

UNIVERSITY OF CALIFORNIA

Los Angeles

**Particle-laden thin film flow:
An alternating direction implicit scheme and
comparison between theory, numerical
simulations, and experiments**

A dissertation submitted in partial satisfaction
of the requirements for the degree
Doctor of Philosophy in Mathematics

by

Matthew Ross Mata

2011

Report Documentation Page		Form Approved OMB No. 0704-0188
Public reporting burden for the collection of information is estimated to average 1 hour per response, including the time for reviewing instructions, searching existing data sources, gathering and maintaining the data needed, and completing and reviewing the collection of information. Send comments regarding this burden estimate or any other aspect of this collection of information, including suggestions for reducing this burden, to Washington Headquarters Services, Directorate for Information Operations and Reports, 1215 Jefferson Davis Highway, Suite 1204, Arlington VA 22202-4302. Respondents should be aware that notwithstanding any other provision of law, no person shall be subject to a penalty for failing to comply with a collection of information if it does not display a currently valid OMB control number.		
1. REPORT DATE JUN 2011	2. REPORT TYPE	3. DATES COVERED 00-00-2011 to 00-00-2011
4. TITLE AND SUBTITLE Particle-laden thin film flow: An alternating direction implicit scheme and comparison between theory, numerical simulations, and experiments		5a. CONTRACT NUMBER
		5b. GRANT NUMBER
		5c. PROGRAM ELEMENT NUMBER
6. AUTHOR(S)	5d. PROJECT NUMBER	
	5e. TASK NUMBER	
	5f. WORK UNIT NUMBER	
7. PERFORMING ORGANIZATION NAME(S) AND ADDRESS(ES) University of California, Los Angeles (UCLA), Department of Mathematics, Los Angeles, CA, 90095		8. PERFORMING ORGANIZATION REPORT NUMBER
9. SPONSORING/MONITORING AGENCY NAME(S) AND ADDRESS(ES)		10. SPONSOR/MONITOR'S ACRONYM(S)
		11. SPONSOR/MONITOR'S REPORT NUMBER(S)
12. DISTRIBUTION/AVAILABILITY STATEMENT Approved for public release; distribution unlimited		
13. SUPPLEMENTARY NOTES		
14. ABSTRACT Gravity-driven thin film flows have been analyzed in terms of fourth-order lubrication models, similarity solutions, traveling wave solutions, numerical simulations and experiments. However, in the case where particle are suspended within the fluid, studies have been largely limited to lubrication models, one-dimensional numerical simulations, and experiments. We present a numerical scheme for a lubrication model derived for particle-laden thin film flow in two dimensions with surface tension. The scheme relies on an alternating direction implicit process to handle the higher-order terms, and an iterative procedure to improve the solution at each timestep. Several aspects of the scheme are examined for a test problem such as the timestep, runtime, and number of iterations. The results from the simulation are compared to experimental data. The simulation shows good qualitative agreement. It also suggests further lines of inquiry for the physical model. For constant-volume particle-laden thin film flow, a lubrication model with precursor and experiments are compared to a power law for the position of the front of the flow with respect to time. This power-law behavior was originally derived for clear fluid flows. In the lubrication model, the precursor has a large effect on the speed of the front, independent of the settling of the particles. Comparison between theory and experiments indicates that this scaling law persists to leading order for particle-laden thin film flows with particle settling. For gravitydriven particle-laden thin film flows on an inclined plane, three distinct regimes can be observed: particles settling to the substrate, a particle-rich ridge forming at the front of the flow, and the particles staying well-mixed. Experiments are conducted for a variety of particle sizes and liquid viscosities. We compare experimental results with equilibrium theory that balances shear-induced migration and hindered settling. We find that the well-mixed regime is transient, with the particle size and liquid viscosity influencing its time scale.		
15. SUBJECT TERMS		

16. SECURITY CLASSIFICATION OF:			17. LIMITATION OF ABSTRACT Same as Report (SAR)	18. NUMBER OF PAGES 120	19a. NAME OF RESPONSIBLE PERSON
a. REPORT unclassified	b. ABSTRACT unclassified	c. THIS PAGE unclassified			

© Copyright by
Matthew Ross Mata
2011

The dissertation of Matthew Ross Mata is approved.

Chris Anderson

Pirouz Kavehpour

Joseph Teran

Andrea Bertozzi, Committee Chair

University of California, Los Angeles

2011

TABLE OF CONTENTS

1	Introduction	1
2	Model	5
3	Numerical Scheme	10
3.1	Time-Discretized Scheme	10
3.2	Adaptive Timestepping	21
3.3	Spatial Discretization	22
3.4	Reference Frame	24
4	Simulations and Comparison to Experiments	32
4.1	Benchmark Simulations	32
4.2	Comparison to Experiments	42
4.3	Summary	48
5	Self-Similarity of Particle-Laden Flow at Constant Volume . .	51
5.1	One-Dimensional Lubrication Model	52
5.2	Well-mixed similarity theory including precursor	56
5.3	Experimental Results	59
5.4	Numerical Simulations	63
5.5	Summary	68
6	Experiments Compared with Equilibrium Theory	70

6.1	Background	70
6.2	Experimental Apparatus and Techniques	74
6.3	Experimental Results	77
6.4	Theoretical Model	84
6.5	Predictions of Theoretical Model vs. Experimental Results	87
6.6	Summary	92
7	Dissertation Summary	95
	References	98

LIST OF FIGURES

2.1	The coordinate system and variables considered in this problem. \mathbf{x} is in the plane, in the direction of the flow; \mathbf{y} is in the plane, perpendicular to \mathbf{x} ; and \mathbf{z} is normal to the plane. h is the film thickness and ϕ is the particle concentration.	6
2.2	The numerical solution of ϕ at time $t = 1000$ without shear-induced diffusion. By this time, an instability has developed near $x = 10$	9
2.3	The numerical solution ϕ at time $t = 1000$ with shear-induced diffusion (2.5). The solution is still stable due to the extra term. .	9
3.1	The intermediate states that develop in the film thickness (left) and particle concentration (right) for the first-order system of equations.	26
3.2	Comparison of theory and simulations at time $t = 100$ for the film thickness, h : theory without higher-order terms (solid line), one-dimensional solution to the full problem (dashed line), perturbed two-dimensional finger (dotted line), and perturbed two-dimensional trough (dot-dashed line). The domain in the y -direction is 15 units long, with the finger slice taken at $y = 7.5$ and the trough slice taken at $y = 1$ (see Figure 3.4).	28
3.3	Comparison of theory and simulations at time $t = 100$ for the particle concentration, ϕ . The labels are the same as in Figure 3.2.	29

3.4	A contour plot of the simulation at times $t = 0$ (left) and $t = 100$ (right) for the film thickness, h , in the perturbed two-dimensional case. The perturbation in two dimensions leads to a fingering instability not seen in the one-dimensional case.	29
3.5	The average front position of the film thickness, h , of the one-dimensional and perturbed two-dimensional case up to time $t = 100$. After an initial transient, the average front positions stay close to each other.	30
3.6	The front position of the film thickness, h , of the perturbed two-dimensional case up to time $t = 100$ along the finger and trough. .	30
3.7	A contour plot of the simulation data at time $t = 100$ for the particle concentration, ϕ , in the perturbed two-dimensional case. The perturbation leads to a particle-rich ridge that outlines and begins to fill in the finger.	31
4.1	The speed-up gained by going from 1 to N processors using OpenMP. The line $y = N$ is shown as a point of reference.	35
4.2	The adaptive timestep up to time $t = 20$. The timestep, Δt , is recorded in intervals of 0.25 for the three cases. <i>Extrapolation and Iterations</i> has a significantly larger timestep than either <i>Time-Lagged and One Iteration</i> or <i>Time-Lagged and Iterations</i>	38
4.3	The number of iterations up to time $t = 100$. The iterations are recorded in intervals of 0.25 for the two cases. Using <i>Extrapolation and Iterations</i> does better than <i>Time-Lagged and Iterations</i> in terms of fewest number of iterations.	39

4.4	The initial film thickness. It is perturbed by a cosine wave along y and smoothed along x by hyperbolic tangent.	40
4.5	Film thickness (left) and particle concentration (right) at time $t = 25$. A small ridge forms in both, with the highest point in the perturbation.	40
4.6	Film thickness (left) and particle concentration (right) at time $t = 50$. A fingering instability and particle-rich ridge form.	41
4.7	Film thickness (left) and particle concentration (right) at time $t = 100$. The fluid finger stretches out ahead of the bulk flow. The particle-rich ridge increases in concentration and has a higher concentration in and around the fingering instability.	41
4.8	The initial condition of the experiment, used for comparing with the simulation. At this point, the front of the flow has begun to develop perturbations, which will lead to fingering instabilities. . .	44
4.9	The initial condition for the film thickness, h , used in the simulation. This is an artificially-created starting condition to be representative of the state shown for the experiment. The height is in mm.	45
4.10	The evolution of the experiment after three minutes. The fingering instability starts to form at the front.	46
4.11	The evolution of the film thickness, h , in the simulation after three minutes. Both the experiment and simulation exhibit a fingering instability, but the instability in the simulation is less pronounced. The height is in mm.	47
4.12	Particle concentration, ϕ , for the film thickness in Figure 4.11. . .	47

5.1	Comparison of front position for different precursor heights, at $L = 2.5$, $\beta = 2$ and $\phi = 0.4$	60
5.2	Time series 45 seconds apart, 35% particle concentration, 45° inclination.	62
5.3	Varying particle concentrations 25, 30, 35, 40, and 45% at two minutes.	62
5.4	Experimental results tracking the average front position and plotting it against the rescaled time $\tau^{1/3}$	63
5.5	Numerical simulations of the particle concentration of solutions of (5.7) and (5.8) with initial concentration $\phi_0 = 0.3$, precursor height 0.01 and for settling function (5.6) with $m = 1$ (left) and $m = 5$ (right) at times $t = 30, 60, 90, 120$. While the plots look qualitatively similar, the more singular solutions for $m = 1$ have larger maxima.	65
5.6	A comparison of scaled solutions. On the left, simulations of (5.7)-(5.8) with precursor but no particle settling. On the right, simulations with precursor and settling with $m = 1$. Both simulations have precursor height 0.05 and initial particle concentration $\phi_0 = 0.4$	65
5.7	Comparison of solutions to the settling model (5.7)-(5.8) with analytical solutions (5.14) of the Riemann problem with precursor height $b = 0.01$ and without precursor for initial particle concentration $\phi_0 = 0.3$, at time $t = 30$	66
5.8	The front position $x_s(\tau)$ plotted versus $\tau^{1/3}$ for different particle concentrations. The data is nearly independent of the choice of settling function. It has precursor height $b = 0.01$	67

5.9	Dependence of the scaling constant C on the particle concentration ϕ . The theoretical scaling constant is computed from (5.11). The numerical and experimental data come from Figures 5.8 and 5.4. .	68
6.1	The experimental apparatus.	74
6.2	The settling regimes: a) settled, b) well-mixed, and c) ridged. The fingering instability typical of clear liquid flows is only observed in the settled and well-mixed regimes.	78
6.3	Phase diagrams for Experiment A. Particle type is fixed (P2), viscosity of the suspending liquid is varied: a) low (L1); and b) high (L2). The symbols denote the regimes observed in experimental runs: circles (\bullet) for settled, triangles (\blacktriangle) for well-mixed, and diamonds (\blacklozenge) for ridged. The solid curve represents the prediction of our theoretical model (see Sections 6.4 and 6.5) for a regime where $\phi' = 0$ (well-mixed).	80
6.4	Phase diagrams for Experiment B. Viscosity of the suspending liquid is fixed (high viscosity, L2), particle size is varied: a) small (P1); b) intermediate (P2); and c) large (P3). The symbols denote the regimes observed in experimental runs: circles (\bullet) for settled, triangles (\blacktriangle) for well-mixed, and diamonds (\blacklozenge) for ridged. The solid curve represents the prediction of our theoretical model (see Sections 6.4 and 6.5) for a regime where $\phi' = 0$ (well-mixed). . . .	81

6.5	Phase diagrams for Experiment C. Viscosity of the suspending liquid is fixed (low viscosity, L1), particle size is varied: a) small (P1) and b) intermediate (P2). The symbols denote the regimes observed in experimental runs: circles (●) for settled, triangles (▲) for well-mixed, and diamonds (◆) for ridged. The solid curve represents the prediction of our theoretical model (see Sections 6.4 and 6.5) for a regime where $\phi' = 0$ (well-mixed).	83
6.6	Numerical solution for $\phi_0 = 0.250$ and $\alpha = 15^\circ$: (a) particle concentration, $\phi(z)$; and (b) velocity, $u(z)$. Note that $\phi_{\max} > \phi(0) > \phi_0$ and $\phi(1) = 0$. This corresponds to the <i>settled</i> regime.	88
6.7	Numerical solution for $\phi_0 = 0.475$ and $\alpha = 45^\circ$: (a) particle concentration, $\phi(z)$; and (b) velocity, $u(z)$. Note that $\phi(0) < \phi_0$ and $\phi(1) = \phi_{\max}$. This corresponds to the <i>ridged</i> regime.	89
6.8	Numerical solution for $\phi_0 = 0.310$ and $\alpha = 45^\circ$: (a) particle concentration, $\phi(z)$; and (b) velocity, $u(z)$. Note that $\phi_{\max} > \phi(0) > \phi_0$ and $\phi(1) = 0$ still apply.	90

LIST OF TABLES

4.1	The intermediate states and shock speed solutions from Equation (3.37) based on the precursor thickness b . As the precursor decreases, both h_i and ϕ_i increase and the shock speeds converge. . .	33
4.2	The two choices to be made when implementing the numerical scheme. One must choose whether to (a) time-lag or extrapolate the approximate terms and (b) whether or not to perform additional iterations past the initial solve.	35
4.3	Results for time $t = 1$ based on various choices for implementation.	36
4.4	Results for time $t = 100$	37
6.1	Physical properties of the liquids and particles used in the experiments.	75
6.2	The different liquid/particle combinations we consider. We study the manner in which the viscosity of the suspending liquid (Experiment A) or particle size (Experiments B and C) affects the settling regime.	76

ACKNOWLEDGMENTS

I would first like to thank my advisor, Andrea Bertozzi, for her help and guidance in my research and academic career. She introduced me to my area of research and opened me up to aspects of it beyond scientific computing. I am grateful to her for the opportunities she has provided me and the encouragement to work hard and put forth my best effort. I am a better mathematician and researcher for serving under her tutelage.

Among the UCLA faculty, I would like to thank Chris Anderson and Joseph Teran. Chris Anderson was my first numerical analysis professor at UCLA and greatly influenced my programming style and appreciation of numerical analysis. He was always willing to answer my questions and give me advice, for which I am grateful. Joseph Teran, through his classes and various discussions, helped me to improve my programming skills and expand my knowledge of scientific computing. I thank Nebojsa Murisic for providing me with good advice regarding the theory and numerics for my research problem. I would also like to thank the various people who helped and influenced me in the early stages of my research: Natalie Grunewald, Rachel Levy, and Thomas Ward. I would finally like to thank my committee members: Chris Anderson, Pirouz Kavehpour, and Joseph Teran.

Chapters 1-4 are from a paper entitled “A numerical scheme for particle-laden thin film flow in two dimensions”, which has been accepted for publication in the *Journal of Computational Physics*. This paper is authored by myself and Andrea Bertozzi. The authors would like to thank Chris Anderson, Nebojsa Murisic, Joseph Teran, and Tom Witelski for their helpful comments and discussions. The images from experiments are courtesy of Joyce Ho, Vincent Hu, Paul Latterman, Trystan Koch, and Kanhui Lin, and were performed during the Research Experience for Undergraduates (REU) program at the University of California, Los

Angeles during the summer of 2009. This research was supported by NSF grants DMS-0601395 and DMS-1048840, and a grant from the UC Lab Fees research fund 09-LR-04-116471-BERA.

Chapter 5 is a version of the paper “Self-similarity in particle-laden flow at constant volume”, which is authored by Natalie Grunewald, Rachel Levy, myself, Thomas Ward, and Andrea Bertozzi. This paper was published in the Journal of Engineering Mathematics in March of 2010. I contributed the experimental part to this paper. The authors thank Ben Cook and A.E. Hosoi for helpful discussions. Natalie Grunewald was supported by the DFG grant GR 3391/1-1. This work was supported by ONR grant N000140610059, and NSF grants ACI-0321917, DMS-0601395, and DMS-0502315, as well as UC Lab Fees research fund 09-LR-04-116741-BERA.

A paper entitled “Particle-laden viscous thin-film flows on an incline: experiments compared with an equilibrium theory” is the basis for Chapter 6. This paper is authored by Nebojsa Murisic, Joyce Ho, Vincent Hu, Paul Latterman, Trystan Koch, Kanhui Lin, myself, and Andrea Bertozzi. This paper has been submitted to Physica D. Most of the work for this paper was done as part of the Research Experience for Undergraduates (REU) program at the University of California, Los Angeles in the summer of 2009, which was overseen by Nebojsa Murisic and myself. The authors would like to gratefully acknowledge the helpful comments of B.P. Cook. This work was supported by NSF grant DMS-0601395 and the UC Lab Fees research fund 09-LR-04-116741-BERA.

VITA

1982	Born, Long Beach, California, USA.
2004	Bachelor of Arts, Applied Mathematics, California State University, Fullerton.
2005–2006	Research Assistant to Mortaza Jamshidian, Mathematics Department, California State University, Fullerton.
2006	Master of Arts, Applied Mathematics, California State University, Fullerton.
2006–2008	Teaching Assistant, Mathematics Department, University of California, Los Angeles.
2008–2009	Research Mentorship Fellowship, Mathematics Department, University of California, Los Angeles.
2008–2011	Research Assistant to Andrea Bertozzi, Mathematics Department, University of California, Los Angeles.

PUBLICATIONS AND PRESENTATIONS

N. Grunewald, R. Levy, M. Mata, T. Ward, and A. Bertozzi (2010). Self-similarity in particle-laden flows at constant volume, *Journal of Engineering Mathematics*, 66:53-63.

M. Jamshidian and M. Mata (2007). Advances in analysis of mean and covariance structures when data are incomplete, Handbook of Latent Variable and Related Models, (S. Y. Lee, Ed.), Chapter 2, 21-44, Elsevier.

M. Jamshidian and M. Mata (2008). Post modeling sensitivity analysis to detect the effect of missing data mechanisms, Multivariate Behavioral Research, 43:432-452.

M. Mata (November, 2009). Self-similarity of particle-laden thin film flows at constant volume. Presented at the Division of Fluid Dynamics 62nd Annual Meeting, Minneapolis, Minnesota.

M. Mata (February, 2010). An numerical scheme for particle-laden thin film flow in 2-D. Presented at the SIAM Conference on Parallel Processing for Scientific Computing, Seattle, Washington.

M. Mata (November, 2010). An ADI scheme for particle-laden thin film flow in 2D. Presented at the Division of Fluid Dynamics 63rd Annual Meeting, Long Beach, California.

M. Mata and A. Bertozzi (2011). A numerical scheme for particle-laden thin film flow in two dimensions, Journal of Computational Physics.

ABSTRACT OF THE DISSERTATION

**Particle-laden thin film flow:
An alternating direction implicit scheme and
comparison between theory, numerical
simulations, and experiments**

by

Matthew Ross Mata

Doctor of Philosophy in Mathematics

University of California, Los Angeles, 2011

Professor Andrea Bertozzi, Chair

Gravity-driven thin film flows have been analyzed in terms of fourth-order lubrication models, similarity solutions, traveling wave solutions, numerical simulations, and experiments. However, in the case where particle are suspended within the fluid, studies have been largely limited to lubrication models, one-dimensional numerical simulations, and experiments. We present a numerical scheme for a lubrication model derived for particle-laden thin film flow in two dimensions with surface tension. The scheme relies on an alternating direction implicit process to handle the higher-order terms, and an iterative procedure to improve the solution at each timestep. Several aspects of the scheme are examined for a test problem, such as the timestep, runtime, and number of iterations. The results from the simulation are compared to experimental data. The simulation shows good qualitative agreement. It also suggests further lines of inquiry for the physical model. For constant-volume particle-laden thin film flow, a lubrication model with precursor and experiments are compared to a power law for the position of the front

of the flow with respect to time. This power-law behavior was originally derived for clear fluid flows. In the lubrication model, the precursor has a large effect on the speed of the front, independent of the settling of the particles. Comparison between theory and experiments indicates that this scaling law persists to leading order for particle-laden thin film flows with particle settling. For gravity-driven particle-laden thin film flows on an inclined plane, three distinct regimes can be observed: particles settling to the substrate, a particle-rich ridge forming at the front of the flow, and the particles staying well-mixed. Experiments are conducted for a variety of particle sizes and liquid viscosities. We compare experimental results with equilibrium theory that balances shear-induced migration and hindered settling. We find that the well-mixed regime is transient, with the particle size and liquid viscosity influencing its time scale.

CHAPTER 1

Introduction

Gravity-driven particle-laden thin film flow occurs in many different contexts, from mudslides to oil spills. A lubrication model has been derived for such flows in two dimensions [CBH08, CAB09]. The model is formulated in terms of the film thickness and particle concentration, with the two dimensions lying in the substrate (see Figure 2.1). It assumes that the particles migrate to the front of the flow, forming a particle-rich ridge. This is one of three possible regimes observed in experiments: particles settling to the substrate, migrating to the front of the flow and forming a particle-rich ridge, or staying well-mixed within the fluid. These regimes are determined by varying the initial particle concentration and inclination angle. Particle-laden thin film flows can be examined using numerical simulations of the model, experiments, and theory existing for similar problems such as clear fluid flows.

In recent years, the problem of numerically solving gravity-driven thin film flow for clear fluids has had ample work done in both one and two dimensions. However, the case when the film contains particles suspended within it has received less attention, especially in two dimensions. The evolution of a clear fluid down an inclined plane is modeled using a single partial differential equation and numerical schemes have been derived using finite differences [DK02, Kon03a] and finite elements [SRX07]. For similar equations, such as spreading thin films, there are methods for finite elements in one dimension [GR00, GR01, ZB00] and for

finite differences in two dimensions [WB03]. The incorporation of particles into such a flow leads to another variable in the model, namely the particle concentration, and an accompanying equation related to the evolution of the particles. The result is a system of equations that requires a different approach from the clear fluid case to formulate a practical numerical scheme, due to the coupling of the equations.

An active area of research in the last decade has been the development of numerical methods for higher-order thin film equations including complex fluids described by systems of equations. Related problems include methods for coupled systems of nonlinear parabolic equations [LCS06, Pao99]. The scheme presented here is, in part, inspired by recent models for surfactants [WCM05] and thin films [WB03]. We choose an Alternating Direction Implicit (ADI) scheme as a tractable method for implicit timesteps, because surface tension introduces a severe restriction on the timestep in the case of explicit schemes. This ADI approach also allows for an implicit scheme while avoiding to have to solve the large sparse linear algebra problems by an iterative method, such as GMRES, that result from linearizing the two-dimensional operators in Newton's method [WB03]. ADI is also amenable to parallelization. While ADI schemes for numerically solving parabolic equations date back to the 1950's [PR55], their use in higher-order problems is rather new, e.g., [WB03], and not all that well-studied. However, the ease of parallelization makes such schemes a viable choice for multiprocessor platforms. Since their inception, ADI schemes have been extended to handle parabolic problems with mixed derivative terms [BW80, CS88, McK71, SIJ76], variable coefficients [Kar09, WB03], and high-order terms [WB03].

The ideas present in these schemes can be combined to create an efficient way to numerically solve the particle-laden thin film flow equations. The nonlin-

earity and higher-order terms are handled in a similar manner to Witelski and Bowen [WB03], which dealt with thin film equations, and the remaining terms are treated as in Warner et al. [WCM05], which devised a semi-implicit scheme for surfactants. This combined approach is fine-tuned to draw out better efficiency, via adaptive timestepping and an iterative procedure within each timestep. At the cost of the extra calculations due to the iterative nature of the scheme, the timestep needed for stability can be improved over recent methods. The result is an efficient method to simulate the continuum model in two dimensions.

The full physics of particle-laden thin film flow is not well understood. Recent experiments, and their comparison to the model, have raised questions. We present such a comparison in this paper, where the results show qualitative agreement. In particular, by performing two-dimensional simulations, we are able to observe finger formation and compare directly with experiments. The development of quantitatively correct models for these systems is an ongoing active area of research. Thus, there is a need for accurate, fully two-dimensional simulations of the model.

Particle-laden thin film flow, as treated in two-dimensional simulations, is most practical as a constant-flux problem. However, experiments are done for the constant-volume problem. A scaling law for the front of the flow, $x(t) \sim Ct^{1/3}$ [Hup82] exists in the constant-volume case for clear fluids and our results indicate that this is still valid for the particle-laden case, to leading order. We also test the impact of choosing different hindered settling functions, which model the effects of particles settling amongst other particles. For particle-laden flows, we compare the results for theory, numerical simulations, and experiments. This comparison is performed using the scaling constants C for each to see how well the three cases agree.

For the particle-laden thin film flow lubrication model, we assume that we are in the regime where a particle-rich ridge forms at the front of the flow. However, depending on the initial particle concentration and inclination angle, different behaviors can be observed. We carry out a systematic study of the regimes for various particle sizes and liquid viscosities. We compare experiments with equilibrium theory to reveal the transient nature of the well-mixed regime, where the particles neither appear to settle to the substrate nor form a particle-rich ridge. The experiments also reveal how the particle size and liquid viscosity affect the time scale of this transient regime.

This dissertation is organized as follows: Chapter 2 discusses the model for particle-laden thin film flow in two dimensions. In Chapter 3, we present a full derivation of the numerical scheme for this problem, with both temporal and spatial discretizations as well as a discussion of a moving reference frame. Simulations and choices for implementing the numerical scheme are given in Chapter 4. The constant-volume problem and comparison between theory, numerical simulations, and experiments are presented in Chapter 5. A comparison of experiments to equilibrium theory is given in Chapter 6. A summary of the previous chapters and results is presented in Chapter 7.

CHAPTER 2

Model

The results from experiments indicate that particle-laden thin film flows exhibit three distinct regimes, based on the initial particle concentration and angle of inclination [ZDB05]. For low concentrations and angles, the particles settle to the substrate with clear fluid flowing over the top. The behavior after sedimentation is similar to clear fluid experiments, such as those performed by Huppert [Hup82]. High concentrations and angles cause a particle-rich ridge to emerge at the front of the flow. Medium concentrations and angles lead to a particle concentration which appears to stay well-mixed throughout the duration of the experiment. Based on Cook [Coo08], this behavior likely belongs to one of the two previously mentioned regimes, but may not have evolved to the point where this distinction can be made.

The evolution equations for the flow are based on the regime where the inclination angle and particle concentration are both high enough to induce the formation of a particle-rich ridge. The equations are formulated in terms of the thickness of the film, h , and the particle concentration by volume, ϕ (see Figure 2.1). The equations for modeling this regime were first derived in Zhou et al. [ZDB05]; re-derived in Cook et al. [CBH08], using conservation of volume rather than mass; and modified in Cook et al. [CAB09], adding in a shear-induced diffusion term to correct for an instability affecting ϕ . The dimensionless system [CAB09] is

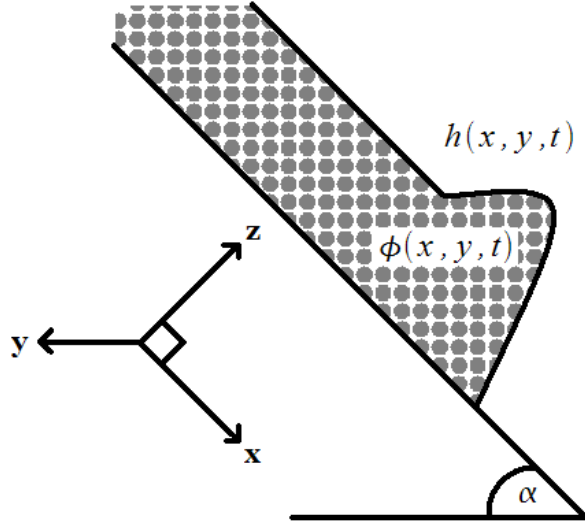


Figure 2.1: The coordinate system and variables considered in this problem. \mathbf{x} is in the plane, in the direction of the flow; \mathbf{y} is in the plane, perpendicular to \mathbf{x} ; and \mathbf{z} is normal to the plane. h is the film thickness and ϕ is the particle concentration.

$$h_t + \nabla \cdot (h \mathbf{v}_{\text{av}}) = 0, \quad (2.1)$$

$$(\phi h)_t + \nabla \cdot [\phi h (\mathbf{v}_{\text{av}} + (1 - \phi) \mathbf{v}_{\text{rel}}) - \mathbf{F}_{\text{diff}}] = 0. \quad (2.2)$$

The orientation for (2.1)-(2.2) is such that \mathbf{x} lies in the plane and is parallel to the direction of the flow, \mathbf{y} is across the plane and perpendicular to \mathbf{x} , and \mathbf{z} is normal to the plane. A one-dimensional form of the problem considers only the x -direction, while two dimensions includes both x and y . The two velocity terms, \mathbf{v}_{av} and \mathbf{v}_{rel} , are the volume-averaged velocity of the fluid and the velocity of the particles relative to the liquid, respectively. We use the term liquid to refer to the substance that the particles are suspended in and fluid to refer to the mixture

as a whole. In Equation (2.2), $\mathbf{v}_{\text{av}} + (1 - \phi)\mathbf{v}_{\text{rel}}$ is the individual velocity of the particles [CBH08] and \mathbf{F}_{diff} is shear-induced diffusion of the particles.

The volume-averaged velocity of the liquid and the particles together is

$$\mathbf{v}_{\text{av}} = \frac{h^2}{\mu(\phi)} \nabla \nabla^2 h - D(\alpha) \left[\frac{h^2}{\mu(\phi)} \nabla (\rho(\phi)h) - \frac{5}{8} \frac{h^3}{\mu(\phi)} \nabla (\rho(\phi)) \right] + \frac{\rho(\phi)}{\mu(\phi)} h^2 \hat{\mathbf{x}}, \quad (2.3)$$

where the terms in (2.3) come from surface tension, the effects of gravity normal to the inclined plane, and the effects of gravity parallel to the inclined plane.

The density of the fluid as a whole is $\rho(\phi) = 1 + \rho_f \phi$; $\rho_f = \frac{\rho_p - \rho_l}{\rho_l}$ is the difference in the densities between the particles and the liquid. The function $\mu(\phi) = (1 - \phi/\phi_{\text{max}})^{-2}$ [Kri72, SP05] is the effective fluid viscosity, where ϕ_{max} is the maximum packing fraction of particles, assuming the particles are spheres. For this problem, the maximum packing fraction has been empirically determined to be 0.58, while the theoretical value is 0.64 [WWG09]. $D(\alpha) = (3Ca)^{1/3} \cot \alpha$ [BB97] is a modified capillary number, where Ca is the capillary number of the liquid and α is the angle of inclination of the plane on which the fluid is flowing ($\alpha = 0$ corresponds to the plane being horizontal while $\alpha = \pi/2$ to vertical).

The settling velocity of the particles, relative to the velocity of the liquid, is a combination of three factors, assumed to be multiplicative,

$$\mathbf{v}_{\text{rel}} = V_s f(\phi) w(h) \hat{\mathbf{x}}. \quad (2.4)$$

The coefficient $V_s = \frac{2}{3} a^2 \rho_f$ in (2.4) is the Stokes settling velocity of a single sphere settling in a viscous liquid, where a is the dimensionless particle radius. A hindered settling function, in this case the Richardson-Zaki function $f(\phi) = (1 - \phi)^5$ [RZ54a], accounts for the effect of sedimentation. The particles settling parallel to the substrate is modeled using a wall effects function,

$w(h) = A(h/a)^2 / \sqrt{1 + (A(h/a)^2)^2}$ with $A = 1/18$. This function is an approximation to a method of images solution to a single sphere falling parallel to a vertical wall [HB65]. This has the property that it is near 0 for h small and near 1 for h large.

Since the system (2.1)-(2.2) is fourth-order and (2.3) contains higher-order terms but (2.4) does not, \mathbf{v}_{rel} is not regularized. This leads to an instability affecting the particle concentration in numerical simulations [CAB09]. To correct for this, a shear-induced diffusion term (2.5) was added in,

$$\mathbf{F}_{\text{diff}} = \frac{3}{2}a^2(3Ca)^{1/3}\hat{D}(\phi)\frac{h^2\rho(\phi)}{\mu(\phi)}\nabla\phi. \quad (2.5)$$

This behavior can be seen in a one-dimensional example on the domain $x : 0 - 50$ with $\Delta x = 0.05$. The initial film thickness is a jump, from 1 to 0.05 at $x = 25$, smoothed by hyperbolic tangent. The initial particle concentration is taken to be $\phi = 0.3$. This simulation is similar to those described in Chapter 4, and a moving reference frame is used, as discussed in Section 3.4. By time $t = 1000$, the solution without the extra diffusion term has developed an instability near $x = 10$ (Figure 2.2) while the one with it is still stable (Figure 2.3). Note that the oscillations trailing the particle-rich ridge, between $x = 0$ and $x = 10$, are a result of the discretization of the moving reference frame and are discussed in Section 3.4. Equation (2.5) accounts for horizontal diffusion of particles in the fluid caused by horizontal gradients of ϕ and was derived based on results from Leighton [Lei85] and Leighton and Acrivos [LA87b]. The term $\hat{D}(\phi) = (1/3)\phi^2 (1 + (1/2)e^{8.8\phi})$ is a dimensionless diffusion coefficient.

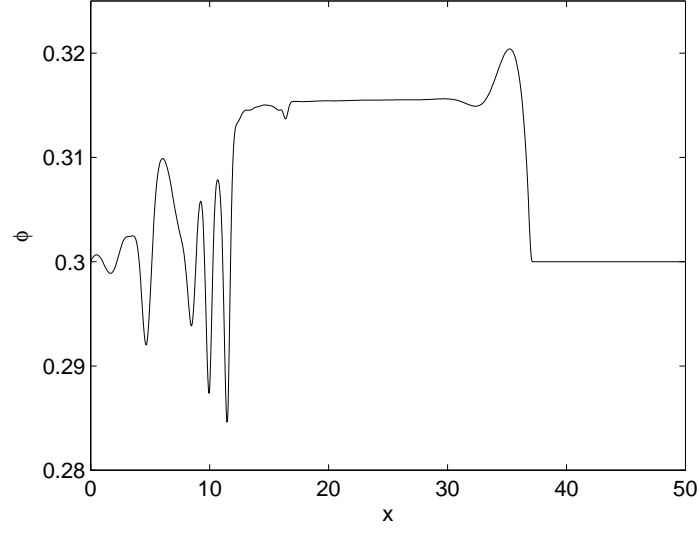


Figure 2.2: The numerical solution of ϕ at time $t = 1000$ without shear-induced diffusion. By this time, an instability has developed near $x = 10$.

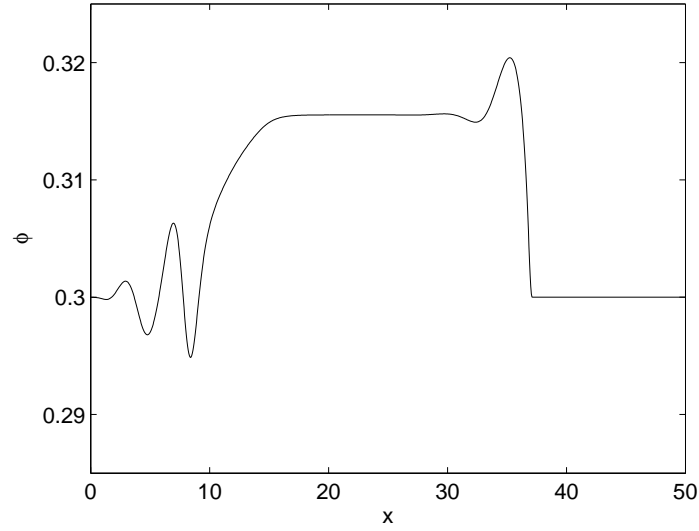


Figure 2.3: The numerical solution ϕ at time $t = 1000$ with shear-induced diffusion (2.5). The solution is still stable due to the extra term.

CHAPTER 3

Numerical Scheme

3.1 Time-Discretized Scheme

In the case of a gravity-driven clear fluid flow, the model reduces to a single equation [BB97] for the film thickness, h ,

$$h_t + (h^3)_x + \nabla \cdot (h^3 \nabla \nabla^2 h - D(\alpha) h^3 \nabla h) = 0. \quad (3.1)$$

Solving (3.1), and similar problems, numerically in one and two dimensions has been performed using several different methods [BBG98, DK02, Kon03a, LGP02, SRX07, WB03]. Including particles in the physics not only adds a second equation, but couples it to the equation for the film thickness. The particle-laden case has been solved numerically in one dimension with methods such as forward Euler with upwind differencing [ZDB05] and the Lax-Friedrichs method [CBH08] when the high-order terms are omitted, and backward Euler with centered differencing [ZDB05] when the terms are included.

This system of PDEs in two dimensions poses numerical difficulties beyond those present in the clear fluid problem. For both the clear and particle-laden cases, fully explicit schemes typically have the problem that an $O(\Delta x^4)$ timestep, assuming $\Delta x = \Delta y$, is needed for stability. One solution is to use an implicit scheme. For the clear fluid and similar problems, the nonlinearity combined with

an implicit scheme amounts to solving the problem at each timestep using an iterative process, such as Newton’s method, to converge to the solution [WB03]. For the particle-laden case, using an implicit scheme typically requires that both equations be solved simultaneously, using an iterative process to account for the nonlinearity. This results in a linear algebra problem with twice the number of unknowns and a matrix that is twice as large in each dimension, compared to the clear fluid problem. Therefore, solving the particle-laden case leads to larger linear algebra problems to solve at each timestep and the matrix from Newton’s method will have a more complex structure than for clear fluids.

The goal of the scheme presented here is to circumvent some of the aforementioned difficulties. The advantages of this approach, over a purely explicit scheme or implicit with Newton’s method, are that the timestep is more lenient than for a fully explicit scheme and the linear algebra problem that results from the implicit part of the scheme is reduced to a series of smaller banded matrix solves, which can be done efficiently and independently for each equation.

The numerical scheme that we employ for the particle-laden thin film flow problem is inspired by the schemes presented in Witelski and Bowen [WB03] for higher-order parabolic PDEs and Warner et al. [WCM05] for surfactants. In Witelski and Bowen, several ADI schemes, based on backward Euler, second-order backward difference formulas, as well as Newton-like schemes, are derived for solving the nonlinear PDE known as the thin film equation,

$$h_t + \nabla \cdot (f(h) \nabla \nabla^2 h) = 0. \quad (3.2)$$

The backward Euler-based ADI scheme for (3.2) uses approximate values of h in the nonlinear and mixed-derivative implicit terms. It is suggested to start with approximations, such as time-lagged values, for evaluating these terms and calcu-

lating the numerical solution at the timestep. Then use this solution for the new approximate values within the same timestep and recalculate. This results in an iterative scheme at each timestep. However, for solving the thin film equation, it was noted that the iterations did not provide a noticeable improvement. Warner et al. use this method for a coupled system of nonlinear PDEs relating to surfactants. They handle the higher-order terms implicitly using Crank-Nicolson, and apply ADI to this. The remaining terms, which are at least second-order in space, are treated explicitly. For the nonlinearity and mixed-derivative terms, the values are time-lagged and the problem is solved only once per timestep. In the simulations, $\Delta x = \Delta y = \pi/100 \approx 0.0314$ required a timestep of $O(10^{-5})$.

Our approach is to handle applicable terms implicitly, using ADI, and treat the remaining terms explicitly, as we show below. The terms handled implicitly are those with spatial derivatives on the same variable as the time derivative. For example, Equation (2.1) has the time derivative on h , so the terms treated implicitly should have spatial derivatives on h . Making this choice allows for the splitting of the two-dimensional operators into the product of two one-dimensional operators in the derivation of the ADI scheme. Iterations within each timestep allow for a larger Δt to be taken at the cost of some extra calculations. In general, the increase in the size of the timestep outweighs the extra computational work, as shown in Chapter 4.

For Equation (2.1), the terms

$$\nabla \cdot \left(\frac{h^3}{\mu(\phi)} \nabla \nabla^2 h + \frac{\rho(\phi)}{\mu(\phi)} h^3 \hat{\mathbf{x}} \right) \quad (3.3)$$

can be handled implicitly. This is because the spatial derivatives on these terms are applied to h . Of these terms, some parts of them will be handled by approximation, as in Witelski and Bowen [WB03]. Including the first-order terms

in the implicit treatment allows them to be discretized spatially using centered differencing to maintain stability. Solving this equation numerically assumes that ϕ is known, or can be approximated, and we are solving for h . First discretize the terms in (3.3) in time with backward Euler, including the time derivative,

$$h^{n+1} + \Delta t \nabla \cdot \left(\frac{h^3}{\mu(\phi)} \nabla \nabla^2 h + \frac{\rho(\phi)}{\mu(\phi)} h^3 \hat{\mathbf{x}} \right)^{n+1} = h^n. \quad (3.4)$$

Write out the operators in (3.4) fully,

$$\begin{aligned} & h^{n+1} + \Delta t \left[\partial_x \left(\frac{h^3}{\mu(\phi)} h_{xxx} \right) + \partial_y \left(\frac{h^3}{\mu(\phi)} h_{yyy} \right) \right. \\ & \left. + \partial_x \left(\frac{\rho(\phi)}{\mu(\phi)} h^3 \right) \right]^{n+1} + \Delta t \left[\partial_x \left(\frac{h^3}{\mu(\phi)} h_{yyx} \right) + \partial_y \left(\frac{h^3}{\mu(\phi)} h_{xxy} \right) \right]^{n+1} = h^n. \end{aligned} \quad (3.5)$$

The idea behind the ADI approach is to reduce the implicit part of (3.5), with derivatives in both x and y , to a product of two operators, each with only derivatives in either x or y . To achieve this, the terms involving only x -derivatives and only y -derivatives are grouped together. Define the operators

$$D_x = \partial_x \left(\frac{h^3}{\mu(\phi)} \partial_{xxx} + \frac{\rho(\phi)}{\mu(\phi)} h^2 I \right)^{n+1}, \quad D_y = \partial_y \left(\frac{h^3}{\mu(\phi)} \partial_{yyy} \right)^{n+1}. \quad (3.6)$$

Then replacing the terms in (3.5) with the definitions in (3.6), we have

$$\begin{aligned} & h^{n+1} + \Delta t (D_x + D_y) h^{n+1} \\ & + \Delta t \left[\partial_x \left(\frac{h^3}{\mu(\phi)} h_{yyx} \right) + \partial_y \left(\frac{h^3}{\mu(\phi)} h_{xxy} \right) \right]^{n+1} = h^n. \end{aligned} \quad (3.7)$$

In order to obtain an ADI scheme from (3.7), note that $I + \Delta t D_x + \Delta t D_y = (I + \Delta t D_x)(I + \Delta t D_y) - (\Delta t)^2 D_x D_y$ and so the left-hand side, with the addition of an $O(\Delta t^2)$ term, can be written as a product of two one-dimensional operators.

$$(I + \Delta t D_x)(I + \Delta t D_y)h^{n+1} - (\Delta t)^2 D_x D_y h^{n+1} + \Delta t \left[\partial_x \left(\frac{h^3}{\mu(\phi)} h_{yyx} \right) + \partial_y \left(\frac{h^3}{\mu(\phi)} h_{xxy} \right) \right]^{n+1} = h^n. \quad (3.8)$$

To handle the nonlinear terms, which occur in front of derivatives, and mixed-derivative terms in (3.8), define them as approximate, denoted by a tilde (e.g., \tilde{h}^{n+1}). The approximate terms can be chosen in some reasonable manner, such as time-lagged or extrapolated. This will be discussed in more detail later. Subtract the mixed-derivative terms from and add the $O(\Delta t^2)$ term to both sides. This leaves a scheme in which all the terms operating on h^{n+1} are known, as is the entire right-hand side.

$$(I + \Delta t \tilde{D}_x)(I + \Delta t \tilde{D}_y)h^{n+1} = h^n + \left\{ (\Delta t)^2 \tilde{D}_x \tilde{D}_y - \Delta t \left[\partial_x \left(\frac{\tilde{h}^3}{\mu(\tilde{\phi})} \partial_{yyx} \right) + \partial_y \left(\frac{\tilde{h}^3}{\mu(\tilde{\phi})} \partial_{xxy} \right) \right] \right\}^{n+1} \tilde{h}^{n+1}. \quad (3.9)$$

For simplicity, define the operators in (3.9) as

$$\tilde{L}_x = I + \Delta t \tilde{D}_x, \quad \tilde{L}_y = I + \Delta t \tilde{D}_y.$$

Subtracting $\tilde{L}_x \tilde{L}_y \tilde{h}^{n+1}$ from both sides of (3.9), which cancels the $O(\Delta t^2)$ term, yields

$$\tilde{L}_x \tilde{L}_y \left(h^{n+1} - \tilde{h}^{n+1} \right) = - \left(\tilde{h}^{n+1} - h^n \right) - \Delta t \nabla \cdot \left(\frac{\tilde{h}^3}{\mu(\tilde{\phi})} \nabla \nabla^2 \tilde{h} + \frac{\rho(\tilde{\phi})}{\mu(\tilde{\phi})} \tilde{h}^3 \hat{\mathbf{x}} \right)^{n+1}. \quad (3.10)$$

At this point, the implicit part of the scheme is complete and the explicit terms can be added back into (3.10) using forward Euler.

$$\begin{aligned}
& \tilde{L}_x \tilde{L}_y \left(h^{n+1} - \tilde{h}^{n+1} \right) = - \left(\tilde{h}^{n+1} - h^n \right) \\
& - \Delta t \nabla \cdot \left(\frac{\tilde{h}^3}{\mu(\tilde{\phi})} \nabla \nabla^2 \tilde{h} + \frac{\rho(\tilde{\phi})}{\mu(\tilde{\phi})} \tilde{h}^3 \hat{\mathbf{x}} \right)^{n+1} \\
& + \Delta t \nabla \cdot \left\{ D(\alpha) \left[\frac{h^3}{\mu(\phi)} \nabla (\rho(\phi) h) - \frac{5}{8} \frac{h^4}{\mu(\phi)} \nabla (\rho(\phi)) \right] \right\}^n. \tag{3.11}
\end{aligned}$$

Define

$$u = h^{n+1} - \tilde{h}^{n+1},$$

which can be thought of as a correction term to the approximation of h^{n+1} , and (3.11) can be written as a three-step process: two one-directional solves (3.12)-(3.13) and an update step (3.14).

$$\begin{aligned}
\tilde{L}_x v = & - \left(\tilde{h}^{n+1} - h^n \right) - \Delta t \nabla \cdot \left(\frac{\tilde{h}^3}{\mu(\tilde{\phi})} \nabla \nabla^2 \tilde{h} + \frac{\rho(\tilde{\phi})}{\mu(\tilde{\phi})} \tilde{h}^3 \hat{\mathbf{x}} \right)^{n+1} \\
& + \Delta t \nabla \cdot \left\{ D(\alpha) \left[\frac{h^3}{\mu(\phi)} \nabla (\rho(\phi) h) - \frac{5}{8} \frac{h^4}{\mu(\phi)} \nabla (\rho(\phi)) \right] \right\}^n, \tag{3.12}
\end{aligned}$$

$$\tilde{L}_y u = v, \tag{3.13}$$

$$h^{n+1} \approx \tilde{h}^{n+1} + u. \tag{3.14}$$

Since the operators \tilde{L}_x and \tilde{L}_y involve at most fourth-order terms, the spatial discretization of them will lead to a five-point stencil in the x - and y -direction,

respectively. This discretization is discussed fully in Section 3.3. Along each row/column of the discretized domain, this results in a pentadiagonal linear algebra problem. This can be solved using a pentadiagonal solver, or a more generic banded matrix solver.

To help with the inaccuracy in the nonlinear and mixed-derivative terms resulting from approximation, an iterative procedure can be used at each timestep to improve the solution and size of the timestep. This was first suggested for the ADI scheme in the context of thin film equations [WB03]. This procedure amounts to repeating the three-step process associated with solving each equation at each timestep and updating the approximate solution with the most recent solution, until the new and approximate solutions sufficiently converge. For example, one would solve (3.12)-(3.14), solve (3.24)-(3.26), and examine how much the approximate solution differs from this computed solution. If this difference is significant, one can replace the old approximate terms with the computed solution and solve the same timestep again. This process can be continued until the approximate and computed solutions are close. This is similar to fixed-point iteration.

For Equation (2.1), when entering the timestep, a choice must be made as to the value of \tilde{h}^{n+1} and $(\tilde{\phi}\tilde{h})^{n+1}$. Using h as an example, two reasonable choices would be a time-lagged approximation, h^n , which is a first-order accurate approximation in time, or an extrapolated approximation, $2h^n - h^{n-1}$, which is second-order in time. For adaptive timestepping, this extrapolation is given by $h^n + (\Delta t / \Delta t_{\text{old}})(h^n - h^{n-1})$, where Δt is the prospective timestep between t^n and t^{n+1} and Δt_{old} is the timestep between t^{n-1} and t^n . While the second choice of an approximation is second-order, it also requires storing an extra set of data, namely h^{n-1} . Other choices for estimating h^{n+1} and $(\phi h)^{n+1}$ based on previous

data could be used as well. With this choice made, the three-step process for each equation can be implemented, obtaining a solution for h^{n+1} and $(\phi h)^{n+1}$. We refer to the case when the solution obtained here is accepted as performing *One Iteration*. However, at this point, the approximation can be redefined, $\tilde{h}^{n+1} = h^{n+1}$, and the process repeated. This can be continued until convergence between the approximate and new solution, or equivalently when the correction term u is small in a chosen norm. We refer to this case as *Iterations* since the problem is solved iteratively for each timestep.

For (2.2), the ADI method is applied to ϕh as a whole, since the time derivative is on this term. The applicable terms in the equation are

$$\begin{aligned} & \nabla \cdot \left[-D(\alpha) \left(\rho_f \frac{(\phi h)h^2}{\mu(\phi)} \nabla(\phi h) \right) \right. \\ & \left. + \phi h \left(\frac{\rho(\phi)}{\mu(\phi)} h^2 + (1 - \phi) V_s f(\phi) w(h) \right) \hat{\mathbf{x}} \right]. \end{aligned} \quad (3.15)$$

As with (2.1), the time discretization of (3.15) is based on a backward Euler method

$$\begin{aligned} & (\phi h)^{n+1} + \Delta t \nabla \cdot \left[-D(\alpha) \left(\rho_f \frac{(\phi h)h^2}{\mu(\phi)} \nabla(\phi h) \right) \right. \\ & \left. + \phi h \left(\frac{\rho(\phi)}{\mu(\phi)} h^2 + (1 - \phi) V_s f(\phi) w(h) \right) \hat{\mathbf{x}} \right]^{n+1} = (\phi h)^n. \end{aligned} \quad (3.16)$$

Writing out the operators in (3.16) explicitly,

$$\begin{aligned} & (\phi h)^{n+1} - \Delta t D(\alpha) \rho_f \left[\partial_x \left(\frac{(\phi h)h^2}{\mu(\phi)} \partial_x(\phi h) \right) + \partial_y \left(\frac{(\phi h)h^2}{\mu(\phi)} \partial_y(\phi h) \right) \right]^{n+1} \\ & + \Delta t \partial_x \left[\phi h \left(\frac{\rho(\phi)}{\mu(\phi)} h^2 + (1 - \phi) V_s f(\phi) w(h) \right) \right]^{n+1} = (\phi h)^n. \end{aligned} \quad (3.17)$$

Define the operators in (3.17) involving only x -derivatives and only y -derivatives as \mathcal{D}_x and \mathcal{D}_y , respectively.

$$\begin{aligned}\mathcal{D}_x &= -D(\alpha)\rho_f\partial_x\left(\frac{(\phi h)h^2}{\mu(\phi)}\partial_x\right)^{n+1} \\ &+ \partial_x\left(\left[\frac{\rho(\phi)}{\mu(\phi)}h^2(1-\phi)V_sf(\phi)w(h)\right]I\right)^{n+1}, \\ \mathcal{D}_y &= -D(\alpha)\rho_f\partial_y\left(\frac{(\phi h)h^2}{\mu(\phi)}\partial_y\right)^{n+1}.\end{aligned}\tag{3.18}$$

Using (3.18), the equation can be compactly written as

$$(\phi h)^{n+1} + \Delta t (\mathcal{D}_x + \mathcal{D}_y) (\phi h)^{n+1} = (\phi h)^n.\tag{3.19}$$

Note that there are no mixed-derivative terms to handle in (3.19). The left-hand side can be written as the product of two one-dimensional operators, incurring an $O(\Delta t^2)$ term in the process.

$$(I + \Delta t \mathcal{D}_x)(I + \Delta t \mathcal{D}_y)(\phi h)^{n+1} - (\Delta t)^2 \mathcal{D}_x \mathcal{D}_y (\phi h)^{n+1} = (\phi h)^n.\tag{3.20}$$

Add the $O(\Delta t^2)$ term to both sides of (3.20), and make all terms that occur nonlinearly at time t^{n+1} approximate, as before.

$$(I + \Delta t \tilde{\mathcal{D}}_x)(I + \Delta t \tilde{\mathcal{D}}_y)(\phi h)^{n+1} = (\phi h)^n + (\Delta t)^2 \tilde{\mathcal{D}}_x \tilde{\mathcal{D}}_y (\tilde{\phi} \tilde{h})^{n+1}.\tag{3.21}$$

Define

$$\tilde{\mathcal{L}}_x = I + \Delta t \tilde{\mathcal{D}}_x, \quad \tilde{\mathcal{L}}_y = I + \Delta t \tilde{\mathcal{D}}_y$$

and subtract $\tilde{\mathcal{L}}_x \tilde{\mathcal{L}}_y (\tilde{\phi} \tilde{h})^{n+1}$ from both sides of (3.21) to obtain

$$\begin{aligned} \tilde{\mathcal{L}}_x \tilde{\mathcal{L}}_y \left((\phi h)^{n+1} - (\tilde{\phi} \tilde{h})^{n+1} \right) &= - \left((\tilde{\phi} \tilde{h})^{n+1} - (\phi h)^n \right) \\ &\quad - \Delta t \nabla \cdot \left[-D(\alpha) \left(\rho_f \frac{(\tilde{\phi} \tilde{h}) \tilde{h}^2}{\mu(\tilde{\phi})} \nabla(\tilde{\phi} \tilde{h}) \right) \right. \\ &\quad \left. + \tilde{\phi} \tilde{h} \left(\frac{\rho(\tilde{\phi})}{\mu(\tilde{\phi})} \tilde{h}^2 + (1 - \tilde{\phi}) V_s f(\tilde{\phi}) w(\tilde{h}) \right) \hat{\mathbf{x}} \right]^{n+1}. \end{aligned} \quad (3.22)$$

The remaining terms can be incorporated into (3.22) via forward Euler.

$$\begin{aligned} \tilde{\mathcal{L}}_x \tilde{\mathcal{L}}_y \left((\phi h)^{n+1} - (\tilde{\phi} \tilde{h})^{n+1} \right) &= - \left((\tilde{\phi} \tilde{h})^{n+1} - (\phi h)^n \right) \\ &\quad - \Delta t \nabla \cdot \left[-D(\alpha) \left(\rho_f \frac{(\tilde{\phi} \tilde{h}) \tilde{h}^2}{\mu(\tilde{\phi})} \nabla(\tilde{\phi} \tilde{h}) \right) \right. \\ &\quad \left. + \tilde{\phi} \tilde{h} \left(\frac{\rho(\tilde{\phi})}{\mu(\tilde{\phi})} \tilde{h}^2 + (1 - \tilde{\phi}) V_s f(\tilde{\phi}) w(\tilde{h}) \right) \hat{\mathbf{x}} \right]^{n+1} \\ &\quad - \Delta t \nabla \cdot \left[\phi h \left(\frac{h^2}{\mu(\phi)} \nabla \nabla^2 h - D(\alpha) \left(\frac{h^2}{\mu(\phi)} \nabla h - \frac{5}{8} \frac{h^3}{\mu(\phi)} \nabla(\rho(\phi)) \right) \right) \right. \\ &\quad \left. - \mathbf{F}_{\text{diff}} \right]^n. \end{aligned} \quad (3.23)$$

Define

$$w = (\phi h)^{n+1} - (\tilde{\phi} \tilde{h})^{n+1}.$$

Then (3.23) can be written out as the three-step process (3.24)-(3.26):

$$\begin{aligned}
\tilde{\mathcal{L}}_x v = & - \left((\tilde{\phi}\tilde{h})^{n+1} - (\phi h)^n \right) \\
& - \Delta t \nabla \cdot \left[-D(\alpha) \left(\rho_f \frac{(\tilde{\phi}\tilde{h})\tilde{h}^2}{\mu(\tilde{\phi})} \nabla(\tilde{\phi}\tilde{h}) \right) \right. \\
& \left. + \tilde{\phi}\tilde{h} \left(\frac{\rho(\tilde{\phi})}{\mu(\tilde{\phi})} \tilde{h}^2 + (1 - \tilde{\phi}) V_s f(\tilde{\phi}) w(\tilde{h}) \right) \hat{\mathbf{x}} \right]^{n+1} \\
& - \Delta t \nabla \cdot \left[\phi h \left(\frac{h^2}{\mu(\phi)} \nabla \nabla^2 h - D(\alpha) \left(\frac{h^2}{\mu(\phi)} \nabla h - \frac{5}{8} \frac{h^3}{\mu(\phi)} \nabla(\rho(\phi)) \right) \right) \right. \\
& \left. - \mathbf{F}_{\text{diff}} \right]^n, \tag{3.24}
\end{aligned}$$

$$\tilde{\mathcal{L}}_y w = v, \tag{3.25}$$

$$(\phi h)^{n+1} \approx (\tilde{\phi}\tilde{h})^{n+1} + w. \tag{3.26}$$

The spatial operators in the $\tilde{\mathcal{L}}_x$ and $\tilde{\mathcal{L}}_y$ terms are at most second-order, and spatial discretization leads to a three-point stencil in each direction. Similar to (3.12) and (3.13), a tridiagonal solver or banded matrix solver can be used to solve along each row/column.

Solving the system, as a whole, at each timestep can be then achieved by solving (2.1) using (3.12)-(3.14) for h^{n+1} , solving (2.2) using (3.24)-(3.26) for $(\phi h)^{n+1}$, then recovering the particle concentration as $\phi^{n+1} = (\phi h)^{n+1}/h^{n+1}$. Note that each solve only uses values $h^n, \tilde{h}^{n+1}, \phi^n$, and $\tilde{\phi}^{n+1}$, all of which are known. This scheme can be solved in other possible ways. One might choose to use, after solving (2.1), h^{n+1} in lieu of an approximation for \tilde{h}^{n+1} for solving (2.2). Alternatively, the equations could be solved in the opposite order.

3.2 Adaptive Timestepping

We use an adaptive timestepping scheme to advance the solution. The scheme utilizes the solution at consecutive timesteps t^{n-1}, t^n, t^{n+1} . Based on a measure of error, it decides whether or not to accept the new solution, and if it is reasonable to increase the size of the timestep. This is a modification of the scheme used in Bertozzi et al. [BBD94], in which it serves as an estimate of a dimensionless local truncation error in time. Consider the solution of the film thickness, h , at times t^{n-1}, t^n , and t^{n+1} . Calculate $e^{n+1} = (h^{n+1} - h^n)/h^n$ and $e^n = (h^n - h^{n-1})/h^n$. The modification from the original method is to divide by the value h^n at each point rather than $h_{\max}^n = \max_{i,j}\{h_{i,j}^n\}$, since it produces a better-working adaptive scheme for this problem. Denote the timestep going from time t^n to t^{n+1} as Δt and from t^{n-1} to t^n as Δt_{old} . Then define

$$\text{Error} = \left\| e^{n+1} - \frac{\Delta t}{\Delta t_{\text{old}}} e^n \right\|. \quad (3.27)$$

This provides a dimensionless estimate of the local truncation error in time, accumulated over the grid. The solution will be accepted if this error is less than some tolerance, denoted Tol_1 . If the error is less than a smaller tolerance, $\text{Tol}_2 < \text{Tol}_1$, for a fixed number of steps, the timestep is increased by a scale factor. If the error is larger than Tol_1 , the maximum number of iterations within a timestep is surpassed, or the solution becomes negative, the timestep is reduced by a factor of 2. An example for Tol_1 and Tol_2 would be $10^{-7} \times (\text{Area of Domain})$ and $10^{-9} \times (\text{Area of Domain})$ respectively, where the difference in the tolerances is at least an order of magnitude apart to prevent the error from alternating between too large to accept and small enough to increase the timestep. The form of these tolerances were chosen to make it convenient for various size domains

without having to change the tolerances manually for each domain.

Since (3.27) only takes into account one of the two variables, this error can be computed for ϕh , or merely ϕ , as well. These two errors can be combined into an overall measure of the error by taking the maximum of the two, or by some other reasonable combination such as adding the two errors together or choosing a separate set of tolerances for each.

3.3 Spatial Discretization

We use centered finite differences for all spatial discretizations. Using the notation, $h_{i+1/2,j} \approx (h_{i,j} + h_{i+1,j})/2$, the fourth-order term in (2.1) is

$$\begin{aligned}
& \nabla \cdot \left(\frac{h^3}{\mu(\phi)} \nabla \nabla^2 h \right)_{i,j} \\
& \approx \left(\frac{h_{i+1/2,j}^3}{\mu(\phi_{i+1/2,j})} h_{xxx,i+1/2,j} - \frac{h_{i-1/2,j}^3}{\mu(\phi_{i-1/2,j})} h_{xxx,i-1/2,j} \right) / \Delta x \\
& + \left(\frac{h_{i+1/2,j}^3}{\mu(\phi_{i+1/2,j})} h_{yyx,i+1/2,j} - \frac{h_{i-1/2,j}^3}{\mu(\phi_{i-1/2,j})} h_{yyx,i-1/2,j} \right) / \Delta x \\
& + \left(\frac{h_{i,j+1/2}^3}{\mu(\phi_{i,j+1/2})} h_{xxy,i,j+1/2} - \frac{h_{i,j-1/2}^3}{\mu(\phi_{i,j-1/2})} h_{xxy,i,j-1/2} \right) / \Delta y \\
& + \left(\frac{h_{i,j+1/2}^3}{\mu(\phi_{i,j+1/2})} h_{yyy,i,j+1/2} - \frac{h_{i,j-1/2}^3}{\mu(\phi_{i,j-1/2})} h_{yyy,i,j-1/2} \right) / \Delta y. \tag{3.28}
\end{aligned}$$

Here, the third derivatives are calculated at half-grid points by differencing consecutive standard second-order approximations. Two representative examples are

$$\begin{aligned}
h_{xxx,i+1/2,j} &\approx (h_{i+2,j} - 3h_{i+1,j} + 3h_{i,j} - h_{i-1,j}) / \Delta x^3, \\
h_{xxy,i,j+1/2} &\approx ((h_{i+1,j+1} - 2h_{i,j+1} + h_{i-1,j+1}) / \Delta x^2 \\
&\quad - (h_{i+1,j} - 2h_{i,j} + h_{i-1,j}) / \Delta x^2) / \Delta y.
\end{aligned} \tag{3.29}$$

The two second-order terms are discretized as

$$\begin{aligned}
&\nabla \cdot \left(\frac{h^3}{\mu(\phi)} \nabla(\rho(\phi)h) \right)_{i,j} \\
&\approx \left(\frac{h_{i+1/2,j}^3}{\mu(\phi_{i+1/2,j})} (\rho(\phi_{i+1,j})h_{i+1,j} - \rho(\phi_{i,j})h_{i,j}) \right. \\
&\quad \left. - \frac{h_{i-1/2,j}^3}{\mu(\phi_{i-1/2,j})} (\rho(\phi_{i,j})h_{i,j} - \rho(\phi_{i-1,j})h_{i-1,j}) \right) / \Delta x^2 \\
&\quad + \left(\frac{h_{i,j+1/2}^3}{\mu(\phi_{i,j+1/2})} (\rho(\phi_{i,j+1})h_{i,j+1} - \rho(\phi_{i,j})h_{i,j}) \right. \\
&\quad \left. - \frac{h_{i,j-1/2}^3}{\mu(\phi_{i,j-1/2})} (\rho(\phi_{i,j})h_{i,j} - \rho(\phi_{i,j-1})h_{i,j-1}) \right) / \Delta y^2,
\end{aligned} \tag{3.30}$$

$$\begin{aligned}
&\nabla \cdot \left(\frac{h^4}{\mu(\phi)} \nabla(\rho(\phi)) \right)_{i,j} \\
&\approx \left(\frac{h_{i+1/2,j}^4}{\mu(\phi_{i+1/2,j})} (\rho(\phi_{i+1,j}) - \rho(\phi_{i,j})) \right. \\
&\quad \left. - \frac{h_{i-1/2,j}^4}{\mu(\phi_{i-1/2,j})} (\rho(\phi_{i,j}) - \rho(\phi_{i-1,j})) \right) / \Delta x^2 \\
&\quad + \left(\frac{h_{i,j+1/2}^4}{\mu(\phi_{i,j+1/2})} (\rho(\phi_{i,j+1}) - \rho(\phi_{i,j})) \right. \\
&\quad \left. - \frac{h_{i,j-1/2}^4}{\mu(\phi_{i,j-1/2})} (\rho(\phi_{i,j}) - \rho(\phi_{i,j-1})) \right) / \Delta y^2.
\end{aligned} \tag{3.31}$$

The advective term is discretized using a standard centered-differencing scheme.

The terms in (2.2) are discretized in the same manner since many of them are similar to those in (2.1). The fourth- and second-order terms that come from \mathbf{v}_{av} are discretized as in (3.28)-(3.31), with h replaced by ϕh . Both advective terms are discretized via standard centered differencing.

The shear-induced diffusion term is discretized the same way as (3.30)-(3.31).

$$\begin{aligned}
& \nabla \cdot \left(\hat{D}(\phi) \frac{h^2 \rho(\phi)}{\mu(\phi)} \nabla \phi \right)_{i,j} \\
& \approx \left(\hat{D}(\phi_{i+1/2,j}) \frac{h_{i+1/2,j}^2 \rho(\phi_{i+1/2,j})}{\mu(\phi_{i+1/2,j})} (\phi_{i+1,j} - \phi_{i,j}) - \right. \\
& \quad \left. \hat{D}(\phi_{i-1/2,j}) \frac{h_{i-1/2,j}^2 \rho(\phi_{i-1/2,j})}{\mu(\phi_{i-1/2,j})} (\phi_{i,j} - \phi_{i-1,j}) \right) / \Delta x^2 \\
& \quad + \left(\hat{D}(\phi_{i,j+1/2}) \frac{h_{i,j+1/2}^2 \rho(\phi_{i,j+1/2})}{\mu(\phi_{i,j+1/2})} (\phi_{i,j+1} - \phi_{i,j}) \right. \\
& \quad \left. - \hat{D}(\phi_{i,j-1/2}) \frac{h_{i,j-1/2}^2 \rho(\phi_{i,j-1/2})}{\mu(\phi_{i,j-1/2})} (\phi_{i,j} - \phi_{i,j-1}) \right) / \Delta y^2. \tag{3.32}
\end{aligned}$$

Centered differencing is not used for the moving reference frame, if one is employed. Instead, a second-order upwind differencing scheme is used, which will be discussed in the next section.

3.4 Reference Frame

The area of interest in the simulations is near the front of the flow, where effects like the capillary and particle-rich ridges occur. With a fixed reference frame, the spatial domain would need to be taken as the entire area over which the flow would evolve, leading to large portions of the domain where no change is

occurring. This issue can be easily addressed by using a moving reference frame.

To implement a moving reference frame, we add an extra term to each equation, $-sh_x$ on the left-hand side of (2.1) and $-s(\phi h)_x$ on (2.2). Here, $s > 0$ is the speed at which the moving reference frame travels. Zhou et al. [ZDB05] approximate the front speed by removing all terms from the equations which are higher than first order, leaving only the advective terms. They observe that these terms capture the large scale dynamics, including the speed of the shocks, and the ridges that develop in h and ϕ . This leaves a 2×2 system of conservation laws of the form

$$h_t + [F(h, \phi h)]_x = 0, \quad (3.33)$$

$$(\phi h)_t + [G(h, \phi h)]_x = 0, \quad (3.34)$$

where F and G are defined as

$$F(h, \phi h) = \frac{\rho(\phi)}{\mu(\phi)} h^3,$$

$$G(h, \phi h) = \frac{\rho(\phi)}{\mu(\phi)} (\phi h) h^2 + (\phi h)(1 - \phi) V_s f(\phi) w(h).$$

The initial conditions for (3.33)-(3.34) are

$$h(x, 0) = \begin{cases} h_l, & x \leq 0, \\ h_r, & x > 0, \end{cases} \quad (3.35)$$

$$(\phi h)(x, 0) = \begin{cases} \phi_0 h_l, & x \leq 0, \\ \phi_0 h_r, & x > 0. \end{cases} \quad (3.36)$$

where h_l and h_r in (3.35) and (3.36) are the initial film thickness and the height of the precursor b , respectively, and ϕ_0 in (3.36) is the initial particle concentration of the fluid. These initial conditions specify a Riemann problem [Lax73]. From the initial shock in both equations, an intermediate state emerges, $(h_i, (\phi h)_i)$. The weak form of this system produces two Rankine-Hugoniot jump conditions, which define the shock speeds, ahead and behind the intermediate states. For s_1 , the speed of the shock behind the intermediate state, and s_2 , the speed ahead, these conditions are given by

$$\begin{aligned} s_1 &= \frac{F(h_i, (\phi h)_i) - F(h_l, (\phi h)_l)}{h_i - h_l} = \frac{G(h_i, (\phi h)_i) - G(h_l, (\phi h)_l)}{(\phi h)_i - (\phi h)_l}, \\ s_2 &= \frac{F(h_r, (\phi h)_r) - F(h_i, (\phi h)_i)}{h_r - h_i} = \frac{G(h_r, (\phi h)_r) - G(h_i, (\phi h)_i)}{(\phi h)_r - (\phi h)_i}. \end{aligned} \quad (3.37)$$

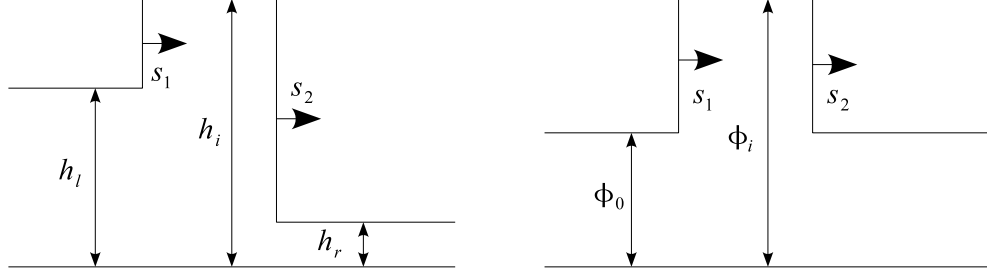


Figure 3.1: The intermediate states that develop in the film thickness (left) and particle concentration (right) for the first-order system of equations.

The intermediate states and shocks can be seen in Figure 3.1. This nonlinear system (3.37) of four equations and four unknowns, h_i , $(\phi h)_i$, s_1 , and s_2 , can be solved via Newton's method. For the simulations shown in Chapter 4, our reference frame speed is an average of the two speeds, $s = (s_1 + s_2)/2$.

The discretization of the terms for the moving reference frame is done explicitly using forward Euler combined with second-order upwind-differencing,

$$-sh_x \approx -s \frac{-h_{i+2,j} + 4h_{i+1,j} - 3h_{i,j}}{2\Delta x}.$$

This was chosen over explicit first-order upwind and implicit centered differencing. For a test run to time $t = 10$ with no variation in the y -direction, implicit centered differencing produced the highest particle-rich ridge, but introduced small oscillations ahead of the flow that were approximately 2% of the height of the ridge. First-order upwind was dissipative and lead to the ridge being 28% smaller than implicit centered differencing. The effects of choosing second-order upwind appear to be some minor dissipation, about 17% as compared to implicit centered differencing, and dispersion, which was not seen in this test case, behind the particle-rich ridge.

The moving reference frame can be used for both the one- and two-dimensional cases (see Figures 3.2 and 3.3). To demonstrate this, simulations were run under the same conditions as those in Chapter 4. The theory-based solution for the problem without higher-order terms (3.33)-(3.36) aligns well with the one-dimensional numerical solution for the full problem. The two-dimensional solution for the full problem with a perturbation to the initial film thickness leads to a finger that moves faster than the one-dimensional case and the troughs, to the sides of the finger, move slower.

This can be viewed more succinctly in Figures 3.4 and 3.7, where the contours of the perturbed two-dimensional case are shown. The position of the finger runs ahead of the one-dimensional front, which is approximately at $x = 15$, while the troughs lag behind. The averaging of the front position was first investigated by Huppert [Hup82] for experiments involving clear fluids. Both simulations start

with the same volume and, after an initial transient, the average front positions for the one- and perturbed two-dimensional case (measured at $h = 0.5$) stay close to each other (Figure 3.5). Figure 3.6 shows the position of the finger and the trough in the two-dimensional case over time.

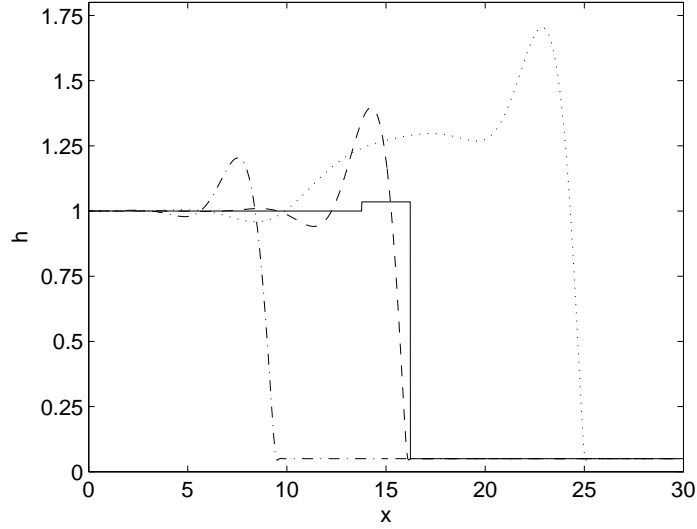


Figure 3.2: Comparison of theory and simulations at time $t = 100$ for the film thickness, h : theory without higher-order terms (solid line), one-dimensional solution to the full problem (dashed line), perturbed two-dimensional finger (dotted line), and perturbed two-dimensional trough (dot-dashed line). The domain in the y -direction is 15 units long, with the finger slice taken at $y = 7.5$ and the trough slice taken at $y = 1$ (see Figure 3.4).

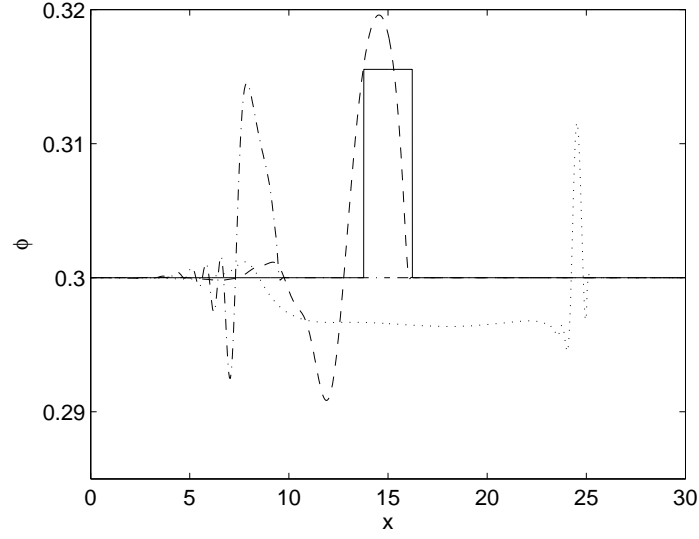


Figure 3.3: Comparison of theory and simulations at time $t = 100$ for the particle concentration, ϕ . The labels are the same as in Figure 3.2.

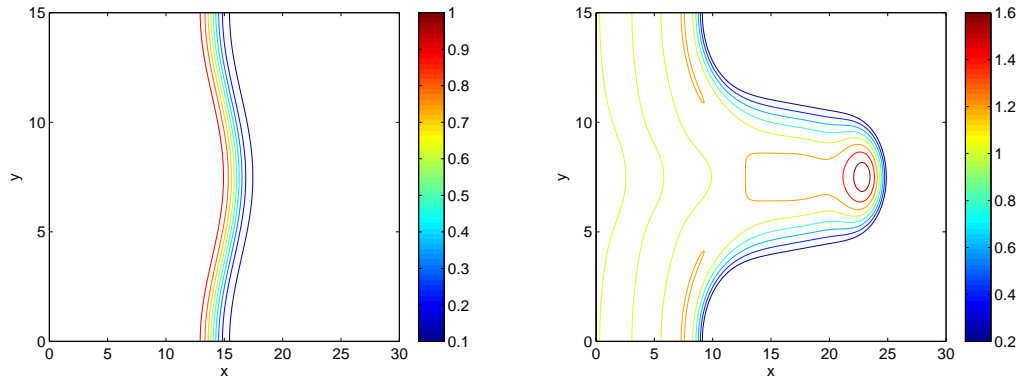


Figure 3.4: A contour plot of the simulation at times $t = 0$ (left) and $t = 100$ (right) for the film thickness, h , in the perturbed two-dimensional case. The perturbation in two dimensions leads to a fingering instability not seen in the one-dimensional case.

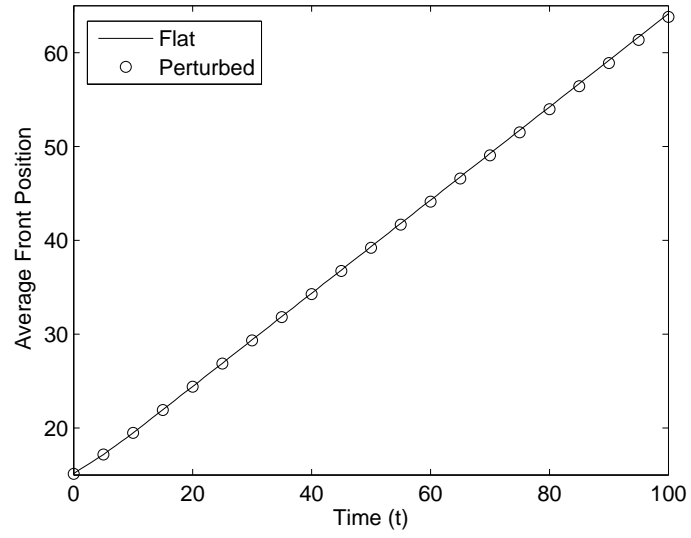


Figure 3.5: The average front position of the film thickness, h , of the one-dimensional and perturbed two-dimensional case up to time $t = 100$. After an initial transient, the average front positions stay close to each other.

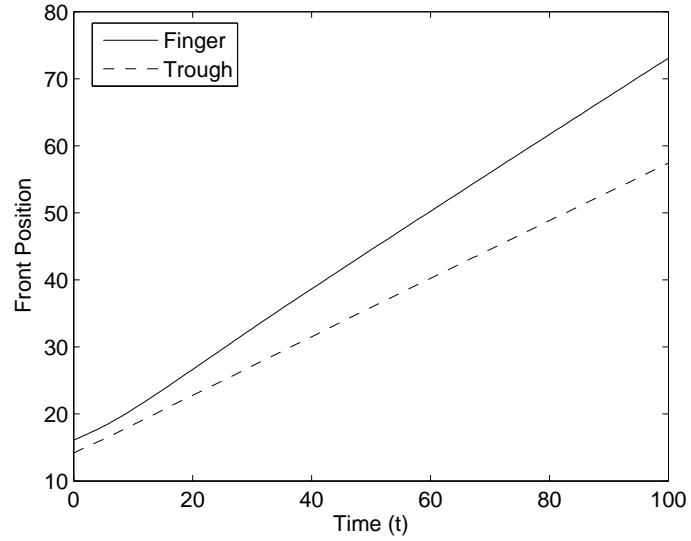


Figure 3.6: The front position of the film thickness, h , of the perturbed two-dimensional case up to time $t = 100$ along the finger and trough.

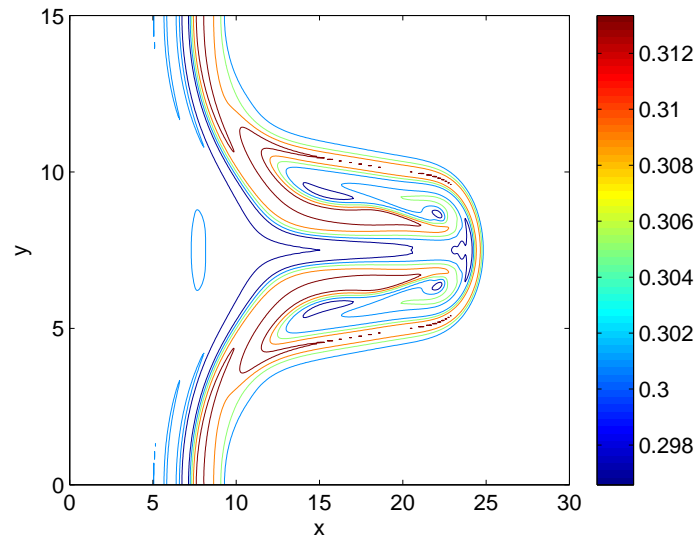


Figure 3.7: A contour plot of the simulation data at time $t = 100$ for the particle concentration, ϕ , in the perturbed two-dimensional case. The perturbation leads to a particle-rich ridge that outlines and begins to fill in the finger.

CHAPTER 4

Simulations and Comparison to Experiments

4.1 Benchmark Simulations

A rectangular domain is used with the x -direction oriented down the inclined plane and the y -direction across the inclined plane. In all cases, the particle concentration is initially taken to be $\phi(x, y, 0) = \phi_0$, where $0 \leq \phi_0 \leq \phi_{\max}$. This corresponds to having a well-mixed initial fluid. The film thickness far behind the contact line is set at $h(x, y, 0) = 1$ and ahead of the flow, a precursor of height $h(x, y, 0) = b$ is assumed. At the contact line, a perturbation to a linear front can be applied to induce behavior such as a fingering instability. The parameters in the model are taken to be: $a = 0.1, \rho_f = 1.7, Ca = 10^{-3}, \alpha = \pi/4$. The constant ϕ_{\max} is taken to be 0.67, in line with the simulations in Cook et al. [CAB09]. The initial timestep is set to $\Delta t = 10^{-6}$ and the mesh width is $\Delta x = \Delta y = 0.05$.

For the model, two sources contribute to the height of the film thickness and particle concentration near the front of the flow. The first is the higher-order terms, such as surface tension, which produce smooth ridges in both h and ϕ . Second, even without these terms, an intermediate state at the front emerges for both variables, higher than either of their respective left or right states. These heights are dependent on the precursor b .

The height of the precursor in the following simulations is chosen to be the same as Δx . In general, the choice of precursor has a small effect on the speed of

the flow, but a large effect on both the film thickness and particle concentration. To illustrate this, Table 4.1 shows the height of the intermediate states for both h and ϕ as well as the speeds of the trailing and leading shocks obtained from the theory-based solution to the system of conservation laws (3.33)-(3.36) (see Section 3.4 for a more in-depth discussion).

b	h_i	ϕ_i	s_1	s_2
0.1	1.01653	0.307566	0.459323	0.510221
0.05	1.03478	0.315538	0.459314	0.483782
0.025	1.07107	0.330331	0.459301	0.471418
0.0125	1.1427	0.356006	0.459289	0.465441
0.00625	1.28276	0.396078	0.459294	0.462488
\vdots	\vdots	\vdots	\vdots	\vdots
0.001	9.14247	0.635545	0.459788	0.459916

Table 4.1: The intermediate states and shock speed solutions from Equation (3.37) based on the precursor thickness b . As the precursor decreases, both h_i and ϕ_i increase and the shock speeds converge.

The intermediate film thickness h_i and particle concentration ϕ_i increase as the height of the precursor b decreases. For the shock speeds, a smaller precursor leads to the trailing shock speed s_1 staying relatively the same, but the leading shock speed s_2 slows down and approaches s_1 . These results agree with the previous ones related to solving the system of conservation laws [CBH08, ZDB05]. For this model, the smallest precursor for which a solution exists is $b \approx 9 \times 10^{-4}$ [CBH08]. A precursor close to this case, $b = 0.001$, produces shocks speeds which are close together and an intermediate particle concentration near the maximum

packing fraction. An alternative settling function that permits solutions with smaller precursors, $f_B(\phi) = (1 - \phi/\phi_{max})^5$, is examined in Cook et al. [CBH08].

The boundary conditions for h are Dirichlet in front and behind, in the x -direction, the flow and Neumann on the sides, in the y -direction. The same is employed for ϕ . In addition, all third derivatives in h , normal to the boundary, are set to 0. More specifically, for a rectangular domain with length X_0 and width Y_0 , the boundary conditions are

$$\begin{aligned} h(0, y) &= 1, \quad h_{xxx}(0, y) = 0, \quad h(X_0, y) = b, \quad h_{xxx}(X_0, y) = 0, \\ h_y(x, 0) &= 0, \quad h_{yyy}(x, 0) = 0, \quad h_y(x, Y_0) = 0, \quad h_{yyy}(x, Y_0) = 0, \\ \phi(0, y) &= \phi_0, \quad \phi(X_0, y) = \phi_0, \quad \phi_y(x, 0) = 0, \quad \phi_y(x, Y_0) = 0. \end{aligned}$$

The simulations are all run using moving reference frames, with the speed of the frame determined as in Section 3.4.

The code is written in parallel using the C++ OpenMP package. This choice of parallelization was made since the majority of calculations are done via *for* loops and OpenMP works well with loop-heavy code. This includes the calculation of all finite differences and the solves along rows and columns associated with the ADI part of the scheme. This is especially useful since rows/columns can be solved independently of each other for each equation. In addition, writing special solvers for linear systems of equations across multiple processors [NS09, PS06] is avoided by this approach. The speed-up attained using N processors is calculated by dividing the runtime for one processor by the runtime for N processors (Speed-Up = Time(1 Processor)/Time(N Processors)).

Based on Figure 4.1, the scaling is close to linear up to 4 processors, with a small drop-off in performance as the number increases. This almost-linear

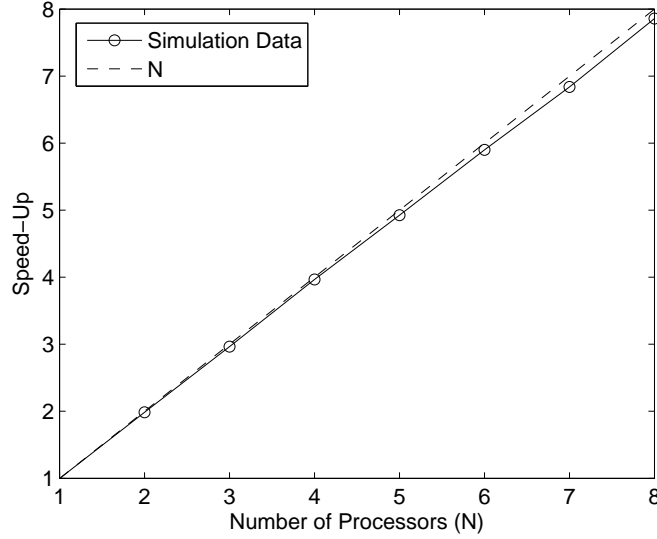


Figure 4.1: The speed-up gained by going from 1 to N processors using OpenMP. The line $y = N$ is shown as a point of reference.

behavior is a result of all of the code, outside of a few minor calculations and the recording of the data, being amenable to parallelization.

To test some preferences that need be chosen a priori in the simulation, we conducted short-time tests to gauge the effectiveness of each approach. The ones considered here are (a) whether to time-lag or extrapolate the approximate terms and (b) whether or not to perform iterations past a single solve to improve the approximate terms, and therefore the solution at each timestep (see Table 4.2).

(a) Approximate Terms	Time-Lagged	Extrapolation
(b) Number of Iterations	One Iteration	Iterations

Table 4.2: The two choices to be made when implementing the numerical scheme. One must choose whether to (a) time-lag or extrapolate the approximate terms and (b) whether or not to perform additional iterations past the initial solve.

Consider an initial condition of $\phi_0 = 0.3$ and a front perturbed from Riemann initial data, $h(x, y, 0) = 1$ far behind the front, $h(x, y, 0) = 0.05$ far ahead of the front. At the jump from fluid to precursor, the shape of the front is given as $x_{\text{front}} = X_0/2 - \cos(2\pi y/Y_0)$. This initial data is then smoothed using hyperbolic tangent and matched to the boundary condition (see Figure 4.4). This has the effect that the initial timestep can be taken more leniently.

We ran this initial simulation for each of the four combinations in Table 4.2 to time $t = 1$ and the maximum timestep allowed, average number of iterations per timestep, and the total runtime, in seconds, are listed in the table below (Table 4.3). This and Table 4.4 provide some global measures to compare the different schemes rather than illustrating convergence studies for any particular method. The choice of $t = 1$ was made as the timestep changes dramatically over this time interval and can provide insight as to which methods seem practical for long-time runs. Since adaptive timestepping is utilized here, the tolerances are tuned so as to ensure that the simulation stays stable, not only to time $t = 1$ but for some time afterwards as well (it is taken up to $t = 100$ in this case, which is the length of the long-run simulations).

	Δt_{max}	Avg. Iter.	Runtime
Time-Lagged and One Iteration	0.000568341	1.0	518.2
Time-Lagged and Iterations	0.00183296	2.20997	601.468
Extrapolation and One Iteration	4.07743×10^{-5}	1.0	19596.1
Extrapolation and Iterations	0.00486338	1.29668	376.603

Table 4.3: Results for time $t = 1$ based on various choices for implementation.

Using *Iterations* performs well for both choices of approximate terms in that the total runtimes are low, the maximum timesteps are large, and the number

of iterations stays close to 1. Between these two, *Extrapolation and Iterations* does best, with nearly one fewer iteration required per timestep, on average, and a runtime that is 37% shorter. Performing *One Iteration*, the runtime for *Time-Lagged* is in between the two cases with *Iterations*, but for *Extrapolation*, it performs poorly, producing a runtime that is 33 to 52 times worse than the other three options. This is due to the small maximum timestep that is associated with this approach, which is 14 to 119 times smaller than the other three. At this point, it makes sense to discard the *Extrapolation and One Iteration* approach due to its excessive runtime and explore the remaining ones.

Under the same conditions, we ran a longer simulation, this time to $t = 100$. Using the best remaining options, we can glean some idea as to which one(s) will work best for a longer simulation.

	Δt_{\max}	Avg. Iter.	Runtime
Time-Lagged and One Iteration	0.00107169	1.0	17811.3
Time-Lagged and Iterations	0.00329173	2.95498	13153.8
Extrapolation and Iterations	0.0106161	2.01204	3364.93

Table 4.4: Results for time $t = 100$.

Comparing Tables 4.3 and 4.4, the maximum timestep for each approach has increased. Using *Iterations*, the average number has gone up for both *Time-Lagged* and *Extrapolation*. However, the average number of iterations per timestep for *Extrapolation* is approximately one iteration fewer than for *Time-Lagged*. Also the runtime takes about 2.9 times longer for *Time-Lagged* compared to *Extrapolation*. One can see the benefit of performing iterations instead of using a smaller timestep in comparing the results for *Time-Lagged and One Iteration* and *Time-Lagged and Iterations*. *Time-Lagged and One Iteration* advances the solution

approximately the same time forward with three timesteps as *Time-Lagged and Iterations* does with one timestep and three iterations. However, doing two extra timesteps costs more than two extra iterations, as seen in their respective run-times. This is because the explicit terms do not need to be re-calculated for each iteration while they do for each timestep. Therefore, the only two options which make sense to use are the ones involving *Iterations*. Of these, *Extrapolation* is the clear favorite.

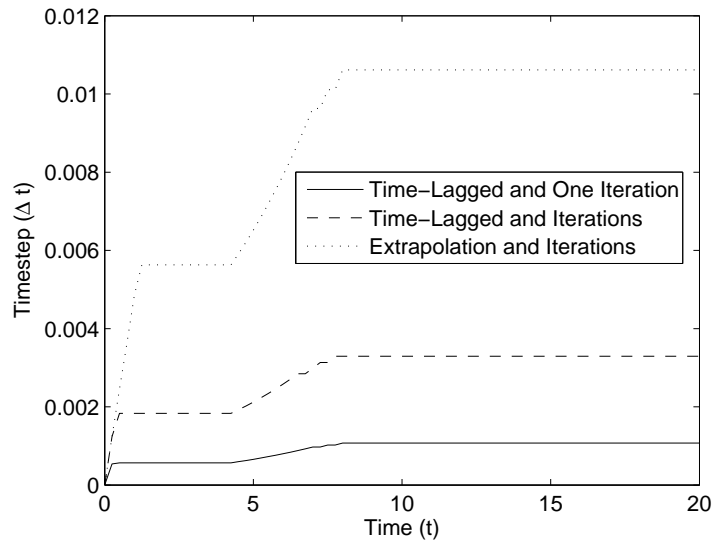


Figure 4.2: The adaptive timestep up to time $t = 20$. The timestep, Δt , is recorded in intervals of 0.25 for the three cases. *Extrapolation and Iterations* has a significantly larger timestep than either *Time-Lagged and One Iteration* or *Time-Lagged and Iterations*.

In Figure 4.2, we see that by time $t = 8$, all three approaches have settled into a respective timestep. The timestep for *Extrapolation and Iterations* does best, followed by *Time-Lagged and Iterations* and *Time-Lagged and One Iteration*. The timestep for *Extrapolation and Iterations* is 3.2 times better than *Time-Lagged and Iterations* and 9.9 times better than *Time-Lagged and One Iteration*. The

benefit of the larger timestep for both approaches with *Iterations* is partially offset by the need for extra calculations related to the iterations.

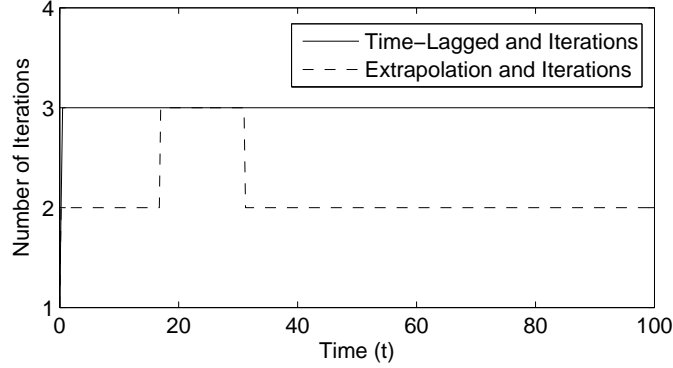


Figure 4.3: The number of iterations up to time $t = 100$. The iterations are recorded in intervals of 0.25 for the two cases. Using *Extrapolation and Iterations* does better than *Time-Lagged and Iterations* in terms of fewest number of iterations.

Figure 4.3 shows the number of iterations required throughout the simulation. For *Extrapolation and Iterations*, the increase in iterations approximately between times $t = 20$ and $t = 30$ corresponds to the finger forming and stretching out ahead of the flow in the film thickness and the particle-rich ridge growing higher and outlining the finger. While the number of iterations jumps once to 3 and then back down to 2 for *Extrapolation and Iterations*, it remains constant at 3 for *Time-Lagged and Iterations*. The cost of storing extra data and performing a small computation to find the extrapolated approximations seems a small price to pay to save one iteration per timestep, which includes recalculating values involving the approximate terms and performing the ADI solves.

Using the simulation data up to $t = 100$, we can examine the effects of the initial perturbation graphically. For the film thickness, a small capillary ridge forms in the center of the perturbation (Figure 4.5) and begins to stretch out

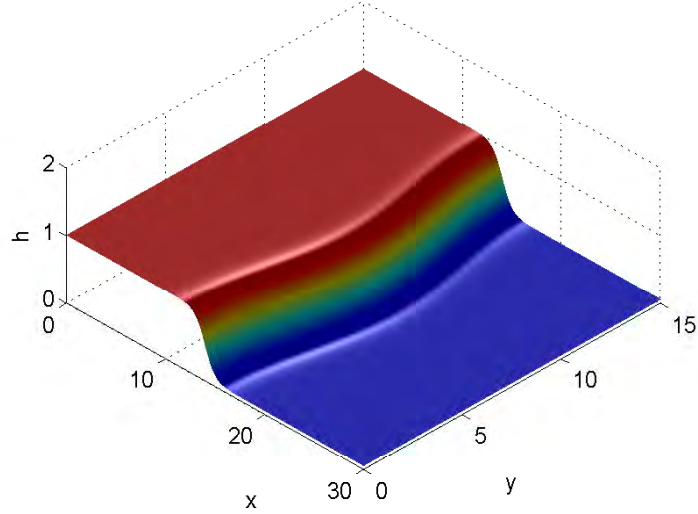


Figure 4.4: The initial film thickness. It is perturbed by a cosine wave along y and smoothed along x by hyperbolic tangent.

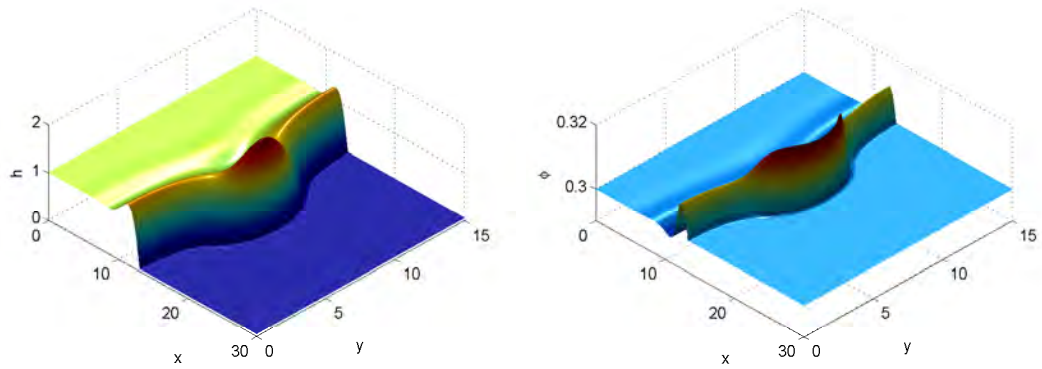


Figure 4.5: Film thickness (left) and particle concentration (right) at time $t = 25$. A small ridge forms in both, with the highest point in the perturbation.

ahead of the bulk flow (Figures 4.6 and 4.7). This is the well-known fingering instability present in thin film flows. For the particle concentration, a particle-rich ridge initially forms at the contact line (Figure 4.5) and, as the fingering instability evolves, outlines the shape of the finger (Figures 4.6 and 4.7). Directly

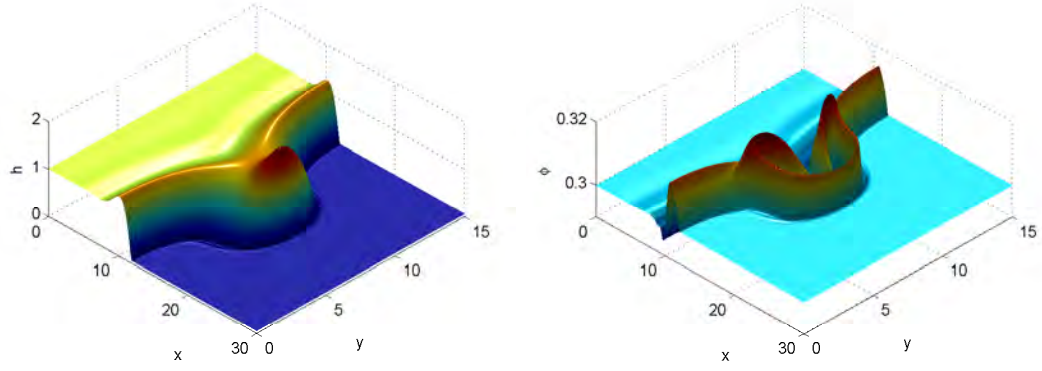


Figure 4.6: Film thickness (left) and particle concentration (right) at time $t = 50$. A fingering instability and particle-rich ridge form.

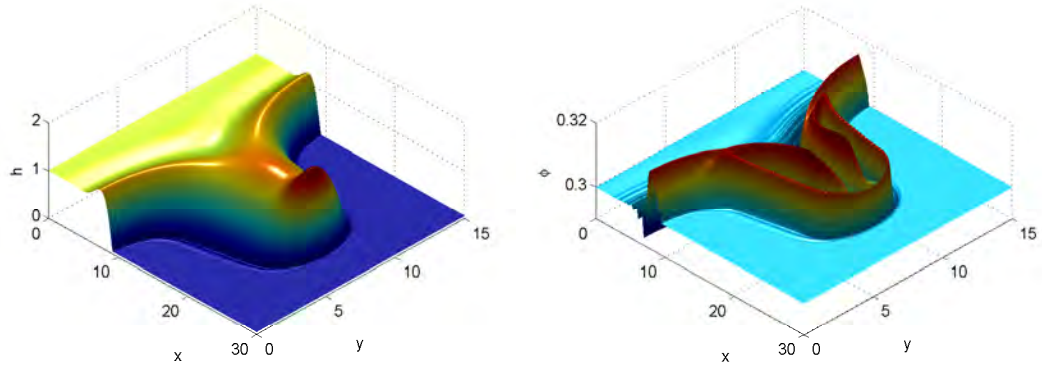


Figure 4.7: Film thickness (left) and particle concentration (right) at time $t = 100$. The fluid finger stretches out ahead of the bulk flow. The particle-rich ridge increases in concentration and has a higher concentration in and around the fingering instability.

behind the ridge, a pocket of lower concentration forms. The interior of the finger is slowly encroached upon by the particles that have accumulated near the back and sides of the finger. This can be seen in Figure 4.7 as an interior layer along the inside of the particle-rich ridge. It is possible that this phenomenon

is not physical, meaning that it occurs only in the simulations and not in the experiments, and may be a result of the current model not containing all of the necessary physics.

4.2 Comparison to Experiments

Experiments for constant-volume particle-laden thin film flows have been compared in one dimension to the solution, both analytically and numerically, for constant-volume clear fluid flows. The average front position for clear fluids is given by a power law, where the location of the front scales like $Ct^{1/3}$, where C is a scaling constant [Hup82]. Ward et al. [WWG09] compare the average front position of the flow to this scaling and find agreement for particle concentrations below $\phi = 0.45$ and deviations at later times for higher concentrations. Grunewald et al. [GLM10] compare the average front position to a re-derived one-dimensional model, based on results from Huppert [Hup82] with a precursor, and to experiments and numerical solutions of the one-dimensional problem. The $Ct^{1/3}$ scaling appears valid for concentrations of 0.25 to 0.45, and the scaling constant for experiments and numerics are within 20% of the theoretical constant (see Chapter 5 for a full discussion). We seek to compare the numerical solution in two dimensions to images of experiments, taking into account that variations occur across the front of the flow.

We use 1000 cSt polydimethylsiloxane (PDMS), a silicone oil, for the liquid component of the fluid. For the particles, glass beads with diameters in the range of $250 - 425 \mu\text{m}$ are used. The two components are then well-mixed and released down an inclined plane from a reservoir. This corresponds to a constant-volume experiment, whereas our simulations are constant-flux. The approximation of a constant-volume problem by a constant-flux one may be invalid at early times,

as the height of the fluid will be changing rapidly. However, the height of the flow changes slower at later times, at which point a constant-flux approximation may be valid.

The experiment, which we will compare to simulation, is a fluid of approximately 90 cm^3 containing a volume which is 35.9% particles. The plane is inclined at a 32-degree angle. The fluid is allowed to flow down the plane, which is 14 cm across and 90 cm down. In the experiments, the flow starts out close to uniform across the front, away from the edges, and over time develops instabilities, in the form of fingers stretching out ahead of the bulk flow. Since, for simulations, starting with a uniform front along the y -direction leads to a uniform solution, we start the simulation some time after the start-time to add a perturbation to the initial data, which induces the type of behavior seen in the latter stages of the experiments.

In order to avoid simulating the problem over the entire domain, we truncate the solution near the front and treat the problem locally as being constant-flux. We are interested in the dynamics of finger formation during which time the film thickness only changes by at most 20% , so a local approximation by constant-flux is reasonable.

We use two images, taken three minutes apart, to compare with the simulation (Figures 4.8 and 4.10). The first image is taken when the front of the flow has reached approximately 53 cm down the plane. The shape of the front is parabolic-like with two large perturbations at either end of the front. In between, smaller perturbations exist which lead to fingering instabilities. The two outer perturbations lead to longer and thicker fingers than the smaller inner perturbations. We take a front similar to this in our simulation.

The scales for a constant-flux problem can be taken from Cook et al. [CBH08],

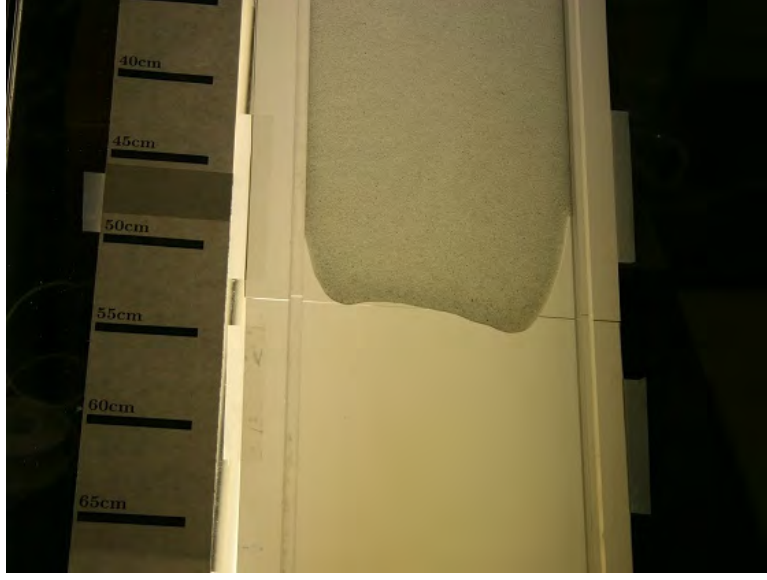


Figure 4.8: The initial condition of the experiment, used for comparing with the simulation. At this point, the front of the flow has begun to develop perturbations, which will lead to fingering instabilities.

which are the same as for the clear fluid case. The height scale is taken to be $h_0 = 1$ mm. The length scale is $x_0 = (l^2 h_0)^{1/3}$, where the capillary length, l , is $l = \sqrt{\gamma / \rho_l g_{\parallel}}$. The constants are γ , the coefficient of surface tension; ρ_l , the liquid density; and g_{\parallel} , the component of gravity parallel to the inclined plane. The time scale is $t_0 = (3\mu_l / \gamma) x_0 l^2 / h_0^2$, where μ_l is the dynamic liquid viscosity. The capillary number is given by $Ca = \mu_l x_0 / \gamma t_0 = h_0^2 / 3l^2$.

The scales, given these parameters, are $h_0 = 0.001$ m, $x_0 = 0.00161396$ m, $l = 0.00205041$ m, $t_0 = 0.93235$ s, and $Ca = 0.0792863$. Using this, we can construct an initial condition which resembles the experiment and will produce similar results. This is done by measuring the features of the initial image and creating a similar condition. While the flow in the experiment is asymmetric, we take a symmetric initial condition in the simulation which has features that are

approximately, in both location and size, the same as in the experiment. The track is taken to be 86.75 units wide (rounded up to the nearest 0.05 increment, which is the value of $\Delta x, \Delta y$), which corresponds to the 14 cm wide track. The precursor in the simulation is set to $b = 0.05$, as in the previous simulations.

A moving reference frame is used since this is taken to be a constant-flux problem locally. The speed of the moving reference frame is approximately $s = 0.343198$, calculated as in Section 3.4. Running a simulation over the course of three minutes leads to a distance traveled for the frame of approximately 10.69 cm, where the actual displacement, based on the experiment, is around 12 cm, so using the constant-flux assumption seems to produce a decent approximation of the distance the fluid will flow.

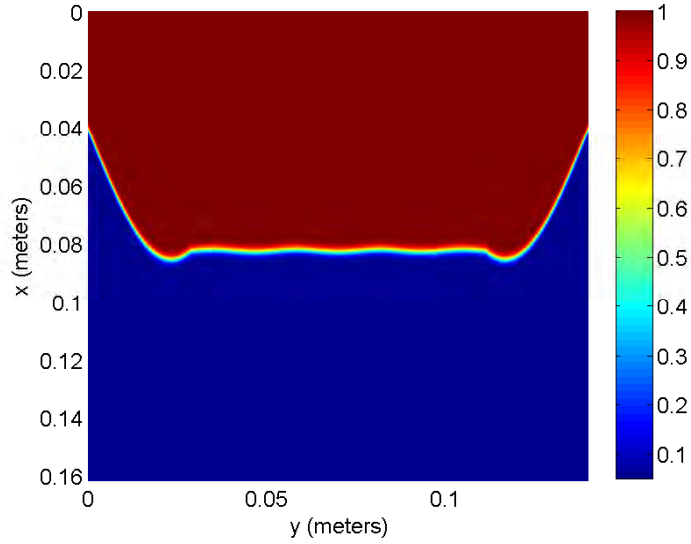


Figure 4.9: The initial condition for the film thickness, h , used in the simulation. This is an artificially-created starting condition to be representative of the state shown for the experiment. The height is in mm.

The initial data is generated using a sine wave to form the two large perturba-

tions and the space away from the edges. The three fingers that develop between these two perturbations are simulated with a cosine wave of small amplitude, 0.25 in dimensionless units (Figure 4.9). The simulation is run to $t = 193.06$, the equivalent of three minutes of real-time.

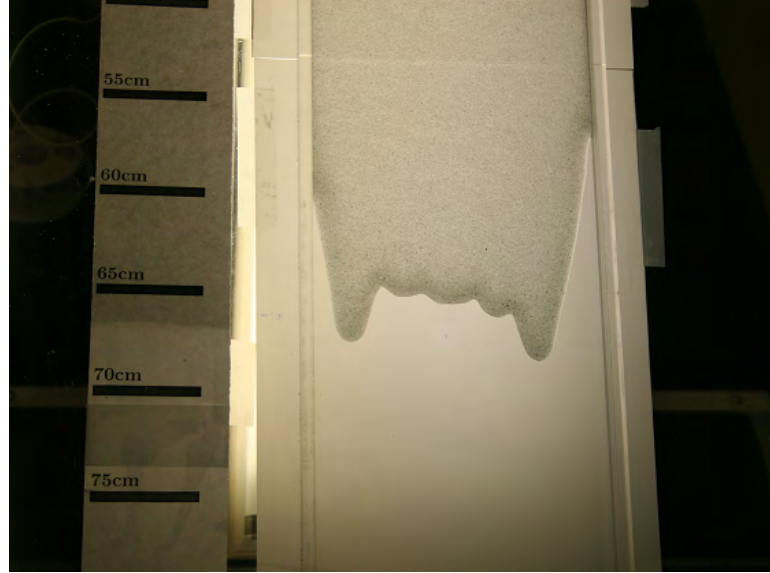


Figure 4.10: The evolution of the experiment after three minutes. The fingering instability starts to form at the front.

Over the course of the three minutes, the exterior of the outer fingers in the experiment go from 4 cm and 6.5 cm on the left and right, respectively, to 7.5 cm and 12 cm. The interior of these fingers go from less than 1 cm on each side to about 3 cm. The interior fingers are not discernable in the initial image. The flow as a whole, measured from where the fluid touches the walls, has moved about 11 cm down the plane. The interior fingers in the experiment extend about 0.5 cm ahead of the flow.

In the simulation (Figure 4.11), the moving reference frame accounts for 10.69 cm of movement, so the position where the fluid touches the edges has

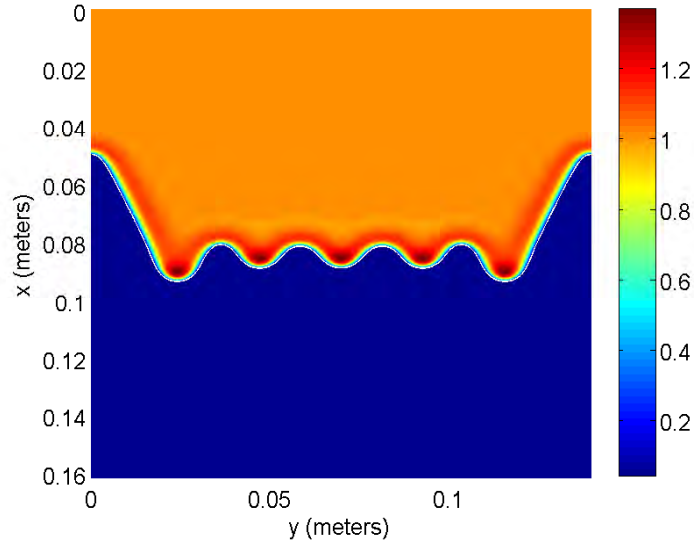


Figure 4.11: The evolution of the film thickness, h , in the simulation after three minutes. Both the experiment and simulation exhibit a fingering instability, but the instability in the simulation is less pronounced. The height is in mm.

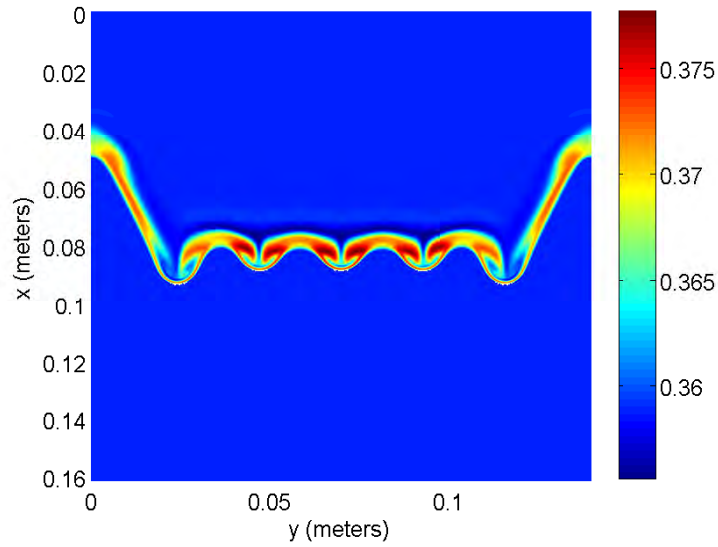


Figure 4.12: Particle concentration, ϕ , for the film thickness in Figure 4.11.

moved approximately 11.4 cm. The evolution of the fingers in the simulation is slightly less pronounced than in the experiment. This is likely due to the simulation initially undergoing a transient state where the fluid travels slower than at later times, while the transient in the experiment has occurred prior to this three-minute interval. The exterior of the outer fingers is approximately 4.2 cm and interior 1.2 cm. The interior fingers extend ahead of the flow about 0.8 cm. The tip of the longest finger in the experiment has moved 15 cm while in the simulations, it has advanced approximately 11.4 cm. The tips of the fingers, in the z -direction, reach up to 1.37 mm.

The particle concentration cannot be determined accurately at the particle-rich ridge in the experiment, but the increased opacity at the leading edge of the flow indicates an increase in the concentration, relative to the ambient concentration. This change in shade is approximately 1 cm long in the direction of the flow. In the simulation (Figure 4.12), the thickness of the ridge ranges from 0.6 to 1.1 cm, which is consistent with the experiment.

4.3 Summary

Schemes originally derived for numerically solving high-order parabolic problems have recently been extended to high-order systems, such as the case of surfactants and particle-laden thin films. Handling the higher-order terms in a practical way is necessary for fast and efficient computation. The scheme we have presented in Chapter 3 for particle-laden thin film flow provides an easy-to-program and effective way to solve this high-order coupled system. This scheme can provide a blueprint for approaches to solving similar problems.

The numerical scheme developed for particle-laden thin film flow has several

nice attributes. The timestep required for this scheme is in the range of $O(\Delta x^2)$, which is much better than the $O(\Delta x^4)$ for a fully explicit scheme. The structure of the scheme allows for the possibility of solving each equation with its own unique timestep for better efficiency, as the particle concentration is typically the equation that fails the timestep restriction criteria. The linear algebra problem that results from an implicit time discretization along with the nonlinearity is reduced to a series of tri- and pentadiagonal solves, which can be done in parallel along the rows/columns of the grid.

The parallelization of the code is straightforward using OpenMP. The loops for computing the explicit and approximate terms as well as the solves along rows and columns can be done in parallel, leading to a code that scales close to linearly for up to 8 processors, getting close to 8 times speed-up. Adding OpenMP implementation to C++ code on any multicore machine is easy to implement, as it only requires adding a few lines of code to existing *for* loops and needs no managing of the movement of data on the programmer's part. Since the code is predominantly such loops, it is easy to parallelize and is highly effective in getting better runtimes.

Implementing *Iterations* within each timestep, which is first presented in Witeliski and Bowen [WB03], but not used in Warner et al. [WCM05], seems to work best for this problem, in terms of allowing for a larger timestep and producing an accurate solution. Among the choices for the approximate terms when performing *Iterations*, *Extrapolation* seems to produce the best runtime and fewest iterations. Implementation requires only storing an extra set of data used in extrapolating the approximate terms but, using the adaptive timestepping discussed here, this data is stored anyway.

The choice of *Extrapolation and Iterations* may work best for this problem,

but for other problems or initial conditions, another choice may fare better. It is recommended, as in this case, that a short-term simulation be performed for the different choices of approximate terms and whether or not to perform extra iterations. The small cost of these short runs may allow for a more efficient run for actual simulations. It is also recommended that one examines the results to make sure that the scheme is not only fast with the choice, but sufficiently accurate.

The numerical solution agrees reasonably well with the behavior seen in experiments. This is in part because the model was derived for the case when a particle-rich ridge forms. This is seen in the experiments for high angles of inclination and high concentrations, but will occur in the model for all concentrations and angles. The particle-rich ridge in the simulations is two thin layers of particles, one which originates at the front of the flow and the other from the troughs of the emerging fingers, which may not be physical.

The current model assumes a constant, or average, particle concentration throughout the fluid layer in the z -direction. The same is true for the velocity, which is averaged in the z -direction. Theory exists for the vertical movement of the particles [Coo08], whether they will settle to the inclined plane or form a ridge, and incorporating this behavior into a new model is the current research of the authors. It is hoped that the current numerical scheme will be adaptable to this new model.

CHAPTER 5

Self-Similarity of Particle-Laden Flow at Constant Volume

This chapter compares the behavior of a constant-volume particle-laden fluid flow down an incline with a clear fluid flow. We compare the analytical solutions of the clear fluid flow to both physical experiments and numerical simulations of the particle-laden fluid flow, using a model proposed in Cook et al. [CBH08] and Zhou et al. [ZDB05].

In Huppert [Hup82], a simple scaling law is derived for the average front position $x(t) \sim Ct^{1/3}$ in the case of clear fluids. Comparison to both the particle-laden flow lubrication model and to physical experiments suggests that the Huppert scaling law is still valid to leading order for particle-laden fluids with moderate particle concentrations in the range 25-45%. In this range, the particle-laden fluid still behaves fluid-like, and settling of the particles is present but does not dominate the large-scale dynamics. The effects of settling in the direction of the flow can be visually observed in the experiments as a particle-rich ridge at the leading edge of the flow. We compare different settling functions in our model to analyze this effect numerically. We also note that the lubrication models with settling require a precursor; they are singular at vanishing precursor [CBH08, ZDB05]. Thus, it makes sense to compare the dynamics of the lubrication model with settling to an exact solution of the problem without settling and with precursor.

5.1 One-Dimensional Lubrication Model

The flow of a particle-laden fluid down an inclined plane has been modeled by a system of conservation laws [CBH08, Coo07],

$$h_t + (hv_{\text{tot}})_x = 0, \quad (5.1)$$

$$(\phi h)_t + (\phi h v_p)_x = 0. \quad (5.2)$$

This is similar to the system of conservation laws (3.33)-(3.34) in Section 3.4. The total volume of the fluid is conserved in (5.1), where $h(x, t)$ is the height of the liquid-particle mixture at position x (oriented down the inclined plane) and time t . We assume uniformity in the transverse direction. The total volume of particles ϕh is conserved in (5.2), where ϕ is the particle concentration in the fluid. The average velocity of the fluid v_{tot} is a depth-average as well as a volume-average of the speeds of the liquid and the particles. The velocity of the particles v_p consists of v_{tot} and an extra term $(1 - \phi)v_{\text{rel}}$ due to the sedimentation of the more dense particles in the fluid:

$$v_p = v_{\text{tot}} + (1 - \phi)v_{\text{rel}}.$$

We assume that the particle concentration ϕ is uniform in the direction perpendicular to the inclined plane. It is shown in Cook [Coo08] that this assumption can be improved to a distribution that is stationary in time which balances sedimentation and shear-induced migration. We refer to Cook [Coo08] for a precise discussion. The depth-average of the velocity of the fluid, v_{tot} found in (5.1), can then be derived via standard techniques in lubrication theory for thin liquid films

[Coo07], which is valid for fluids with small Reynolds numbers and characteristic height much smaller than the characteristic length. The first-order term describes its dominant behavior as:

$$v_{\text{tot}} = \frac{\rho(\phi)}{3\mu(\phi)} h^2 g_{\parallel}. \quad (5.3)$$

Note that the terms discussed in this chapter (e.g., $\rho(\phi), \mu(\phi), \dots$) have not been nondimensionalized. Following the modeling suggested in Krieger [Kri72] and Stickel and Powell [SP05], we model the viscosity with the empirically derived model

$$\mu(\phi) = \mu_l (1 - \phi/\phi_{\text{max}})^{-2} \quad (5.4)$$

with dynamic liquid viscosity μ_l . The value ϕ_{max} is as defined in Chapter 2. We use $\phi_{\text{max}} = 0.58$, which is our experimentally determined value [WWG09]. This value is also used in the literature; see e.g., [ZHL00]. The density is a linear combination of the density of the liquid ρ_l and the density of the particles ρ_p

$$\rho(\phi) = \rho_l (1 - \phi) + \rho_p \phi.$$

The other constant in (5.3) is the component of gravitational acceleration $g_{\parallel} = |g| \sin \alpha$, where α is the inclination angle of the plane.

The velocity v_p in the second conservation law (5.2) requires a more explicit description, since the theory for particle-laden flow is still relatively novel and continues to present many open questions, especially for shear-driven flows. Recall that the lubrication approximation used to derive (5.3) employs a depth-averaged velocity. We also employ a depth-averaged model for v_{rel} as in Chapter 2, which we assume is a product of three factors:

$$v_{\text{rel}} = V_s f(\phi) w(h). \quad (5.5)$$

The Stokes settling velocity V_s is given as:

$$V_s = \frac{2}{9} \frac{(\rho_p - \rho_l) g_{\parallel} a^2}{\mu_l}.$$

The other factors account for phenomena that reduce the speed of a single particle: hindered settling from adjacent particles and slowing due to proximity of particles to the substrate.

A classical model for hindered settling was proposed by Richardson and Zaki [RZ54a] and Buscall et al. [BGO82]:

$$f(\phi) = (1 - \phi/\phi_{\text{max}})^m \quad (5.6)$$

with $\phi_{\text{max}} = 1$ and empirically determined exponent $m = 5.1$. Cook [Coo07] modified the function to include the maximum packing fraction of particles ($\phi_{\text{max}} = 0.67$ in their case) to avoid singular shocks in solutions to the Riemann problem for (5.1) and (5.2) that occur when $\phi_{\text{max}} = 1$. This form also ensures that sedimentation stops once the maximum concentration is reached. We will compare results for $m = 1$ and $m = 5$ to probe the effect of the exponent in the hindered settling function. This is particularly relevant when comparing numerical results and physical experiments, since the division by the maximum packing fraction may have altered the appropriate choice of exponent for comparison to experiments. Note that, although the singular limits for both functions

$$\lim_{\phi \rightarrow \phi_{\text{max}}} f(\phi) = 0, \quad \lim_{\phi \rightarrow 0} f(\phi) = 1,$$

are appropriate, we will not consider extreme values of ϕ , since the comparison to experiments is most appropriate for moderate concentrations of particles.

The third factor in (5.5) models the slowing of particles due to their proximity to the substrate, called the wall effects function [ZDB05, Coo07] (see Chapter 2). The full system of equations for $h(x, t)$ and $\phi(x, t)$ is now fully specified by incorporating (5.3) into (5.1) and (5.5) into (5.2).

As has been shown for clear fluids [BB97], a first-order model such as the one proposed here can correctly capture quantities such as front speed but does not contain the physics necessary to model fingering due to surface tension and the component of gravity normal to the substrate. Numerical evidence in Cook [Coo07] for constant-flux boundary conditions indicates that higher-order terms smooth solutions but do not affect the speed of the leading front of the film. Nevertheless, quite a lot of information can be gained by studying the dominant physics in the flow direction, in particular with regard to the competition between settling of particles and overall motion of the fluid.

Nondimensionalizing the reduced system with length scale h_0 (half of the upstream gate height) and time scale $t_0 = (\sin \alpha)t$, we obtain

$$h_t + \left(\frac{g\rho(\phi)}{3\mu(\phi)} h^3 \right)_x = 0, \quad (5.7)$$

$$(\phi h)_t + \left(\frac{g\rho(\phi)}{3\mu(\phi)} \phi h^3 + V_s \phi h (1 - \phi) f(\phi) w(h) \right)_x = 0, \quad (5.8)$$

which we solve numerically and compare to experimental results. This nondimensionalization is slightly different than the one given for the two-dimensional system in Chapter 2. Note that this system has been studied for constant-flux boundary conditions [Coo07]. Since the physical experiment (described in Sec-

tion 5.3) more closely resembles a constant volume of particle-laden fluid than a constant flux (for the purpose of numerical simulations), we will choose initial conditions to approximate a constant volume of fluid.

5.2 Well-mixed similarity theory including precursor

We begin our discussion of similarity solutions by considering a model for a well-mixed fluid flow down an inclined plane. Let ϕ_0 be the initially constant particle concentration in the fluid. For a well-mixed fluid without particle settling, the concentration stays constant in space and time. We compare the settling model (5.7) and (5.8) to solutions of the well-mixed model:

$$h_t + \frac{g\rho}{3\mu} (h^3)_x = 0, \quad (5.9)$$

with

$$\rho = \rho(\phi_0) \text{ and } \mu = \mu(\phi_0).$$

This model from Huppert [Hup82] captures the dominant behavior of the flow with no particles. For simulations with no precursor, the solution of (5.9) for an initial fluid profile

$$h(x, 0) = \begin{cases} \beta, & 0 \leq x \leq L, \\ 0, & \text{otherwise} \end{cases}$$

can be solved explicitly. We consider (5.9) in its natural time scale

$$\tau = \frac{g\rho_0}{3\mu_0} t.$$

After an initial transient time $\tau \geq \tau^\star = \frac{3L}{2\beta^2}$ a similarity solution

$$h(x, \tau) = \begin{cases} \sqrt{x/\tau}, & 0 \leq x \leq x_s(\tau), \\ 0, & \text{otherwise} \end{cases}$$

develops with

$$x_s(\tau) = \left(\frac{3}{2}\beta L\right)^{2/3} \tau^{1/3} = Ct^{1/3}, \quad (5.10)$$

where

$$C = \left(\frac{3}{2}\beta L\right)^{2/3} \left(\frac{g\rho_0}{\mu_0}\right)^{1/3}. \quad (5.11)$$

The constant C , when measured experimentally, provides a method for measuring the effective viscosity of the fluid by inverting (5.11)

$$\mu = \frac{9}{4}\beta^2 L^2 g\rho_0 C^{-3}.$$

The effectiveness of this quantity as a measure for bulk viscosity of the particle-laden fluid is explored in Ward et al. [WWG09]. For comparison between numerical experiments and simulations, we focus on the variation in the scaling constant C for experiments with and without particles.

It is also possible to consider analytical solutions of (5.9) with a small uniform precursor layer of height b . We consider (5.9) with Riemann initial data

$$h(x, 0) = \begin{cases} \beta, & 0 \leq x \leq L, \\ b, & \text{otherwise} . \end{cases}$$

The discontinuity in the initial data at $x = 0$ will immediately become a rarefaction, while the shock at $x = L$ will persist. At a critical time

$$\tau_c = \frac{L}{\beta^2 - (1/3)(\beta^2 + \beta b + b^2)},$$

the trailing rarefaction and leading shock will merge, creating a wedge shape that continues to evolve in time above the precursor. The shape of this profile can be described analytically [Lax73, Eva98]. Above the precursor the solution still has the shape of $\sqrt{x/\tau}$. The excess volume above the precursor

$$V = L(\beta - b) \tag{5.12}$$

remains constant. One can therefore use the conservation of volume to determine the speed of the shock. Let x_s be the position of the shock. Then

$$\int_{b^2\tau}^{x_s} \sqrt{x/\tau} dx - b(x_s - b^2\tau) = V.$$

Therefore the shock position is defined implicitly by the solution of

$$\frac{2}{3} \left(x_s \sqrt{x_s/\tau} - b^3\tau \right) - b(x_s - b^2\tau) - V = 0. \tag{5.13}$$

and the solution of the double Riemann problem with precursor after τ_c is

$$h(x, \tau) = \begin{cases} b, & x < b^2\tau, \\ \sqrt{x/\tau}, & b^2\tau < x < x_s, \\ b, & x > x_s. \end{cases} \tag{5.14}$$

To explore the difference in evolution of the solutions analytically, let

$$H = \sqrt{x/\tau} \quad (5.15)$$

be the maximum height of h . Rewriting (5.13) in V and H gives:

$$\frac{2}{3}H^3 - V/\tau = bH^2 - b^3/3.$$

This illustrates by (5.15) and (5.12) that, as long as $b \ll H$, the right-hand side is negligible and x_s approximates the shock position of the solution without precursor (5.10). Figure 5.1 shows the deviation of the shock positions. The data start from time τ_c after which (5.13) is valid. For increasing time and precursor, the relation $b \ll H$ gets less valid and therefore the deviation of the shock positions increases. Note that for the settling model the limit $b \rightarrow 0$ is singular [ZDB05, CBH08]. We therefore have to introduce a precursor for the numerical simulations.

5.3 Experimental Results

The experimental apparatus consists of a 90 cm long, 50 cm wide acrylic sheet mounted to an adjustable stand capable of inclination angles ranging from 5° to 80° (see Figure 6.1). Down the length of the sheet is a track approximately 14 cm wide. Side walls, approximately 3.2 cm high near the top and 1.4 cm near the lower part of the track, are designed so the fluid does not escape over the sides. Near the top of the acrylic sheet is a gated reservoir from which a finite well-mixed volume of liquid and particles is released.

The experiments shown are all conducted at an inclination angle of 45° and particle concentrations of 25-45%, in increments of 5%. For these values, we avoid the rapid settling of the particles toward the substrate associated with low

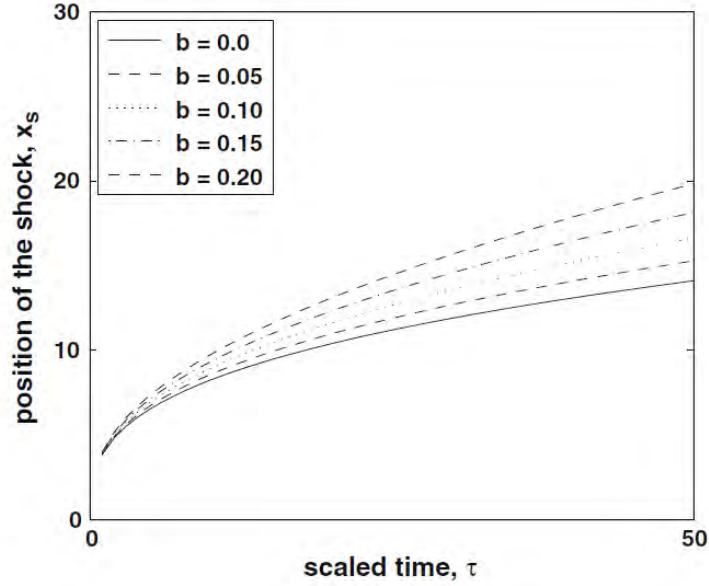


Figure 5.1: Comparison of front position for different precursor heights, at $L = 2.5$, $\beta = 2$ and $\phi = 0.4$.

concentrations and low inclination angles which leads to deposits of particles at the rear of the flow and clear fluid fingers at the leading edge. We also avoid particle jamming, clumping, and sliding that is associated with higher particle concentrations and higher inclination angles. Additional experimental data have been collected for other inclination angles [WWG09]; but the data presented here for 45° provide representative results.

The particle-laden fluid is a mixture of 1000 cSt silicone oil (Clearco Products) with a density of approximately 0.96 g/cm^3 , and soda-lime glass beads (Ceroglass) with a density of approximately 2.5 g/cm^3 . The diameter of the beads is 0.025 cm . For smaller particles, the settling in the direction of the flow to form a particle ridge at the front is less evident.

This experimental setup has a Péclet number Pe on the order of 10^{10} , with

$Pe = V_s a / D$ where $V_s = (2/9)(\rho_p - \rho_l)g_{\parallel}a^2/\mu_l$ is the settling velocity, a is the particle radius, and $D = k_b T / 6\pi\mu_l$ is the diffusivity with Boltzmann constant k_b and temperature T . We note that a high Péclet number in the experiments suggests that we may neglect Brownian motion in the derivation of the model.

The maximum packing fraction of beads is determined experimentally as described in Ward et al. [WWG09]. The value of ϕ_{\max} is measured to be approximately 0.57-0.58. Each preparation of particle-laden fluid has a constant volume of 90 cm³ with approximately 70 cm³ actually being transferred from the jar into the reservoir. The particle-liquid mixture is prepared according to the desired concentration of beads and silicone oil.

To begin the experiment, the particle-laden flow materials are placed in a plastic container and hand-mixed using a stirring rod for 4 minutes, creating a homogeneous mixture. Since the density of the particles is greater than that of the liquid, the particles settle out fairly quickly and the experiments must be performed immediately after the particle-laden fluid is well-mixed. The fluid is placed in the reservoir and the gate is opened. A camera positioned above the track and perpendicular to the inclined plane records still images at predetermined time intervals. The images for the 25 and 30% particle concentration experiments are recorded at 4 fps (frames per second), the 35 and 40% at 2 fps, and the 45% at 1 fps.

The images are analyzed by an image-processing code and an average front position is calculated for each image. Figure 5.2 shows a time-series of images taken at 45 second intervals. In these images, the development of the fingering instability and a dark particle-rich ridge at the front of the fluid can be observed. Figure 5.3 contains a series of plots each taken two minutes into the experiment for a range of particle concentrations. Note that the fluids with more particles

move more slowly, and have a darker particle ridge at the front.

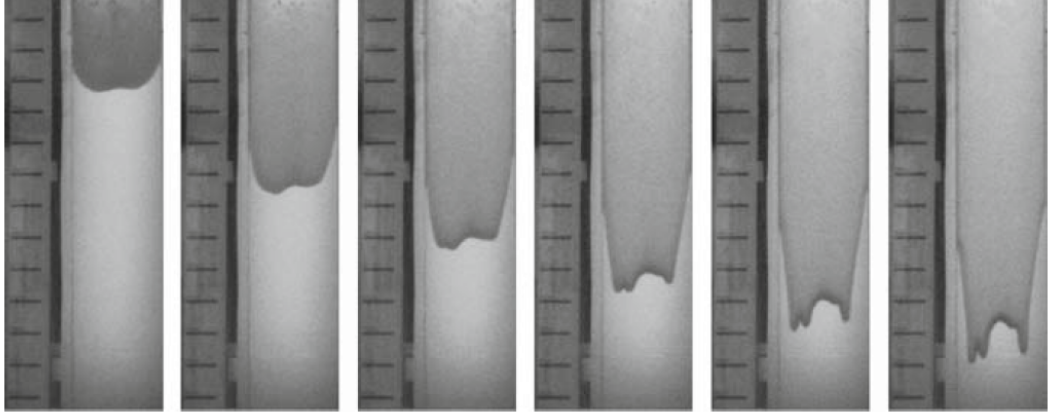


Figure 5.2: Time series 45 seconds apart, 35% particle concentration, 45° inclination.

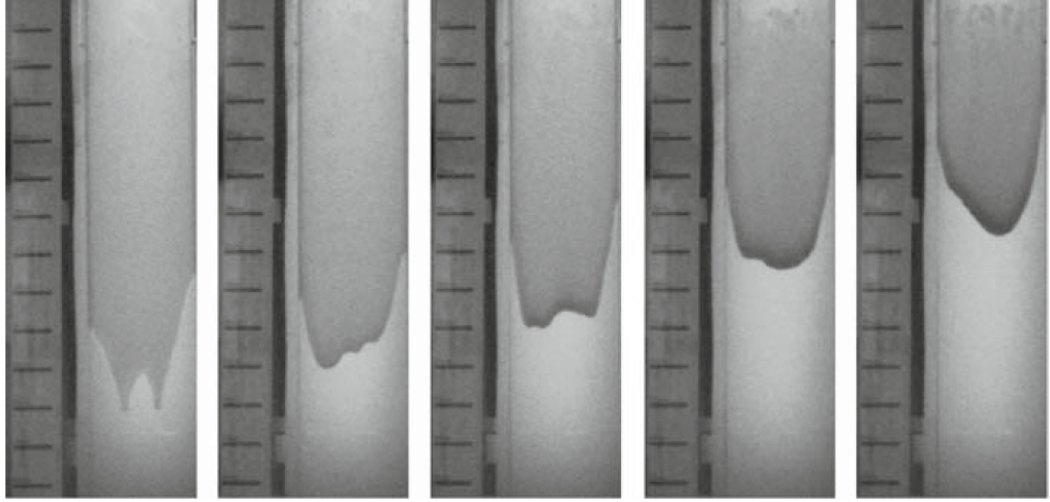


Figure 5.3: Varying particle concentrations 25, 30, 35, 40, and 45% at two minutes.

The images recorded by the camera are processed to extract the profile of the leading edge of the fluid. A front position for the central half of the flow (away from the side walls), measured in pixels and averaged over approximately 125 data

points, is calculated and later converted into a physical distance. The average front position (cm) is plotted against the rescaled time τ (see Section 5.2) to the one-third power in Figure 5.4. After an initial transient, the data is approximately linear with slope (found using least squares) analogous to the scaling constant C of (5.11), which decreases with increasing particle concentration. This qualitatively confirms the well-mixed model. A quantitative comparison of the theoretical, experimental, and numerical scaling constants is given in Figure 5.9. Note also that the data for the different particle concentrations almost collapse.

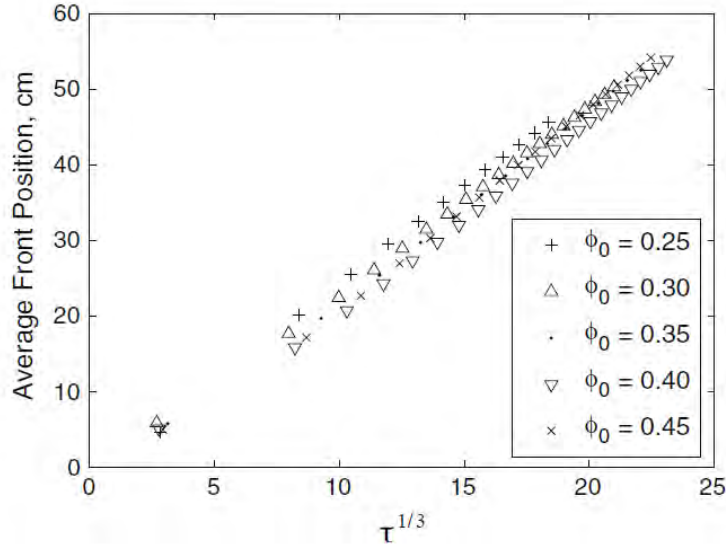


Figure 5.4: Experimental results tracking the average front position and plotting it against the rescaled time $\tau^{1/3}$.

5.4 Numerical Simulations

In this section, we describe numerical simulations for the model of a particle-laden film with settling, i.e., (5.7) and (5.8). This model requires a precursor as

it has been shown that solutions with settling depend singularly on the precursor thickness [CBH08, ZDB05]. The simulations employ an upwind finite-difference scheme, which is efficient for conservation laws with a unidirectional velocity. We use the experimental parameters described in Section 5.3 for the viscosity, density, and the diameter of the particles. For the maximum packing fraction ϕ_{\max} , we use the experimentally determined value of 0.58; see Ward et al. [WWG09]. We assume initial data of the step-like form described in Section 5.2, with initial height $\beta = 2$ and width $L = 2.5$. The precursor height for the numerical data is $b = 0.01$ unless otherwise stated. The initial particle concentration is uniform, representing the well-mixed initial fluid in the physical experiment.

We compute solutions with settling function (5.6) for $m = 1$ and $m = 5$. Recall that the value for the exponent m was determined experimentally [RZ54a]. For each of the settling functions, Figure 5.5 contains snapshots in time of numerical solutions of (5.8). In the left-hand plot which contains solutions using the settling function (5.6) with $m = 1$, the magnitude of the plots in the vertical direction is larger than solutions using the settling function (5.6) with $m = 5$. This phenomenon has been described in Cook et al. [CBH08] as a singular shock. However, at these scales, the plots are qualitatively similar. From the modeling point of view, the exponent $m = 1$ seems to be more appropriate as it shows a stronger ridge that is also observed experimentally. For $m = 5$, the concentrations vary less than 1%. From the data in Figure 5.5, one can determine the spatial variations in the viscosity by the empirically derived model (5.4).

In Figure 5.6, we compare the profile shapes for the analytical solution with precursor (left) and the numerical solution with settling function (right). To compare profile shapes, we rescale the data by the maximum height in h and by front position in x . We see that the addition of particle settling exhibits depar-

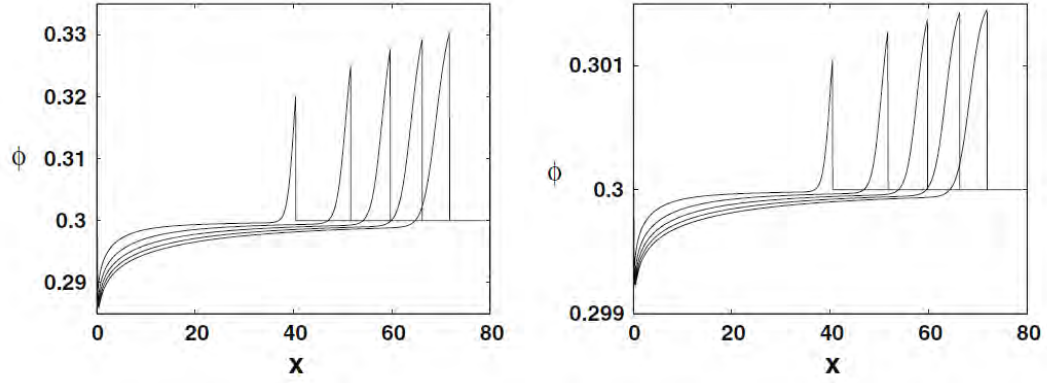


Figure 5.5: Numerical simulations of the particle concentration of solutions of (5.7) and (5.8) with initial concentration $\phi_0 = 0.3$, precursor height 0.01 and for settling function (5.6) with $m = 1$ (left) and $m = 5$ (right) at times $t = 30, 60, 90, 120$. While the plots look qualitatively similar, the more singular solutions for $m = 1$ have larger maxima.

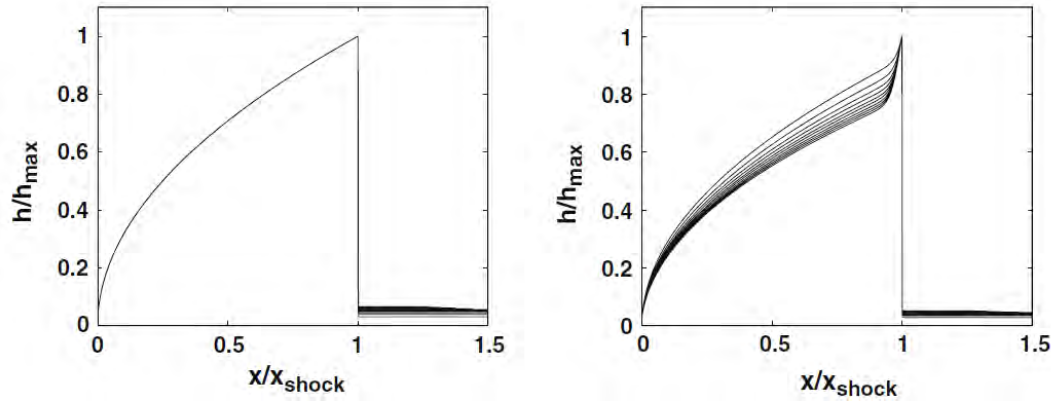


Figure 5.6: A comparison of scaled solutions. On the left, simulations of (5.7)-(5.8) with precursor but no particle settling. On the right, simulations with precursor and settling with $m = 1$. Both simulations have precursor height 0.05 and initial particle concentration $\phi_0 = 0.4$.

tures from pure self-similarity, as seen in the profile shapes, for times relevant to us. Another comparison of the fronts is illustrated in Figure 5.7. It shows that the height of the precursor makes a much more significant difference in the front speed than the addition of particle settling. With a precursor, the front speed is similar for both the analytical solution and the settling models of either power and faster than that of the similarity solution with no precursor.

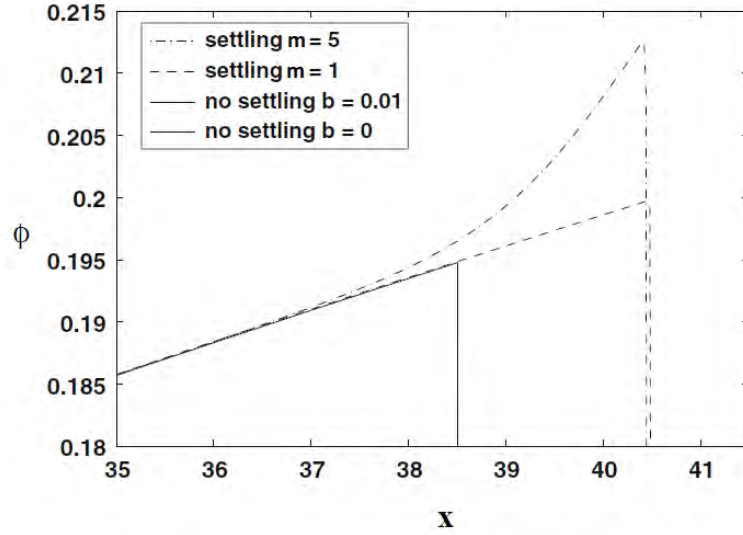


Figure 5.7: Comparison of solutions to the settling model (5.7)-(5.8) with analytical solutions (5.14) of the Riemann problem with precursor height $b = 0.01$ and without precursor for initial particle concentration $\phi_0 = 0.3$, at time $t = 30$.

Figure 5.8 is the numerical version of Figure 5.4, which is for physical experiments. It shows the same near-collapse of the front positions in the right scaling. The data is ordered monotone with the particle concentration. The qualitative agreement of Figures 5.4 and 5.8 is very good, whereas the quantitative agreement is not yet fully reached.

A quantitative comparison between analytical, numerical, and experimental results is provided in Figure 5.9. It shows the scaling constants derived from the

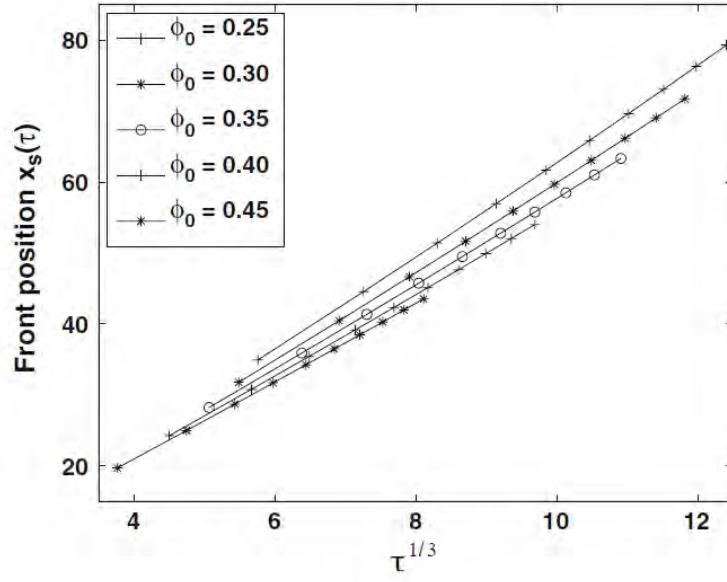


Figure 5.8: The front position $x_s(\tau)$ plotted versus $\tau^{1/3}$ for different particle concentrations. The data is nearly independent of the choice of settling function. It has precursor height $b = 0.01$.

experiments, the numerics, and the theory, all divided by the theoretical constants, in dependence of the particle concentration. The solid line at 1 represents the theoretical constants (5.11) derived from the analytical solutions without precursor. The theoretical constants with precursor height $b = 0.01$ derived in Section 5.2 are bigger than the ones for $b = 0$. They are similar to the numerical data for precursor height $b = 0.01$. The numerical values for C for the different settling functions are so similar that the points are virtually indistinguishable on this plot and are represented by a single averaged point. The numerical data is the same as in Figure 5.8. The numerical (experimental) constants are found by the slope of a linear interpolation of the data in Figure 5.8 (Figure 5.4). The best agreement between the numerical results from the system (5.7) and (5.8) and the experimental results is for an initial particle concentration of approximately 0.45.

We conjecture that this is a balancing point between low particle concentrations when settling to the substrate is dominant and high particle concentrations when clumping and sliding behavior dominates. We see that numerics as well as theory overestimate the scaling constant found in the physical experiment for low concentrations. For high concentrations, the numerical and the experimental scaling constants almost agree.

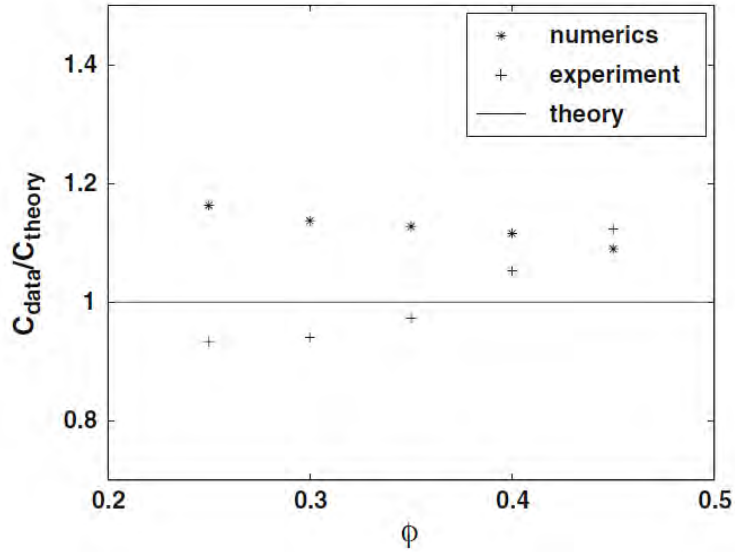


Figure 5.9: Dependence of the scaling constant C on the particle concentration ϕ . The theoretical scaling constant is computed from (5.11). The numerical and experimental data come from Figures 5.8 and 5.4.

5.5 Summary

We have developed a new understanding of the role of the precursor in lubrication models for particle-laden thin film flows, in determining the position of the front of a particle-laden fluid. Settling of the particles in the direction of the flow primarily affects the profile of the film as a particle-rich ridge develops at the

front, and has a less significant effect on the speed of the front. The scaling for the front position that is exact for analytical solutions with and without precursor is also appropriate to leading order for numerical simulations of the model with particle settling, as well as for the physical experiments.

The development of a particle-rich ridge at the front of the fluid is seen in the numerical data and in the physical experiments, where it appears as a dark ridge at the front. However, it is also clear that the model does not quantitatively reproduce this departure from self-similarity of the fluid profile. A separate paper, on the transverse fingering instability with surface tension [CAB09] also suggests that some important physics is missing from the lubrication model, even when surface-tension effects are included in the mathematics. One possibility of additional physics to include in this analysis is shear-induced migration (e.g., [LA86, LA87b]) which has recently been shown to give quantitatively accurate predictions of phase transitions between settling to the substrate and settling to the contact line in constant-flux experiments [Coo08]. It would also be interesting to incorporate a precursor into the physical experiments.

The understanding of particle-laden fluid flows and the relationship to clear fluid and pure granular models is still at a preliminary stage. Appropriate modeling for low concentrations, in which settling to the substrate creates a phase transition in which part of the fluid becomes particle-free needs more modeling. The high particle concentrations that exhibit sliding of large clumps will require yet another (if fluid, then non-Newtonian) model.

CHAPTER 6

Experiments Compared with Equilibrium Theory

6.1 Background

While many studies address gravity-driven clear liquid flows [Hup82, SD85, THS89, JB92, KB99, Kon03b] and pure granular flows [NHS89, SH89, PDS97], comparatively fewer studies have centered on particle-laden thin film flows [ZDB05, CBH08, Co008, WWG09]. Apart from complexities associated with moving contact lines, the study of slurries also involves an intricate interplay between particle settling/migration and viscous fingering mechanisms.

The settling of particles in quiescent liquids and sedimentation in suspensions have also garnered significant attention [RZ54b, Bat72, BM73, BGO82, DA85, SM00]. For rigid spherical particles, the well-known Stokes' Law applies, neglecting inertial effects of the liquid due to the smallness of the Reynolds number. In order to account for the presence of a large number of identical particles, the velocity given by Stokes' Law is typically modified by a purely empirical multiplicative hindrance function which depends on the particle concentration, ϕ . This function, typically denoted by $f(\phi)$, has been a matter of much discussion through the decades. A so-called Richardson-Zaki expression was proposed, where $f(\phi) = (1-\phi)^m$, with $m \approx 5.1$, and found to compare favorably with exper-

imental data for moderately dilute suspensions [RZ54b]. For dilute dispersions, $f(\phi) \sim (1 - 6.55\phi)$ was suggested in Batchelor [Bat72]. Other, more complex, expressions for $f(\phi)$ have been discussed [BM73, BGO82, DA85, SM00]. In the presence of shear, a hindrance function of form $f(\phi) \sim (1 - \phi)$ was shown to be appropriate in Schaffinger et al. [SAZ90].

Concentrated suspensions of spherical particles have been shown to behave curiously when subjected to shear. This phenomena was first detected in experiments with a Couette viscometer, where an unusual decrease in measured viscosity occurred during prolonged shearing. The theoretical framework for this phenomena was laid out by Leighton and Acrivos [LA87a, LA87b] and subsequently rephrased in Phillips et al. [PAB92]. Its key element was *shear-induced migration*, a diffusive mechanism resulting from gradients in both the particle concentration and suspension viscosity, $\mu(\phi)$. Net fluxes caused by these gradients were deduced by considering irreversible interactions between pairs of smooth spherical particles (for details, see [LA87b]). In Phillips et al. [PAB92], the predictions of this model were shown to be in excellent agreement with experimental data for Couette flows, and the use of the model was also extended to flows of concentrated suspensions through cylindrical tubes. Recently, the model was employed in Kim [CLK08] to carry out numerical simulations for suspension flows in more complex geometries. Other studies, focusing on the migration of particles in pressure-driven channel flows [NB94], steady and unsteady flows in various geometries [MB99], and inclined free-surface channel flows [TM05], were carried out using a different approach, based on Stokesian dynamics.

More recent studies addressed particle-laden thin film flows with contact lines. Zhou et al. [ZDB05] reported on their preliminary experimental results for incline flows of suspensions of polydisperse glass beads with diameter $\sim O(100\mu\text{m})$,

focusing on a single bead size. As they varied the bulk particle concentration, ϕ_0 , and the inclination angle, α , they identified three distinct settling regimes: for small ϕ_0 and α values, the particles would settle out of the flow, clear liquid film would flow over the particulate bed, and the fingering instability resulted; for large values of ϕ_0 and α , the particles would move faster than the liquid, leading to an aggregation of particles in the contact line region, the formation of a particle-rich ridge, and almost complete suppression of the fingering instability; finally, intermediate values of these parameters would lead to a well-mixed regime in which a fingering instability occurred. A theoretical model was also derived in Zhou et al. [ZDB05], based on the Navier-Stokes equations for the liquid and a diffusive model for the particle concentration, including capillary effects and hindered settling. A simplified version of this model, which neglected higher-order capillary terms was studied in a shock dynamics framework [ZDB05, CBH08]. Although successful in explaining qualitatively the formation of the particle-rich ridge, they did not provide a quantitative model nor did they ever attempt to model the other regimes. In an effort to improve the understanding of these regimes, Cook [Coo08] included shear-induced migration in his model. He assumed that the outcome of particle settling is guided by the balance between shear-induced migration and hindered settling. Through his steady state formulation, he derived a system of ODEs for ϕ and the shear stress, σ . However, this model did not include a significant hindrance effect due to the presence of the solid track. Furthermore, while he found good agreement between the model's predictions regarding the well-mixed regime and the experimental data, the data itself was from Zhou et al. [ZDB05] - old, preliminary, and rather limited. Additional work in Ward et al. [WWG09] focused on studying the propagation of contact lines in particle-laden thin film flows experimentally. Apart from varying ϕ_0 and α , particle size and density, and liquid viscosity were all varied in order

to examine their influence on the front speed. It was found that the dependence of the front position on time was of a power-law type, with exponents similar to the one-third proposed in Huppert [Hup82].

In this chapter, we carry out a systematic study of the settling regimes over a range of particle sizes and liquid viscosities. Through comparison between our experimental results and the predictions of equilibrium theory, we uncover the transient nature of the well-mixed regime, where a bifurcation to either of the remaining regimes eventually occurs. In addition, our experimental results clearly indicate how the particle size and the liquid viscosity affect the time scale on which we observe this transient regime.

In contrast to the preliminary experimental results from Zhou et al. [ZDB05], we perform experiments with three different particle sizes and two different liquid types, and vary ϕ_0 and α over wide ranges of values. The liquid viscosity and the particle size are found to affect the width of the region in (ϕ_0, α) -space over which the transition between the settled and ridged regimes occurs. Therefore, we show that these parameters dictate both the likelihood of observing the well-mixed regime for given ϕ_0 and α values, and the time scale over which the well-mixed suspension is preserved. Next, a theoretical model is derived. We consider the steady state of the system where hindered settling balances the shear-induced migration of particles. Our modeling approach is similar to the one in Cook [Coo08], with one important difference: we also include the hinderance to settling due to the presence of the solid track. We proceed by showing excellent agreement between the model's predictions and our experimental results over all ranges of viscosities and particle sizes. Furthermore, we show how the results of numerical simulations of our model provide additional evidence for the transiency of the well-mixed regime.

6.2 Experimental Apparatus and Techniques

Figure 6.1 shows the experimental apparatus we use, which is the same as in Section 5.3. A liquid/particle mixture prepared beforehand is poured into the reservoir situated at the top of the track and the gate is lifted, allowing it to flow down the track, with the contact line initially straight. Here, we only focus on experiments with finite, constant suspension volume. The evolution of the flow is monitored using a digital camera, which is positioned above the track and captures images of the moving front at predetermined time intervals, typically 0.25-4 seconds. Using this setup, we are able to monitor the film motion, starting from release, until the front has reached approximately 0.6 m down the track. Several fluorescent lights are placed below the track for imaging purposes, while food-coloring dye is employed to enhance contrast. Images are subsequently analyzed, and each experimental run is classified, based on the observed settling regime, as either ‘settled’, ‘well-mixed’ or ‘ridged’ (see Section 6.3 for details).

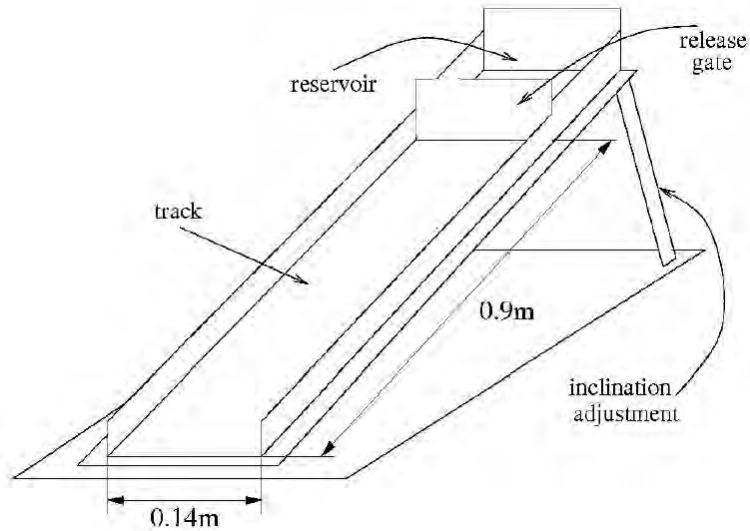


Figure 6.1: The experimental apparatus.

Our experiments involve three different particle types and two different liquids. The particles are smooth spherical glass beads (Ceroglass), and we consider three different diameters: $d = 0.143$ mm (‘P1’), 0.337 mm (‘P2’), and 0.625 mm (‘P3’). The standard deviation of the particle diameters is 26% for all particle sizes. For the suspending liquid, we use polydimethylsiloxane (PDMS) (Alfa Aesar) in two different kinematic viscosities: $\nu = 10^{-4}$ m²/s (‘L1’) and 10^{-3} m²/s (‘L2’). The particles are heavy, i.e., $\rho_p > \rho_l$ for all particle and liquid types, where ρ_p and ρ_l are particle and liquid densities respectively. Relevant material parameters are summarized in Table 6.1.

Suspensions are prepared by first weighing the particles and PDMS individually, pouring PDMS into a container, and then adding particles; slow manual stirring is used until a uniform mixture is obtained. This procedure prevents the formation of air bubbles. Typically, no haste is required between the preparation of the suspension and its release down the track since uniformity of the mixture is preserved for sufficiently long time-intervals. The bulk particle concentration, ϕ_0 , is defined as $\phi_0 = V_p/V$, where $V = V_l + V_p$ is the total volume of the mixture, and V_l and V_p are the liquid and particle volumes respectively. Here, we focus on V between 75 ml and 103 ml.

	$\nu(\text{m}^2/\text{s})$	$\rho_l(\text{kg}/\text{m}^3)$	$\rho_p(\text{kg}/\text{m}^3)$	$d(\text{mm})$
L1	10^{-4}	966	-	-
L2	10^{-3}	971	-	-
P1	-	-	2475	0.143
P2	-	-	2475	0.337
P3	-	-	2475	0.625

Table 6.1: Physical properties of the liquids and particles used in the experiments.

The experiments are carried out in open air and at room temperature (298 K), maintained by the air-conditioning unit. The fluorescent lights we use for imaging purposes radiate heat, but the amount is insufficient to affect either the viscosity of the liquid, flow dynamics, or observed particle behavior in any significant manner. The track, gate, and reservoir are cleaned after each experimental run using a squeegee to remove the excess particulate and dust which may accumulate. Although this cleaning procedure does not remove the PDMS entirely, it ensures reproducibility of our experimental results.

	P1	P2	P3
L1	Experiment C	Experiments A,C	-
L2	Experiment B	Experiments A,B	Experiment B

Table 6.2: The different liquid/particle combinations we consider. We study the manner in which the viscosity of the suspending liquid (Experiment A) or particle size (Experiments B and C) affects the settling regime.

We carry out three different sets of experiments, conveniently summarized in Table 6.2. In all experiments, we vary ϕ_0 between 0.25 and 0.50, and α between 20° and 50° . In Experiment A, we consider medium-sized particles, P2, and both PDMS types in order to study the influence of the viscosity of the suspending liquid on the settling regime. Experiments B and C focus on studying the influence of particle size, by fixing the liquid type (L2 in B and L1 in C) and varying the particle size. When L1 PDMS and P3 particles are used, rapid settling occurs. Regardless of our best efforts, a significant fraction of particles often settles to the bottom of the reservoir before the suspension is ever released down the track. Hence, we omit experiments with this mixture.

6.3 Experimental Results

In all experiments, the observed flows are relatively slow. In addition, settling behavior can only be classified after an initial transient stage which typically lasts up to 900 seconds. The settling regimes observed in our experiments resemble the ones discussed in Zhou et al. [ZDB05]: each experimental run is labeled as either settled, well-mixed, or ridged. Typical examples of these regimes are shown in Figure 6.2. In general, these three regimes occur in each experimental set, A, B, and C (an exception is discussed below). In the settled regime, the particles tend to quickly settle out of the flow, forming a particulate bed, with the suspending liquid moving down the track faster than the particles. Virtually clear liquid film ultimately leaves the particulate bed far behind and develops the fingering instability as described in Huppert [Hup82]. Typically, this regime occurs for small values of ϕ_0 and α . In contrast, when ϕ_0 and α are large, the particles move faster than the suspending liquid and aggregate in the contact line region, forming a particle-rich ridge, often several times thicker than the trailing film. Hence, we refer to this regime as ridged. Large particle concentrations at the front appear to suppress the fingering instability. Intermediate values of ϕ_0 and α lead to the well-mixed regime, where the particle concentration remains almost uniform throughout the film. The fingering instability occurs, but compared to the settled regime, it is typically characterized by a longer wavelength.

For any particular liquid/particle combination, we classify each experimental run and compile the results of the classification in a corresponding (ϕ_0, α) phase diagram (see Figures 6.3, 6.4, and 6.5). Same-type settling behaviors cluster in these diagrams, forming distinct bands. We use color to label these regime bands: *white* for settled, *light* for well-mixed, and *dark* for ridged. Figures 6.3, 6.4, and 6.5 each include a curve superposed on the experimental results. These curves

represent a well-mixed regime prediction (i.e. $\phi' = 0$, where $\phi(z)$ is particle concentration) of our theoretical model. The discussion regarding the model and the agreement between its predictions and the experimental results is given in Sections 6.4 and 6.5.

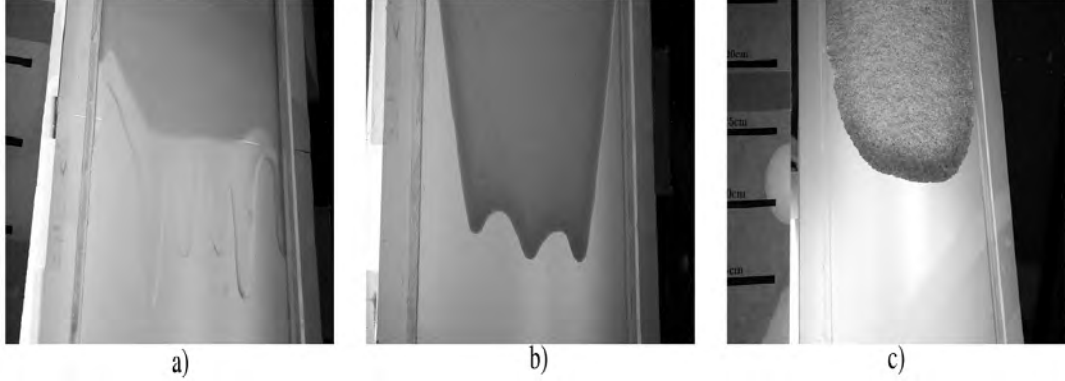


Figure 6.2: The settling regimes: a) settled, b) well-mixed, and c) ridged. The fingering instability typical of clear liquid flows is only observed in the settled and well-mixed regimes.

We note that other more complex behavior also occurs. In some experimental runs, we notice capillary motion of the particles along the side walls or their alignment in linear streaks along the track. Irregularities in the shape and size of fingers, and extreme cases of the ridged regime, where sections of the contact line experience jamming with particles, become solid-like and virtually break off in blocks are also observed. These phenomena are attributed to either the finite width of the track and the presence of side walls or complex interplay between particle migration and contact line effects. While very intriguing, we leave detailed study of such complex behavior for future work, and focus here on the three settling regimes described above. We proceed by discussing the dependence of settling behavior on the viscosity of the suspending liquid and the particle size by presenting results of Experiments A, B, and C.

In Experiment A, we consider intermediate size particles, P2, and both the low and the high viscosity liquid (L1 and L2 respectively). This allows us to study the dependence of observed settling behavior on PDMS viscosity. Since, based on Stokes' Law (e.g., [Bat72]), the settling velocity of particles is inversely proportional to the liquid viscosity, a decrease in PDMS viscosity should result in an enhanced tendency of the particles to settle out of the flow. Figure 6.3 shows phase diagrams which result for low a) and high viscosity b). At first glance, the outcomes appear to be rather similar for the two liquids, although the band for the settled regime is somewhat wider in Figure 6.3 a) compared to b), confirming our expectations based on the settling time. A closer inspection also reveals that the well-mixed band is noticeably wider when the viscosity of the suspending liquid is lower (Figure 6.3 a)). In order to better understand this difference, we consider the time scales of the motion of the front and the settling of the particles. For clear fluid inclined flows, the former time scale is proportional to the viscosity of the liquid (e.g., [ZDB05]), $T \propto \mu$. However, for suspensions $\mu = \mu(\phi)$. For estimation purposes, we may assume uniformity of the slurry (i.e., well-mixed case), and by using $\mu = \rho_l \nu (1 - \phi/\phi_{\max})^{-2}$ as in [TM05], we get that $T \propto \nu$. It is now clear that a decrease in the viscosity of the suspending liquid, with all the other material parameters fixed, leads to a faster propagation of the suspension front. On the other hand, for purely gravity-driven particle settling, the relevant time scale is viscous and also directly proportional to ν (see Section 6.4) - a decrease in viscosity leads to a faster settling of particles. Therefore, if gravity were the only mechanism responsible for particle settling, the width of the well-mixed bands in Figure 6.3 would have been independent of the viscosity. The fact it is not suggests that some part of the relevant settling dynamics occurs on a time scale other than the viscous one. In Section 6.4, we conjecture that the settling behavior is governed by a balance between settling

due to gravity and shear-induced migration. This balance may lead to settling which occurs on a different time scale, introducing a correction to the purely viscous one. Accordingly, while a decrease in the viscosity clearly affects the motion of the front, it may only have a relatively minor effect on the settling rate.

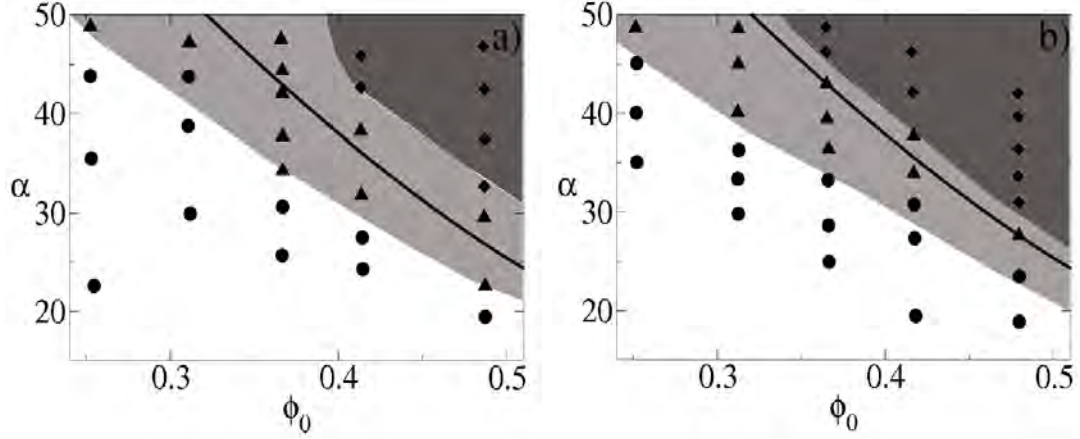


Figure 6.3: Phase diagrams for Experiment A. Particle type is fixed (P2), viscosity of the suspending liquid is varied: a) low (L1); and b) high (L2). The symbols denote the regimes observed in experimental runs: circles (\bullet) for settled, triangles (\blacktriangle) for well-mixed, and diamonds (\blacklozenge) for ridged. The solid curve represents the prediction of our theoretical model (see Sections 6.4 and 6.5) for a regime where $\phi' = 0$ (well-mixed).

Next, we examine the manner in which particle size affects the settling regime. For this purpose, we carry out Experiments B and C, where the liquid type is fixed and the particle size is varied.

In Experiment B, we consider the high viscosity suspending liquid, L2, and all three particle sizes, P1, P2, and P3 (note: experimental runs with the L2/P2 combination have already been carried out in Experiment A). According to Stokes' Law, the settling velocity is proportional to a^2 , and hence, the largest particles

are most likely to settle out of the flow. Based on this reasoning, the settled band should be widest for P3. The phase diagrams resulting from Experiment B are shown in Figure 6.4.

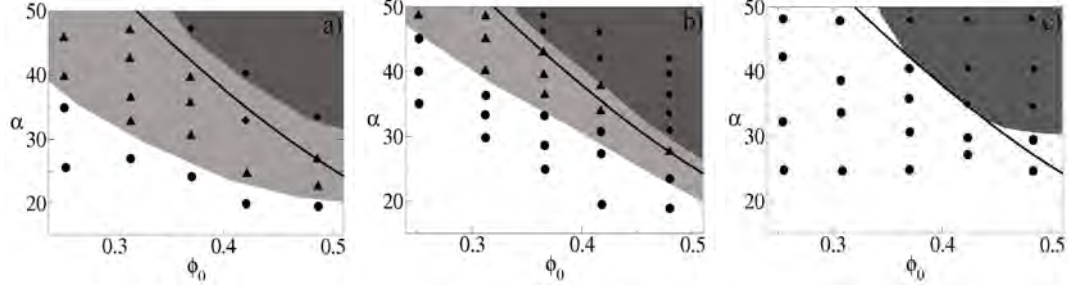


Figure 6.4: Phase diagrams for Experiment B. Viscosity of the suspending liquid is fixed (high viscosity, L2), particle size is varied: a) small (P1); b) intermediate (P2); and c) large (P3). The symbols denote the regimes observed in experimental runs: circles (\bullet) for settled, triangles (\blacktriangle) for well-mixed, and diamonds (\blacklozenge) for ridged. The solid curve represents the prediction of our theoretical model (see Sections 6.4 and 6.5) for a regime where $\phi' = 0$ (well-mixed).

Compared to Experiment A, the differences between the diagrams are much more pronounced. The speculation based on Stokes' Law is again proven correct compared to Figures 6.4 a) and b), the band corresponding to the settled regime is widest in Figure 6.4 c); it is narrowest for the smallest particles in Figure 6.4 a). But, the most striking feature here is a complete absence of the well-mixed regime for the largest particles in Figure 6.4 c) - all considered runs with the L2/P3 configuration resulted in either settled or ridged behavior. In addition, we notice that the well-mixed band is significantly wider for the smallest particles in Figure 6.4 a) compared to the intermediate ones in Figure 6.4 b). Hence, the trend is obvious: for a fixed liquid viscosity, an increase in particle size makes the well-mixed outcome less likely. This result further supports our hypothesis re-

garding the transient nature of the well-mixed regime. In particular, the diffusive fluxes of particles due to hindered settling and shear-induced migration are both proportional to a^2 (see Section 6.4). Since these are, in our opinion, the two main mechanisms of particle motion in the system we study, the smallest particles P1 are moving on a time scale much longer than the larger particles P2 and P3. Consequently, and as seen in Figure 6.4 a), many runs involving P1 remain well-mixed for the duration of the experiment. We suspect that given a longer track and larger sample volume, the majority of these flows would eventually bifurcate to either the settled or ridged regime. On the other hand, the largest particles P3 move on shorter time scale compared to both P1 and P2. Therefore, the flows involving particles P3 quickly bifurcate to either settled or ridged, with the latter regime likely for most ϕ_0 and α values. The complete absence of the well-mixed band in Figure 6.4 c) serves as an indicator of just how rapid this process is.

Finally, in Experiment C, we study the influence of particle size on the settling behavior for low viscosity PDMS, L1. We focus on small and intermediate size particles, P1 and P2. As discussed in Section 6.2, we do not consider the L1/P3 combination since the particles in all suspensions of that type undergo rapid settling while still in the reservoir. We also note that runs with the L1/P2 combination have already been carried out in Experiment A.

The results of Experiment C are shown in Figure 6.5. The trend observed in Experiment B is very much noticeable here too: as the particle size increases, the uniformity of the suspension is less likely to be preserved. In particular, the well-mixed band is significantly wider in Figure 6.5 a) compared to the one in b) for larger particles. The explanation for this trend is identical to one for Experiment B. For small particles, the time scale of particle settling is much longer than for larger ones; therefore, uniformity of the suspension is likely to

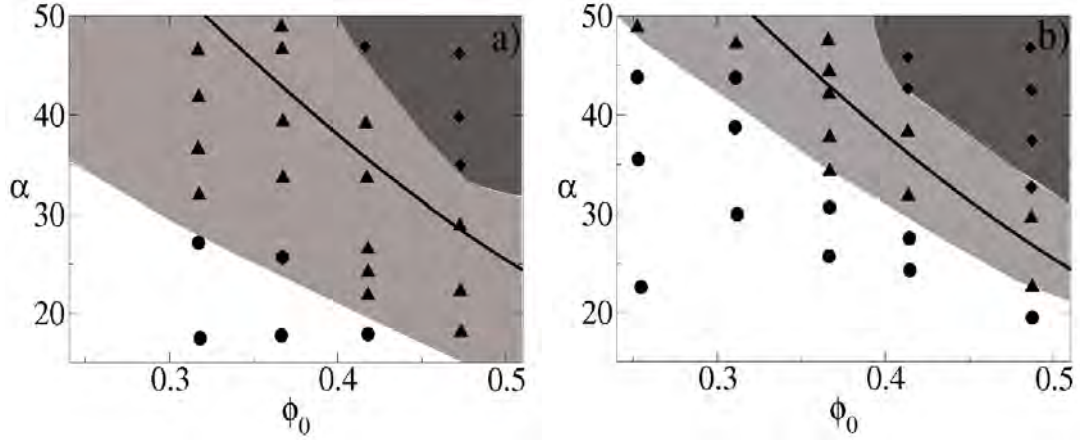


Figure 6.5: Phase diagrams for Experiment C. Viscosity of the suspending liquid is fixed (low viscosity, L1), particle size is varied: a) small (P1) and b) intermediate (P2). The symbols denote the regimes observed in experimental runs: circles (\bullet) for settled, triangles (\blacktriangle) for well-mixed, and diamonds (\blacklozenge) for ridged. The solid curve represents the prediction of our theoretical model (see Sections 6.4 and 6.5) for a regime where $\phi' = 0$ (well-mixed).

be preserved longer for small particles. Furthermore, a comparison of diagrams in Figures 6.3, 6.4, and 6.5 reveals that the well-mixed regime is more likely to occur for L1/P1 than for any other liquid/particle combination we consider - the well-mixed band in Figure 6.5 a) is by far the widest. This is particularly evident when Figures 6.4 a) and 6.5 a) are compared (small particle size, high and low viscosity suspending liquid respectively). The latter comparison also shows that for the smallest particles, the influence of viscosity on both prolonging the transient phase and making it more likely for a wider range of ϕ_0 and α values is much more pronounced than in Experiment A.

To summarize, Experiments A, B, and C show that the particle size particularly affects settling behavior. It dictates the likelihood of occurrence for the settled regime and the time scale for particle-motion in general. The viscosity

of the suspending liquid also influences the particles' motion, and increasingly so for smaller particles. The experiments also reveal the transient nature of the well-mixed regime. This is evident from the manner in which both the particle size and the viscosity of the suspending liquid affect the persistence of the well-mixed regime. We argue that given a longer track length, a majority of, if not all, the well-mixed flows would bifurcate to either the settled or ridged regime. We revisit this argument again when we compare the predictions of our theoretical model and the experimental results in Section 6.5.

6.4 Theoretical Model

We consider a continuum model for the particle concentration, ϕ . The dynamics of ϕ are described by a conservation equation for particles, written in an Eulerian reference frame

$$\frac{D\phi}{Dt} = -\nabla \cdot (\mathbf{J}_{\text{bd}} + \mathbf{J}_{\text{grav}} + \mathbf{J}_{\text{coll}} + \mathbf{J}_{\text{visc}}). \quad (6.1)$$

Here t denotes time, and $D/Dt = \partial/\partial t + \mathbf{v} \cdot \nabla$, where $\mathbf{v} = (u, w)$, u and w are the components of the liquid velocity vector \mathbf{v} in the x -direction (down the track) and z -direction (normal to track) respectively. Equation (6.1) includes hindered settling (\mathbf{J}_{grav}), and shear-induced migration effects (\mathbf{J}_{coll} and \mathbf{J}_{visc}). It also includes Brownian diffusive flux, $\mathbf{J}_{\text{bd}} = -D\nabla\phi$. We note that since the Péclet number corresponding to our problem is large (i.e., $Pe = \dot{\gamma}a^2/D \sim O(10^3)$, where $\dot{\gamma}$ is the magnitude of the local shear rate), we neglect this effect. The viscosity of the suspension is a function of the particle concentration, $\mu = \mu(\phi)$. Here, we use the expression from [TM05], $\mu(\phi) = \mu(1 - \phi/\phi_{\text{max}})^{-2}$, where ϕ_{max} denotes the maximum packing fraction, and restricts the meaningful interval of values for ϕ

to $[0, \phi_{\max}]$, with the mixture becoming almost solid-like as $\phi \rightarrow \phi_{\max}$. Different values of ϕ_{\max} have appeared in the literature, usually within the range 0.57-0.68 (e.g., see [Coo08, WWG09, BGO82, SM00, LA87b, SAZ90, PAB92, MB99, TM05]). We use the procedure described in [WWG09] and obtain $\phi_{\max} = 0.61$. Also, $\mu_l = \nu \rho_l$.

The settling of a particle due to gravity is hindered by the presence of other particles and the solid track/wall [ZDB05]. The net flux of particles caused by this effect is given by

$$\mathbf{J}_{\text{grav}} = -\frac{2a^2\phi(\rho_p - \rho_l)}{9\mu_l} f(\phi)w(z)\mathbf{g}. \quad (6.2)$$

Here, we use the hindrance function from Schaflinger et al. [SAZ90]: $f(\phi) = \mu_l(1 - \phi)/\mu(\phi)$. The presence of a solid track at $z = 0$ is taken into account through $w(z) = A(z/a)^2/\sqrt{1 + A^2(z/a)^4}$ [ZDB05]; $A = 1/18$ so that $w(z) \rightarrow 0$ as $z \rightarrow 0$, and $w \approx 1$ away from $z = 0$. We note that this is the main difference between our model and the one derived in [Coo08]: we include the hindrance $w(z)$ in our settling model, while in Cook [Coo08], this effect is neglected altogether.

The effect of shear-induced migration is included in Equation (6.1) through two separate terms, \mathbf{J}_{coll} and \mathbf{J}_{visc} . These terms are defined as in Leighton and Acrivos [LA87b] and Phillips et al. [PAB92]. The net flux of particles due to irreversibility of collisions between pairs of particles is given by

$$\mathbf{J}_{\text{coll}} = -K_{\text{coll}}a^2(\phi^2\nabla\dot{\gamma} + \phi\dot{\gamma}\nabla\phi). \quad (6.3)$$

On the other hand, the net flux due to gradients in viscosity, $\mu(\phi)$, is given as

$$\mathbf{J}_{\text{visc}} = -K_{\text{visc}}a^2\phi^2\dot{\gamma}\frac{1}{\mu(\phi)}\frac{d\mu}{d\phi}\nabla\phi. \quad (6.4)$$

Here, K_{coll} and K_{visc} are proportionality constants determined from experiments. We follow Phillips et al. [PAB92] and use $K_{\text{coll}} = 0.41$ and $K_{\text{visc}} = 0.62$.

The fluxes given in Equations (6.2), (6.3), and (6.4) are all proportional to a^2 , a fact we have employed in Section 6.3, in our argument regarding the influence of particle size on the settling behavior of particles. It is interesting to note that in Equation (6.3), the first term suggests that even if the particle distribution is uniform (i.e., $\nabla\phi = 0$), migration will occur due to gradients in the frequency of irreversible particle collisions. This migration will then induce gradients in ϕ and hence, the second term in Equation (6.3) is activated.

The governing equation given in (6.1) is accompanied by boundary conditions (zero normal flux at both $z = 0$ and $z = h$, where h is film thickness) and coupled to the Navier-Stokes equations for a liquid with viscosity $\mu(\phi)$. However, in order to gain insight into the settling behavior of particles, it is sufficient to consider Equation (6.1) at steady state [Coo08]. Assuming the thin film is flat, the steady state is achieved when the fluxes given in Equations (6.2), (6.3), and (6.4) balance in z -direction

$$\mathbf{J}_{\text{grav}} + \mathbf{J}_{\text{coll}} + \mathbf{J}_{\text{visc}} = 0. \quad (6.5)$$

We also assume that the flow is simple and unidirectional, so that $\dot{\gamma} = \partial u / \partial z$. Henceforth, instead of using $\dot{\gamma}$, we revert to the shear stress, $\sigma = \mu(\phi)\dot{\gamma}$. By scaling Equation (6.5) using H as the length scale in z -direction and $\rho_l g H \sin \alpha$ as the scale for σ , and differentiating, we arrive at the following ODE

$$\left[1 + \frac{2(K_{\text{visc}} - K_{\text{coll}})}{K_{\text{coll}}} \frac{\phi}{\phi_{\text{max}} - \phi} \right] \sigma \phi' = -\sigma' \phi - \frac{2\rho_f \cot \alpha}{9K_{\text{coll}}} (1 - \phi) \bar{w}(z), \quad (6.6)$$

where $\rho_f = (\rho_p - \rho_l) / \rho_l$, and $\bar{w}(z)$ is the scaled version of $w(z)$. Since we assume

that the film is flat, the pressure is hydrostatic in the suspension and the (scaled) gradient in shear stress is given as [Coo08]

$$\sigma' = -(1 + \rho_f \phi). \quad (6.7)$$

By substituting the expression from Equation (6.7) into (6.6), we obtain

$$\left[1 + \frac{2(K_{\text{visc}} - K_{\text{coll}})}{K_{\text{coll}}} \frac{\phi}{\phi_{\text{max}} - \phi} \right] \sigma \phi' = (1 + \rho_f \phi) \phi - \frac{2\rho_f \cot \alpha}{9K_{\text{coll}}} (1 - \phi) \bar{w}(z). \quad (6.8)$$

Finally, the accompanying boundary conditions are $\sigma(0) = (1 + \rho_f \phi_0)$ and $\sigma(1) = 0$ [Coo08].

The system of ODEs given by Equations (6.7)-(6.8) and accompanying boundary conditions may be solved numerically for $\phi(z)$ and $\sigma(z)$. The numerical solutions of this system are discussed in Section 6.5.

6.5 Predictions of Theoretical Model vs. Experimental Results

The system of equations for $\phi(z)$ and $\sigma(z)$ given by (6.7)-(6.8) is solved using a shooting method. The shooting is carried out from $z = 0$, with $\phi(0)$ adjusted in order to satisfy $\sigma(1) = 0$. Since $\partial u / \partial z = \sigma(z) / \mu(\phi(z))$, once $\phi(z)$ and $\mu(z)$ are known, $u(z)$ is readily found, by simply integrating once and using the no-slip boundary condition, $u(0) = 0$.

As previously noted in Cook [Coo08], due to the fact that σ is nonnegative, ϕ is a monotonic function of z . This is because $\sigma \phi'$ in Equation (6.8) is determined by a function of ϕ only, with a single unstable root $\bar{\phi}(\alpha)$ in the interval $[0, \phi_{\text{max}}]$. Hence, either $\phi_{\text{max}} > \phi(0) > \phi_0$ and $\phi(1) = 0$, or $\phi(0) < \phi_0$ and $\phi(1) = \phi_{\text{max}}$,

corresponding to the experimentally observed settled and ridged regimes respectively. The well-mixed regime occurs when $\phi' = 0$ and $\phi(z) = \phi_0$ for $0 < z < 1$. Setting $\phi' = 0$, $\phi = \phi_0$ in Equation (6.8) allows us to obtain an expression for α in terms of ϕ_0

$$\alpha = \tan^{-1} \left[\frac{2\rho_f}{9K_{\text{coll}}} \frac{1 - \phi_0}{(1 + \rho_f\phi_0)\phi_0} \right]. \quad (6.9)$$

The curve corresponding to this expression is shown as a solid line compared with the experimental results in the phase diagrams of Figures 6.3, 6.4, and 6.5. The profiles for $\phi(z)$ and $u(z)$ obtained by numerically solving Equations (6.7)-(6.8) using several representative combinations of ϕ_0 and α values are shown in Figures 6.6, 6.7, and 6.8.

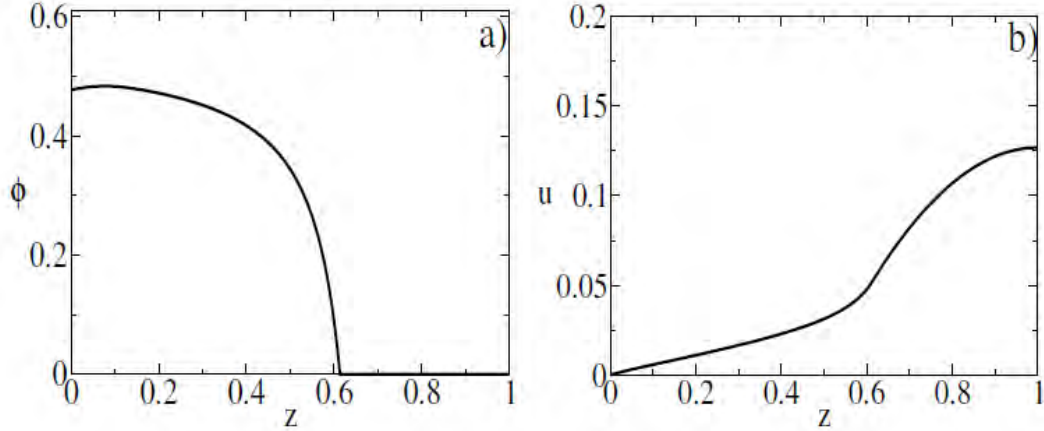


Figure 6.6: Numerical solution for $\phi_0 = 0.250$ and $\alpha = 15^\circ$: (a) particle concentration, $\phi(z)$; and (b) velocity, $u(z)$. Note that $\phi_{\text{max}} > \phi(0) > \phi_0$ and $\phi(1) = 0$. This corresponds to the *settled* regime.

Figure 6.6 shows the profiles for $(\phi_0, \alpha) = (0.250, 15^\circ)$, corresponding to the settled regime in all phase diagrams in Figures 6.3, 6.4, and 6.5. From Figure 6.6 a), it is evident this is the scenario where $\phi_{\text{max}} > \phi(0) > \phi_0$ and

$\phi(1) = 0$. Most of the particles are in $z \leq 0.5$, after which ϕ decreases rapidly. Effectively, the particle-rich lower layer is covered by a less viscous clear liquid layer. Furthermore, in Figure 6.6 b), the velocity increases sharply for $z > 0.5$, causing the clear liquid layer to flow faster than the particle-rich one. This is equivalent to the regime seen in Figure 6.2 a) in which particles settle to the substrate and clear liquid continues down the track. In this case, the prediction of our model agrees well with the experimental results.

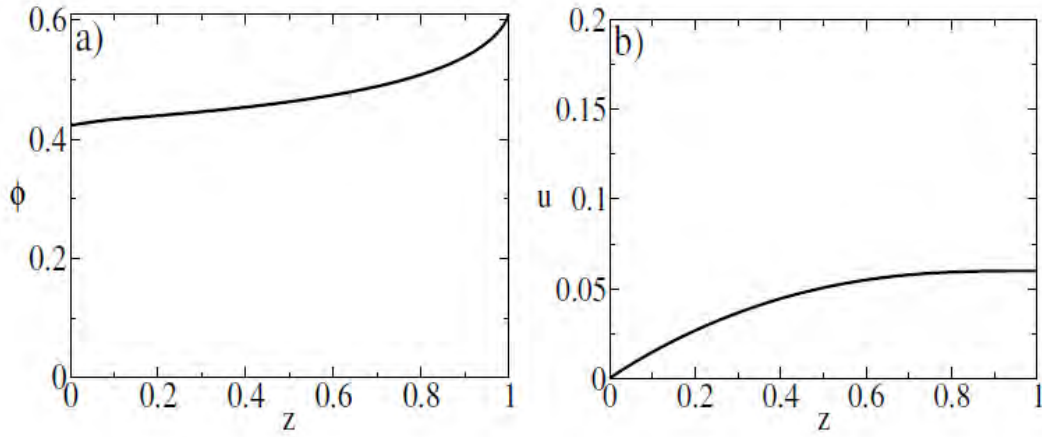


Figure 6.7: Numerical solution for $\phi_0 = 0.475$ and $\alpha = 45^\circ$: (a) particle concentration, $\phi(z)$; and (b) velocity, $u(z)$. Note that $\phi(0) < \phi_0$ and $\phi(1) = \phi_{\max}$. This corresponds to the *ridged* regime.

In Figure 6.7, the profiles for ϕ and u resulting from $(\phi_0, \alpha) = (0.475; 45^\circ)$ are given. We note that in all our experiments with these values of ϕ_0 and α , the ridged regime occurs (see Figures 6.3, 6.4 and 6.5). Figure 6.7 a) shows, in contrast to Figure 6.6 a), that $\phi(0) < \phi_0$ and $\phi(1) = \phi_{\max}$. Therefore, particles aggregate close to the free surface of the film, and according to Figure 6.7 b), flow faster than the more dilute lower layer. This behavior is typical in the ridged regime observed in experiments and the model predictions are again in good

agreement with our experimental results.

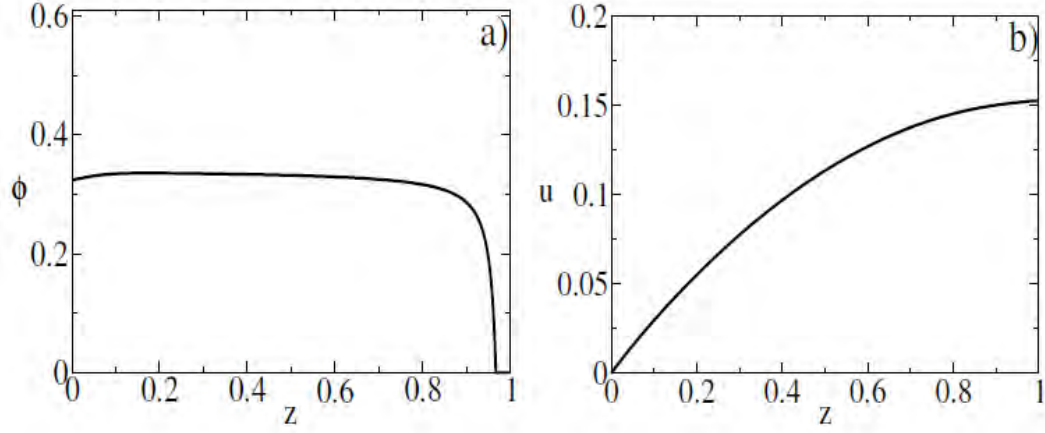


Figure 6.8: Numerical solution for $\phi_0 = 0.310$ and $\alpha = 45^\circ$: (a) particle concentration, $\phi(z)$; and (b) velocity, $u(z)$. Note that $\phi_{\max} > \phi(0) > \phi_0$ and $\phi(1) = 0$ still apply.

Finally, for $(\phi_0, \alpha) = (0.310, 45^\circ)$, the resulting ϕ and u profiles are given in Figure 6.8. With the exception of the experiments with the largest particles (see Figure 6.4 c)), this combination of ϕ_0 and α values leads to a well-mixed regime. From Figure 6.8 a), we see that for most of the film thickness, the particles are uniformly distributed. However, a close inspection reveals that this case still belongs to the category of solutions to Equations (6.7)-(6.8) where $\phi_{\max} > \phi(0) > \phi_0$ and $\phi(1) = 0$, namely the settled regime. In addition, Figure 6.8 b) indicates that the very thin layer of clear liquid at the free surface still flows faster than the particle-laden layer below it. While our model is a steady state one, one could clearly see how, in a dynamic setting, the situation shown in Figure 6.8 eventually leads to a settled regime, with the top layer of clear liquid becoming ever thicker and flowing ever faster as the system evolves.

Next, we examine the agreement between the $\alpha(\phi_0)$ well-mixed curve, given

by Equation (6.9), and the experimental results. We note that, apart from the inclusion of the hindrance due to the presence of a solid track in our model, another important difference between this study and the one in Cook [Coo08] is that we compare the predictions of our model to the results of much more extensive experiments. For this purpose, we go back to Figures 6.3, 6.4, and 6.5. In all diagrams, except the one in Figure 6.4 c), the curve lies completely within the well-mixed band, in excellent agreement with the experimental results. For the largest particles in Figure 6.4 c), the well-mixed regime does not occur; however, the curve overlaps a large section of the border between the settled and ridged bands marking the transition between these two regimes. This again hints at the transiency of the well-mixed regime. The structure of Equations (6.7)-(6.8) also indicates that the well-mixed regime is an unstable root of the system. Even if ϕ_0 and α values are adjusted to lie exactly on the well-mixed curve, even the smallest of perturbations will eventually cause a bifurcation to either the settled or ridged regime. The strongest evidence for this argument is given by Figure 6.4 c), where the relevant settling time scales are short enough so that the bifurcation occurs rapidly and the well-mixed band simply collapses to the well-mixed curve. Other phase diagrams in Figures 6.3, 6.4, and 6.5 are also in line with our argument, only the time scales at which the bifurcation occurs are much longer compared to the one in Figure 6.4 c), leading to an observable well-mixed regime. A sufficiently long experimental track would allow for the bifurcation to occur, resulting in the eventual collapse of all well-mixed bands in Figures 6.3, 6.4, and 6.5.

Finally, it is worthwhile to emphasize that our model is a steady state one while the behavior shown (e.g., in Figure 6.2 a)), where a clear film leaves a particle-rich sediment behind and develops fingers, is clearly a dynamic process which could only be captured by a more complete evolutionary-type model. How-

ever, the settling behavior, which our simple model correctly predicts, is the most crucial ingredient, as it truly sets the stage for these more complex dynamic processes. Therefore, our model should be considered as one of the main components of any fully dynamic model.

6.6 Summary

In this chapter, we focus on experiments with particle-laden thin film flows down an incline, where the effects of the viscosity of the suspending liquid and the particle size are examined. We observe that the settling behavior of particles proceeds in three distinct regimes: settled, well-mixed, and ridged, depending on the bulk particle concentration, ϕ_0 , and the inclination angle, α . Our theoretical model, based on equilibrium theory where hindered settling balances shear-induced migration, is found to be in excellent agreement with our experimental data. More precisely, its predictions for the transition between the settled and ridged regimes match the experimental observations exactly over all ranges of viscosities and particle sizes. Furthermore, both our model and our experimental results suggest that the intermediate well-mixed regime is a transient. In particular, our equilibrium theory predicts no such regime; our experiments show how the well-mixed band collapses as the relevant time scales are changed by varying the viscosity and the particle size. Therefore, we argue that the well-mixed regime eventually leads to a bifurcation to either the settled or ridged regime.

Our experimental results indicate that particle size is a significant parameter. The likelihood of observing the well-mixed regime increases with a decrease in particle diameter. The viscosity of the suspending liquid is found to affect the relevant time scale of the flow. For the smallest considered particle size, the liquid viscosity also significantly affects the likelihood of the well-mixed regime: it

is more prevalent in the case of a less viscous suspending liquid. A combination of a low viscosity liquid and small particles significantly affects the relevant time scales. The flowing film runs out of track length before any substantial disturbance to the uniformity of the suspension is observed. We argue that given a sufficiently long track, the well-mixed bands in phase diagrams such as those in Figures 6.3, 6.4, and 6.5 might eventually collapse to a well-mixed line given by Equation (6.9), so that only the settled and ridged regimes are observed.

The development of a tractable theoretical model for particle-laden thin films, incorporating all the relevant physical mechanisms, is an interesting problem. This model would have to account for the momentum conservation and continuity in the liquid, and include the capillary and contact line effects, along with those relevant to particle migration. Hence, this task is still a formidable one. Instead, a simplified steady state model is derived here. The model considers a balance between the hindered settling and shear-induced migration of particles, and it is shown to provide useful new information about the settling behavior. This chapter therefore makes a significant step toward a fully quantitative model by identifying the dominant equilibrium physics for the flow. In addition, it also implies further modifications required in order to fully understand the transiency of the well-mixed regime and the intricacies connected to the time scales relevant to the front motion and particle settling. Our study also raises interesting questions regarding the motion of the contact lines and the fingering instability. A more complete theoretical model would allow for a comparison with the time dependent experimental results from Ward et al. [WWG09], regarding the front motion in particle-laden films. In addition, the experiments with clear liquid flows in Jerrett and de Bruyn [JB92] showed that once the fingering instability occurred, the exponent in the power law (e.g., [Hup82]) describing the evolution of the front position was modified. Carrying out a similar study in the particle-

laden setting would indeed be compelling, especially since it would also allow for the examination of the connection between different settling regimes and the wavelength of the fingering instability.

CHAPTER 7

Dissertation Summary

In Chapter 1, we presented the motivation for the ADI scheme for the particle-laden thin film flow equations as well as outlined our work on constant-volume problems, equilibrium theory, and experiments.

Chapter 2 described the system of equations for particle-laden thin film flow. One equation is related to the film thickness, h , and the other to the particle concentration, ϕ . The equations are obtained using conservation of volume, for the fluid as a whole and for the particulate phase. The two velocity terms, \mathbf{v}_{av} and \mathbf{v}_{rel} , are the average velocity of the liquid and particles and the velocity of the particle relative to the liquid, respectively. A shear-induced diffusion term is added in to correct for an instability in the particle concentration.

Chapter 3 gave the derivation for the semi-implicit ADI scheme for the particle-laden thin film flow equations. ADI is used for applicable terms and the remaining ones are treated explicitly. Forward Euler is employed for the explicit terms and backward Euler for the implicit terms. The spatial discretizations are done via centered differencing. A moving reference frame is utilized to reduce the size of the domain needed for simulations, and the speed for the frame can be determined based on shock theory for the first-order system of equations.

Various choices for the implementation of the scheme and results from the simulations were discussed in Chapter 4. Based on simulations, the best choice,

in terms of runtime, is performing iterations at each timestep and extrapolating the approximate terms. The scheme parallelizes well, with nearly eight times speed-up for eight processors. The scheme serves as a means to compare the model to experiments. A mixture of silicone oil and glass beads is used in an experiment, and the results from this are compared with a numerical simulation with the same parameters. The comparison shows good qualitative agreement, but lacks some quantitative agreement. We also discuss the advantages of using this scheme and future work.

In Chapter 5, we compared results for constant-volume particle-laden flows in terms of theory, numerics, and experiments. A similarity solution without the settling of particles is derived with and without a precursor. In comparison with the one-third power law, we observe qualitative agreement from experiments. Testing a different hindered settling function, we find that for $\phi_{\max} = 0.67$, the exponent $m = 1$, instead of $m = 5$, produces a more pronounced particle-rich ridge, which is consistent with the behavior seen in experiments. Comparing the effects of the precursor and settling, the front speed of the fluid is more influenced by the precursor thickness than the addition of particle settling. For the scaling constant, C , the best agreement between theory, numerics, and experiments occurs at $\phi_0 = 0.45$, which is theorized to be the point which separates the regimes where the particles settle to the substrate and where the particles migrate to the front of the flow, forming a particle-rich ridge.

We examined the effects of various liquid viscosities and particle sizes on the behavior of the liquid/particle mixture in Chapter 6. The size of the particles has an effect on the settling behavior, with larger particle settling to the substrate faster. This produces the appearance of large well-mixed regions for smaller particles. Due to the speed of the settling, the time scale for particle motion

is affected as well. The viscosity of the liquid component influences particle motion, especially for smaller particles. The transient nature of the well-mixed regime is observable as the particle size increases. The equilibrium theory, based on the model and numerics, predicts that the well-mixed regime is an unstable equilibrium separating the settled and ridged regimes.

REFERENCES

- [Bat72] G.K. Batchelor. “Sedimentation in a dilute suspension of spheres.” *J.Fluid Mech.*, **52**:245–268, 1972.
- [BB97] A.L. Bertozzi and M.P. Brenner. “Linear stability and transient growth in driven contact lines.” *Phys. Fluids*, **9**:530–539, 1997.
- [BBD94] A.L. Bertozzi, M.P. Brenner, T.F. Dupont, and L.P. Kadanoff. *Singularities and similarities in interface flows, Trends and Perspectives in Applied Mathematics*, pp. 155–208. Springer-Verlag Applied Mathematical Sciences, New York, 1994.
- [BBG98] J.W. Barrett, J.F. Blowey, and J. Garcke. “Finite element approximation of a fourth order nonlinear degenerate problem.” *Numer. Math.*, **80**:525–556, 1998.
- [BGO82] R. Buscall, J.W. Goodwin, R.H. Ottewill, and T.F. Tadros. “The settling of particles through Newtonian and non-Newtonian media.” *J. Colloid Interface Sci.*, **85**:78–86, 1982.
- [BM73] E. Barnea and J. Mizrahi. “A generalized approach to the fluid dynamics of particulate systems 1. General correlation for fluidization and sedimentation in solid multiparticle systems.” *Chem. Eng. J.*, **5**:171–189, 1973.
- [BW80] R.M. Beam and R.F. Warming. “Alternating direction implicit methods for parabolic equations with a mixed derivative.” *SIAM J. Sci. Stat. Comp.*, **1**:131–159, 1980.
- [CAB09] B. Cook, O. Alexandrov, and A. Bertozzi. “Linear stability of particle-laden thin films.” *Eur. Phys. J. Spec. Top.*, **166**:77–81, 2009.
- [CBH08] B.P. Cook, A.L. Bertozzi, and A.E. Hosoi. “Shock solutions for particle-laden thin films.” *SIAM J. Appl. Math.*, **68**:760–783, 2008.
- [Coo07] B.P. Cook. *Lubrication models for particle-laden thin films*. PhD thesis, University of California, Los Angeles, 2007.
- [Coo08] B. Cook. “A theory for particle settling and shear-induced migration in thin film flow.” *Phys. Rev. E Stat. Nonlin. Soft Matter Phys.*, **78**:045303 1–4, 2008.

- [CS88] I.J.D. Craig and A.D. Sneyd. “An alternating-direction implicit scheme for parabolic equations with mixed derivatives.” *Comput. Math. Applic.*, **16**:341–350, 1988.
- [DA85] R.H. Davis and A. Acrivos. “Sedimentation of noncolloidal particles at low Reynolds-numbers.” *Ann. Rev. Fluid Mech.*, **17**:91–118, 1985.
- [DK02] J.A. Diez and L. Kondic. “Computing Three-Dimensional Thin Film Flows Including Contact Lines.” *Jour. Comp. Phys.*, **183**:274–306, 2002.
- [Eva98] L.C. Evans. *Partial differential equations*. American Mathematical Society, Providence, 1998.
- [GLM10] N. Grunewald, R. Levy, M. Mata, T. Ward, and A.L. Bertozzi. “Self-similarity in particle-laden flows at constant volume.” *J. Eng. Math.*, **66**:53–63, 2010.
- [GR00] G. Grun and M. Rumpf. “Nonnegativity preserving convergent schemes for the thin film equation.” *Numer. Math.*, **87**:113–152, 2000.
- [GR01] G. Grun and M. Rumpf. “Simulations of singularities and instabilities arising in thin film flow.” *Euro. J. Appl. Math.*, **12**:293–320, 2001.
- [HB65] H. Happel and H. Brenner. *Low Reynolds number hydrodynamics with special applications to particulate media*. Prentice-Hall, Englewood Cliffs, NJ, 1965.
- [Hup82] H. Huppert. “Flow and instability of a viscous current down a slope.” *Nature*, **300**:427–429, 1982.
- [JB92] J.M. Jerrett and J.R. de Bruyn. “Finger instability of a gravitationally driven contact line.” *Phys. Fluids A*, **4**:234–242, 1992.
- [Kar09] S. Karaa. “A high-order ADI method for parabolic problems with variable coefficients.” *Int. J. Comput. Math.*, **86**:109–120, 2009.
- [KB99] L. Kondic and A.L. Bertozzi. “Nonlinear dynamics and transient growth of driven contact lines.” *Phys. Fluids*, **11**:3560–3562, 1999.
- [KLK08] J.M. Kim, S.G. Lee, and C. Kim. “Numerical simulations of particle migration in suspension flows: Frame-invariant formulation of curvature-induced migration.” *J. Non-Newtonian Fluid Mech.*, **150**:162–176, 2008.

- [Kon03a] L. Kondic. “Instabilities in gravity driven flow of thin fluid films.” *SIAM Rev. Soc. Ind. Appl. Math.*, **45**:95–115, 2003.
- [Kon03b] L. Kondic. “Instability in the gravity driven flow of thin liquid films.” *SIAM Review*, **45**:95–115, 2003.
- [Kri72] I.M. Krieger. “Rheology of monodisperse lattices.” *Adv. Colloid Interface Sci.*, **3**:111–136, 1972.
- [LA86] D. Leighton and A. Acrivos. “Viscous resuspension.” *Chem Eng Sci*, **41**, 1986.
- [LA87a] D. Leighton and A. Acrivos. “Measurement of shear-induced self-diffusion in concentrated suspensions of spheres.” *J.Fluid Mech.*, **177**:109–131, 1987.
- [LA87b] D. Leighton and A. Acrivos. “The shear-induced migration of particles in concentrated suspensions.” *J. Fluid Mech.*, **181**:415–439, 1987.
- [Lax73] P.D. Lax. “Hyperbolic systems of conservation laws and mathematical theory of shock waves.” *CBMS-NSF Regional Conference Series in Applied Mathematics*, **11**:1–48, 1973.
- [LCS06] X-Z. Liu, X. Cui, and J-G. Sun. “FDM for multi-dimensional nonlinear coupled system of parabolic and hyperbolic equations.” *J. Comput. Appl. Math.*, **186**:432–449, 2006.
- [Lei85] D. Leighton. *The shear induced migration of particulates in concentrated suspensions*. PhD thesis, Stanford Univ., 1985.
- [LGP02] A.V. Lyushnin, A.A. Golovin, and L.M. Pismen. “Fingering instability of thin evaporating liquid films.” *Phys. Rev. E Stat. Nonlin. Soft Matter Phys.*, **65**:021602 1–7, 2002.
- [MB99] J.F. Morris and F. Boulay. “Curvilinear flows of noncolloidal suspensions: The role of normal stresses.” *J. Rheol.*, **43**:1213–1237, 1999.
- [McK71] S. McKee. “Alternating direction methods for a system of parabolic equations in two space dimensions with a mixed derivative.” *J. Inst. Math. Appl.*, **8**:376–385, 1971.
- [NB94] P.R. Nott and J.F. Brady. “Pressure-driven flow of suspensions - simulation and theory.” *J.Fluid Mech.*, **275**:157–199, 1994.

- [NHS89] Y. Nohguchi, K. Hutter, and S.B. Savage. “Similarity solutions for granular avalanches of finite mass with variable bed friction.” *Continuum Mech. Thermodyn.*, **1**:239–265, 1989.
- [NS09] M. Naumov and A.H. Sameh. “A tearing-based hybrid parallel banded linear system solver.” *J. Comput. Appl. Math.*, **226**:306–318, 2009.
- [PAB92] R.J. Phillips, R.C. Armstrong, R.A. Brown, A.L. Graham, and J.R. Abbott. “A constitutive equation for concentrated suspensions that accounts for shear-induced particle migration.” *Phys. Fluids A*, **4**:30–40, 1992.
- [Pao99] C.V. Pao. “Numerical analysis of coupled systems of nonlinear parabolic equations.” *SIAM J. Numer. Anal.*, **36**:393–416, 1999.
- [PDS97] O. Pouliquen, J. Delour, and S.B. Savage. “Fingering in granular flow.” *Nature*, **386**:816–817, 1997.
- [PR55] D.W. Peaceman and H.H. Rachford, Jr. “The numerical solution of parabolic and elliptic differential equations.” *J. Soc. Ind. Appl. Math.*, **3**:28–41, 1955.
- [PS06] E. Polizzi and A.H. Sameh. “A parallel hybrid banded system solver: The SPIKE algorithm.” *Parallel Comput.*, **32**:177–194, 2006.
- [RZ54a] J.F. Richardson and W.N. Zaki. “Sedimentation and fluidization: Part I.” *Trans. Inst. Chem. Eng.*, **32**:35–53, 1954.
- [RZ54b] J.F. Richardson and W.N. Zaki. “The sedimentation of a suspension of uniform spheres under conditions of viscous flow.” *Chem. Eng. Sci.*, **3**:65–73, 1954.
- [SAZ90] U. Schafflinger, A. Acrivos, and K. Zhang. “Viscous resuspension of a sediment within a laminar and stratified flow.” *Int. J. Multiphase Flow*, **16**:567–578, 1990.
- [SD85] N. Silvi and E.B. Dussan V. “On the rewetting of an inclined solid surface by a liquid.” *Phys. Fluids*, **28**:5–7, 1985.
- [SH89] S.B. Savage and K. Hutter. “The motion of a finite mass of granular material down a rough incline.” *J. Fluid Mech.*, **199**:177–215, 1989.
- [SIJ76] Satteluri, R.K. Iyengar, and M.K. Jain. “Comparative study of two and three level ADI methods for parabolic equations with a mixed derivative.” *Int. J. Numer. Methods Eng.*, **10**:1309–1315, 1976.

- [SM00] P. Snabre and P. Mills. “Settling and fluidization of non-Brownian hard spheres in a viscous liquid.” *Euro. Phys. J. E*, **1**:105–114, 2000.
- [SP05] J.J. Stickel and R.L. Powell. “Fluid mechanics and rheology of dense suspensions.” *Annu. Rev. Fluid Mech.*, **37**:129–149, 2005.
- [SRX07] P. Sun, R.D. Russell, and J. Xu. “A new adaptive local mesh refinement algorithm and its applications on fourth order thin film flow problem.” *J. Comput. Phys.*, **224**:1021–1048, 2007.
- [THS89] S.M. Troian, E. Herbolzheimer, S.A. Safran, and J.F. Joanny. “Fingering instabilities of driven spreading films.” *Europhys. Lett.*, **10**:25–30, 1989.
- [TM05] B.D. Timberlake and J.F. Morris. “Particle migration and free-surface topography in inclined plane flow of a suspension.” *J. Fluid Mech.*, **538**:309–341, 2005.
- [WB03] T. Witelski and M. Bowen. “ADI schemes for higher-order nonlinear diffusion equations.” *Appl. Numer. Math.*, **45**:331–351, 2003.
- [WCM05] M.R.E. Warner, R.V. Craster, and O.K. Matar. “Fingering phenomena associated with insoluble surfactant spreading on thin liquid films.” *J. Fluid Mech.*, **510**:169–200, 2005.
- [WWG09] T. Ward, C. Wey, R. Glidden, A. Hosoi, and A. Bertozzi. “Experimental study of gravitation effects in the flow of a particle-laden thin film on an inclined plane.” *Phys. Fluids*, **21**:083305 1–7, 2009.
- [ZB00] L. Zhornitskaya and A.L. Bertozzi. “Positivity-preserving numerical schemes for lubrication-type equations.” *SIAM J. Numer. Anal.*, **37**:523–555, 2000.
- [ZDB05] J. Zhou, B. Dupuy, A.L. Bertozzi, and A.E. Hosoi. “Theory for shock dynamics in particle-laden thin films.” *Phys. Rev. Lett.*, **94**:117803 1–4, 2005.
- [ZHL00] I.E. Zarraga, D.A. Hill, and D.T. Leighton, Jr. “The characterization of the total stress of concentrated suspensions of noncolloidal spheres in Newtonian fluids.” *J. Rheol.*, **44**:185–220, 2000.